Technische Universität Braunschweig

Aidin Lak

Synthesis and Characterization of Magnetic Iron Oxide Nanoparticles

Dissertation
Braunschweig 2013

Berichte aus dem **Institut für Elektrische Messtechnik und Grundlagen der Elektrotechnik**

Band **44**

Hrsg. Prof. Dr. Meinhard Schilling

Synthesis and Characterization of Magnetic Iron Oxide Nanoparticles

Von der Fakultät für Elektrotechnik, Informationstechnik, Physik
der Technischen Universität Carolo-Wilhelmina
zu Braunschweig
zur Erlangung des Grades eines
Doktors der Naturwissenschaften
(Dr.rer.nat.)

genehmigte
Dissertation

von:	Aidin Lak, M.Sc.
aus:	Hamedan (Iran)

1. Referent:	Prof. Dr. Meinhard Schilling
2. Referent:	Prof. Dr. Fred Jochen Litterst
eingereicht am:	05.07.2013
mündliche Prüfung am:	10.10.2013
Druckjahr:	2013

To Matin

Abstract

In this thesis, hydrophobic single-core superparamagnetic iron oxide nanoparticles were synthesized via high temperature decomposition of iron-oleate. The impact of common synthesis parameters on particle size distribution and magnetic properties were explored by exploiting design of experiment methodology. A simple empirical growth model presenting the dependencies of particle hydrodynamic size on reaction temperature and time and iron-oleate concentration was found. The formation of highly monodisperse particles was attributed to burst nucleation and rapidly terminating growth mechanisms. The slow decomposition of iron-oleate results in the crystallization of larger particles via gradual nucleation and retarded growth mechanisms. We succeeded in establishing a robust and reproducible synthesis procedure to judiciously tailor the particle core size from 12 to 25 nm while preserving the size deviation $< 10\%$.

An anomalous magnetic behavior was observed in larger particles. By performing deeper investigations on particles, a model describing the change in the particle phase composition from pure Fe_3O_4 to a mixture of Fe_3O_4, FeO and an interfacial FeO/Fe_3O_4 phase as particle size enlarges was established. The biphasic particles show a deteriorated magnetic performance. This phenomenon was related to the existence of differently oriented Fe_3O_4 crystalline domains in particle outer layers and paramagnetic FeO phase.

The nanoparticles were transferred into water via exchanging oleic acid with poly(ethylene glycol). They retained monodisperse and their magnetic core remained intact after PEGylation as proven by various techniques. The particles show an excellent stability in water. Besides, the particles exhibited a moderate cytotoxic effect on macrophages and no release of inflammatory or anti-inflammatory cytokines.

The PEGylated particles with a mean core and hydrodynamic size of 24 and 60 nm were functionalized with Herceptin antibodies for performing homogeneous magnetic bioassays. The particle surface modification and functionalization were monitored by measuring particle phase lag change using a fluxgate-based rotating magnetic field setup. The results showed that these particles, primarily relaxing via the Brownian mechanism, are a potent tracer for magnetic bioassays.

Nomenclature

ACS	AC susceptibility
AFM	Antiferromagnetic
bcc	Body-centred cubic
BF	Bright field
DF	Dark field
DOE	Design of experiment
DSC	Differential scanning calorimetry
DWs	Domain walls
EA	Elemental analysis
EB	Exchange bias energy
EELS	Electron energy loss spectroscopy
ELISA	Enzyme-linked immunosorbent assay
ESI	Electron spectroscopic imaging
FC	Field cooled
fcc	Face-centred cubic
Fe-OLA	Fe-oleate
FFT	Fast fourier transform
FIM	Ferrimagnetic
FWHM	Full width half maximum
HRTEM	High resolution transmission electron microscopy
IR	Fourier transform infrared spectroscopy
LDH	Lactate dehydrogenase
MNPs	Magnetic nanoparticles
MPI	Magnetic particle imaging
MRI	Magnetic resonance imaging
MRX	Fluxgate magnetorelaxometry

MS	Mössbauer spectroscopy
MSM	Moment superposition model
NMR	Nuclear magnetic resonance spectroscopy
NP-Herceptin	Herceptin functionalized nanoparticles
NP-OA	Oleic acid capped nanoparticles
NP-PEG	PEGylated nanoparticles
NPs	Nanoparticles
OA	Oleic acid
PBS	Phosphate buffered saline
PCCS	Photon cross-correlation spectroscopy
PEG	Poly(ethylene glycol)
RMF	Rotating magnetic field
RT	Room temperature
SAED	Selected area electron diffraction
SNR	Signal-to-noise ratio
SPIONs	Superparamagnetic iron oxide nanoparticles
SQUIDs	Superconducting quantum interference devices
SVD	Singular value decomposition
TEM	Transmission electron microscopy
TGA	Thermogravimetric analysis
WR-PEELS	Wide range parallel electron energy loss spectroscopy
XRD	X-ray diffraction
ZFC	Zero field cooled

Contents

Introduction

The huge scientific and technological interests in fabrication of magnetic nanoparticles with defined size and shape distributions and high magnetic performance for applications such as homogeneous magnetic bioassays, magnetic particle imaging, targeted drug delivery, etc. are the major motivations of this study [1, 2]. Synthesis of functional magnetic biomarkers begins with the dimensionally and magnetically controlled synthesis of particles. Fabrication of uniformly sized and shaped nanoparticles has attracted a lot of attention in the last few years and yet is a great challenge. The ability to tailor size and morphology of nanoparticles gives the opportunity of exploring magnetism at the nanoscale, allowing to gain a deeper understanding of magnetic phenomenon originating from finite-size effects, such as superparamagnetism. Undoubtedly, superparamagnetism is one of the most intriguing properties of magnetic nanoparticles, appearing below a critical size threshold. The next topic is the characterization of nanoparticles. A broad range of physical properties being structural, compositional and magnetic have to be examined. Correlating different properties and aspects of nanoparticles is one of the biggest challenges. Considering magnetic nanoparticles as nano-biomaterials, it is vital to investigate their physicochemical aspects, including surface chemistry and inertness, toxicological effects and stability and interaction in biological media. Owing to the interdisciplinary nature of this research topic, a close collaboration between materials scientists, physicists, chemists and biologists is the key to overcome difficulties and deepen our knowledge.

The aim of this thesis is to (a) establish a robust and reproducible synthesis protocol for the fabrication of large single-core iron oxide nanoparticles with a narrow size distribution, (b) contribute to a deeper understanding of homogeneous nucleation and growth mechanisms in order to engineer customized particles particularly suitable for homogeneous magnetic detection of biomolecules, (c) correlate crystallographic, compositional and magnetic properties to particle core size, (d) design a phase transfer strategy to efficiently pull hydrophobic nanoparticles into aqueous media and prepare stable aqueous colloidal nanoparticle suspensions, (e) characterize their physical and chemical properties, assess their toxic impact on cells and understand particle cell interaction mechanisms and (f) eventually measure and analyze the particle performance as biomarkers for magnetic detection schemes based on the particle manipulation in dynamic magnetic fields.

The thesis is organized as follows:

In chapter 1, the principles of magnetism and nanomagnetism are reviewed briefly. Superparamagnetism as the most promising dimension dependent effect in single domain magnetic nanoparticles is discussed. The features appearing at the nanoscale, where surface to volume ratio rises significantly and consequently surface dominated effects become strong, are addressed. **In chapter 2**, the crystal structure of iron oxide phases is described. The most commonly used

synthesis methods of iron oxide nanoparticles including chemical precipitation, hydrothermal, microemulsion and thermal decomposition are discussed. The synthesis methods are compared with regard to the resulting particle size distribution and their advantages and drawbacks are addressed. Finally, the theory of homogeneous nucleation and growth mechanisms in colloidal syntheses are reviewed and the synthetic strategies which have been so far proposed for realization of theoretical concepts in a real particle synthesis experiment are thoroughly discussed. **In chapter 3**, the principles of characterization methods which have been used in this thesis to analyze particle size and morphology distributions, crystallography, phase composition, electronic structure, surface chemistry, capping density of capped molecules, long term stability, static and dynamic magnetic properties and magnetic response to dynamic magnetic fields are explained. The assays employed to examine the *in vitro* cytotoxic and intrusive effects of particles are described. **Chapter 4** contains all the experimental parts. The design of experiment methodology applied to optimize the most effective synthesis parameters is described. The synthesis procedure of poly(ethylene glycol) derivative compounds, particle phase transfer into aqueous fluids and further functionalization with Herceptin antibodies are discussed. The preparation method and experimental conditions of toxicity assays are provided. **In chapter 5**, the results of structural, magnetic, hydrodynamic analyses on the particles synthesized via the design of experiment are present and discussed. The particle nucleation and growth mechanisms are thoroughly discussed and a empirical growth model is given. In collaboration with Institute of Physical Chemistry, University of Hamburg, Institute of Condensed Matter Physics, TU Braunschweig and Physikalisch-Technische Bundesanstalt, Braunschweig and Berlin, the particle size dependence structural, compositional and magnetic properties of the synthesized iron oxide nanoparticles were unravelled. Besides the effect of ageing at ambient conditions on particle composition and magnetization is addressed. The physicochemical properties of particles stabilized in water with poly(ethylene glycol) derivative ligands are presented. The results of particle toxicity and cellular uptake assessments, carried out in a collaboration with Helmholtz Center for Infection Research, Braunschweig, are presented in this chapter. The measurement results of particle response to dynamic magnetic fields after PEGylation, functionalization with Herceptin antibodies and labeling with tumor specific HER2 antibodies are presented and discussed.

1 Fundamental

Magnetism has been a research topic for more than three thousand years since the time that iron ore attracted Greek scholars and philosophers' attention. In the last two centuries, the understanding of magnetism has gained a rapid progress which resulted in realizing the link between magnetism and electricity, called electromagnetic wave and known as the nature of light. In the mean time it was understood that magnetism in macroscopic systems is different from atoms and particles although both are made up of the same constituents. This observation opened a new window to the topic and led us to realize that magnetism like superconductivity is a collective phenomenon, influenced by the mutual interaction of an enormous number of particles and atoms [3]. From the technological point of view, a lot of progress in fabricating new permanent magnets, sensors and magnets for recording purposes has been obtained in parallel with the scientific achievements. In the last two decades and by emerging nanotechnology and nanoscience, the chance of studying magnetism as a classical physical phenomenon at the nanoscale (dimensions < 100 nm) has appeared and thus it has become the focus of many studies. Among different nanostructured magnetic materials, magnetic nanoparticles (MNPs) gain an immense interest for being used in a variety of biomedical and bioanalytical applications owing to their promising properties. In this chapter, we are going to briefly review the principle of magnetism in order to make a bridge to the phenomena prevailing magnetism in nanostructured materials.

1.1 Magnetism

The gateway to the magnetism is to understand how magnetic materials respond to an external magnetic field. Therefore, here it is vital to review some basic concepts of magnetism.

When a magnetic material is exposed to a magnetic field of strength H in A m^{-1}, the magnetic moments response to the field and the overall induced magnetization, denoted as flux density $\overrightarrow{B}$ in Tesla, is given by

$$\overrightarrow{B} = \mu_0 \left(\overrightarrow{H} + \overrightarrow{M} \right), \tag{1.1}$$

with $\mu_0 = 4\pi \times 10^{-7}$ the permeability of vacuum in J $A^{-2}m^{-1}$, and M magnetization in A m^{-1} given by

$$\overrightarrow{M} = \frac{\overrightarrow{m}}{V}, \tag{1.2}$$

where m is the net magnetic moment of a volume V of the magnetic material.

Broadly speaking, all materials are to some extent magnetic and in a simple classification their magnetization $\overrightarrow{M}$ is linearly proportional to the magnetic field $\overrightarrow{H}$ via volumetric magnetic susceptibility χ and may be written as

$$\overrightarrow{M} = \chi \overrightarrow{H}, \tag{1.3}$$

with χ a dimensionless parameter. In most crystals, the magnetic susceptibility is a tensor.

Substituting Eq. 1.3 into Eq. 1.1, Eq. 1.1 for small fields can be rewritten as

$$\overrightarrow{B} = \mu_0 \left(1 + \chi\right) \overrightarrow{H} = \mu_0 \mu_r \overrightarrow{H}, \tag{1.4}$$

in which $\mu_r = (1 + \chi)$ is the relative permeability of a magnetic material [3, 4].

Generally, all materials to some extent reveal magnetic responses. Those types, which show negative or very small positive magnetic response to an applied field $\overrightarrow{H}$, are called diamagnets and paramagnets, respectively. The magnetically ordered materials are classified as ferromagnetic, ferrimagnetic and antiferromagnetic depending on how the spins are coupled.

Diamagnetism

A material is called a diamagnet if it has no magnetic dipoles in the absence of an external magnetic field and shows a very weak induced dipole in the opposite direction of the applied magnetic field as visualized in Fig. 1.1. Therefore, diamagnetic materials show small magnetic responses with the negative magnetic susceptibility χ in the range of -10^{-6} to -10^{-3} [5].

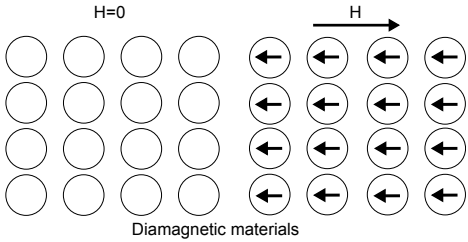

Figure 1.1: Schematic presentation of diamagnetic materials behavior in absence and presence of an external magnetic field.

Paramagnetism

In contrast to the diamagnetism, paramagnetism is described by the alignment of the magnetic dipoles parallel to the applied magnetic field. Paramagnetic materials reveal randomly distributed dipoles in the absence of the magnetic field. Both mechanisms are illustrated in Fig. 1.2(a). Generally speaking, the magnetic response of the paramagnetic materials is relatively weak and the magnetic susceptibility χ is positive and varying from 10^{-6} to 10^{-1} [5]. Positive magnetic response of paramagnets compared to the negative one of diamagnets is seen in their magnetization versus an applied field $M - H$ curves as shown in Fig. 1.2(b).

Ferromagnetism

Ferromagnetic materials are characterized by their spontaneous magnetization regardless of the absence or presence of an external magnetic field. The magnetic moments are aligned parallel in one specific direction depending on the crystal structure as depicted in Fig. 1.3. The ferromagnetism originates from exchange interactions occurring in ordered magnetic solids. At the macroscopic scale, these materials exhibit permanent magnetization.

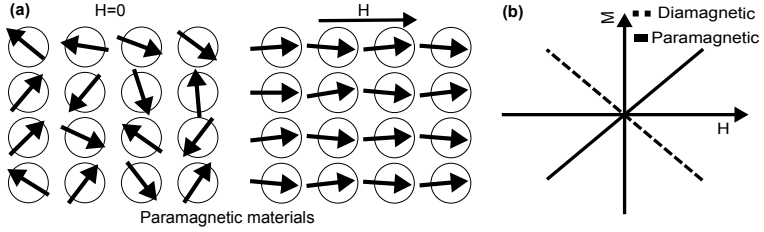

Figure 1.2: Schematic depiction of the behavior of paramagnetic materials in absence and presence of a magnetic field.

Ferrimagnetism

The difference between ferrimagnetic (FIM) and ferromagnetic materials is related to the alignment of adjacent dipoles. In FIM materials, in the absence of a magnetic field, weaker magnetic dipoles aligned antiparallel to their adjacent stronger dipoles reduce the net magnetization as depicted in Fig. 1.3.

Antiferromagnetism

Antiferromagnetic (AFM) materials consist of two magnetic sublattices in each the atomic magnetic moments are coupled ferromagnetically, but the magnetic moments belonging to two different sublattices are oriented antiparallel. Thus, essentially the net magnetization of an antiferromagnet is zero. The described mechanism can be seen in Fig. 1.3.

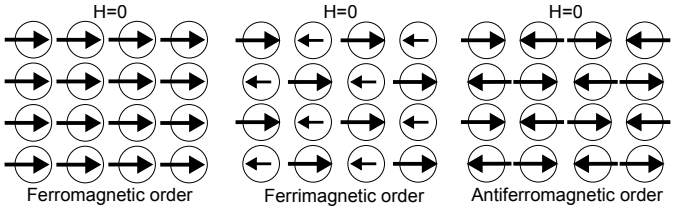

Figure 1.3: Behavior of ferromagnetic, ferrimagnetic and antiferrimagnetic materials in absence of a magnetic field.

1.1.1 Hysteresis loops

Magnetic properties of magnetic materials can primarily be characterized by analysis of their magnetic response to an applied external magnetic field ($M-H$ curves) known as hysteresis loops. Fig.1.4 shows a typical $M-H$ hysteresis loop of a ferromagnet. By applying a sufficiently large DC magnetic field, the magnetic spins become aligned in the field direction and the magnetization reaches a plateau, the so-called saturation magnetization M_s. By decreasing the H value to zero, spins start to relax and do not any longer follow the field and thereby the net magnetization drops to a residual magnetization denoted as remanent magnetization M_r. Ultimately, to reach zero magnetization, a magnetic field in the opposite direction has to be applied. The magnitude of the requiring field is called coercivity H_C which depends on both structural features such as size, shape, vacancies, impurities, or grain boundaries and intrinsic properties including crystalline anisotropy, etc. of the investigated material. The coercivity is given by

$$H_C = \frac{(H^+ - H^-)}{2}, \tag{1.5}$$

with H^+ and H^- the positive and negative coercivities.

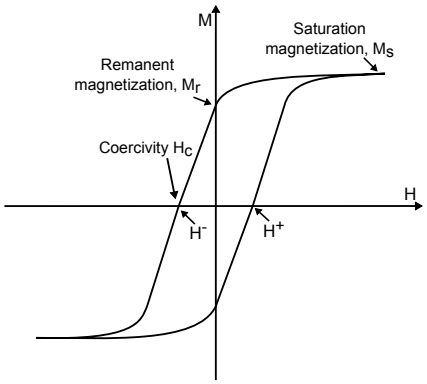

Figure 1.4: A typical $M - H$ hysteresis loop of a ferromagnet.

1.2 Nanomagnetism

Nanomagnetism relates to magnetic phenomena occurring in the dimensions below 100 nm (nanoscale). Broadly speaking, the magnetization in nanomaterials is governed by the competition between two key features: finite-size and surface effects, arising from small size, confined geometry and high surface to volume ratio of nanoparticles (NPs). These phenomena result in the appearance of several intriguing properties in the NPs which have not been observed in bulk materials. The finite-size effects are related to those features of magnetic materials which are influenced by reduction in size and dimension. Of the most investigated ones, single-domain and superparamagnetic size thresholds can be mentioned [2, 6]. The magnetization reveals promising and yet unknown features when the particle size is comparable to the characteristic length of some fundamental magnetic phenomena such as the crystalline anisotropy length l_K, the magnetostatic length l_S and the applied field length l_H which may be written as

$$l_K = \sqrt{\frac{J}{K}} \tag{1.6}$$

$$l_S = \sqrt{\frac{2J}{\mu_0 H M_s}} \tag{1.7}$$

$$l_H = \sqrt{\frac{J}{2\pi\mu_0 M_s^2}} \tag{1.8}$$

where J (J m^{-1}) is the exchange within a grain, K (J m^{-3}) is the anisotropy constant and H is the applied field. If more than one type of barrier exists, the shortest characteristic length determines the material properties [5].

Since the particle surface to volume ratio becomes significantly large at the nanoscale, the surface dominated properties are of particular interest. One of the most relevant surface features is surface spin disordering, caused by random orientation of the spins on the surface compared to the bulk like ordering exiting in the magnetic core. The disordered surface spins form a so called magnetic dead layer which has nearly no contribution to the net magnetization and even degrades the magnetic properties.

1.2.1 Anisotropy

When MNPs experience an external magnetic field in equilibrium, the total magnetization points in a direction in which the minimum anisotropy energy is achieved [6]. The magnetic anisotropy energy, being assumed uniaxial for spherical particles, is given by

$$E(\Theta) = KV \sin^2 \Theta, \tag{1.9}$$

with V_c the magnetic core volume, K the effective anisotropy coefficient and Θ the angle between the magnetization easy axis and magnetic moment (see Fig. 1.5). The term KV in Eq. 1.9 is known as the anisotropy energy barrier E_B^0. When a magnetic field H with an angle $\theta - \varphi = \psi$ with respect to the particle magnetization axis is applied to a particle, Eq. 1.9 shall be modified and be rewritten as

$$E(\Theta) = KV_c \sin^2 \Theta - \mu_0 V_c H M_s \cos(\theta - \varphi). \tag{1.10}$$

In fact, this is based on the Stoner-Wohlfarth model. The axis system and angles are defined in Fig. 1.5. In zero magnetic field, the preferential orientation of the magnetization coincides with the anisotropy axis (i.e. magnetization easy axis), whereas under applying an external magnetic field, the magnetization axis rotates towards the field direction. If H is smaller than a threshold denoted by switching field at zero temperature H_{sw}^0, $E(\theta)$ shows two minima which are separated by an energy barrier E_B. The two minima appear at $\theta = 0$ and $\theta = \pi$ when no external field is applied. If the applied field points in the opposite direction of the magnetization, the energy barrier can be expressed by

$$E_B(H) = E_B^0 (1 - \frac{H}{H_{sw}^0})^{\kappa}, \tag{1.11}$$

with κ a phenomenological exponent depending on φ. The switching field H_{sw}^0 is the least amount of the field at zero temperature which enables the magnetization to flip from one easy axis to another one [6, 7].

Bulk anisotropy

The magnetization of magnetic materials is influenced by two general types of anisotropy: bulk and surface. The most common types of the bulk anisotropy in nanomaterials are magnetocrystalline and shape anisotropy. The magnetocrystalline anisotropy is an intrinsic property of a material independent of its shape.

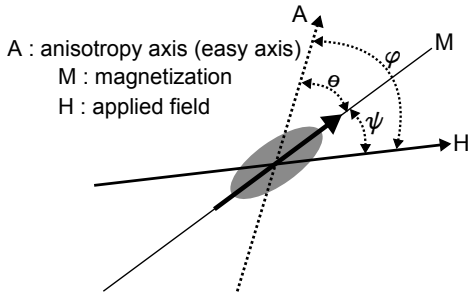

Figure 1.5: Illustration of anisotropy, magnetization and applied field axes and their angles with respect to each other.

Owing to the magnetocrystalline anisotropy, the magnetization in MNPs tends to occur along a certain crystallographic direction known as the magnetization easy axis. In polycrystalline particles, consisting of several primary crystallites oriented in different directions, a negligible net magnetocrystalline anisotropy is expected due to averaging over all directions. The shape anisotropy plays no significant role when MNPs are spherical and it becomes important when a 1D material is magnetized [5, 7].

Surface anisotropy

It has been experimentally realized that the effective anisotropy energy increases as the particle size decreases. This observation was attributed to a bigger contribution of the surface anisotropy at the nanoscale since the surface to volume ratio is much higher. The relation between the effective K, bulk K_b and surface K_s anisotropies per unit volume for spherical particles can be described using a phenomenological model given by [5]

$$K = K_b + \frac{6}{d_c} K_s, \tag{1.12}$$

The surface anisotropy plays a crucial role in the magnetization of MNPs. For instance, in 2 nm fcc Co NPs, the surface anisotropy is one order of magnitude larger than the bulk one [6].

Exchange anisotropy

Exchange anisotropy is a rare type of anisotropy usually seen at the interface of a ferrimagnet (FIM) and antiferromagnet (AFM). The exchange coupling happens when a FIM with the Curie temperature T_C higher than the Néel temperature of an AFM are in proximity. If this system is cooled to temperatures below the Néel temperature of AFM in a DC magnetic field, the recorded $M - H$ loop seems to be shifted. The energy associated with this exchange coupling can be characterized with the exchange field H_E and can be expressed by

$$H_E = \frac{-(H^+ + H^-)}{2}. \tag{1.13}$$

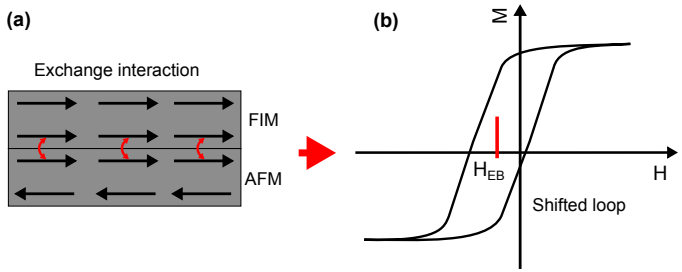

Figure 1.6: (a) Spin coupling at FIM/AFM interface causing an exchange interaction and (b) its consecutive impacts on the magnetization seen as a shifted field cooled $M - H$ hysteresis loop.

1.2.2 Single and multi-domain particles

Magnetic NPs are classified into two general groups: single and multi-domain particles. Magnetic domains are the areas in which spins are aligned in a certain direction (uniform magnetization regions) and separated by domain walls (DWs). The DWs form due to the energy competition between magnetostatic energy E_{ms}, proportional to the particle volume, and the domain wall energy E_{dw} depending on the inter-domain areas. This means that a new DW nucleates when the cost of the magnetostatic energy is bigger than the one for the domain wall. In other words, this implies that the bigger the particle volume is, the stronger the trend to form further DWs would be. On the contrary, when the particle size drops below a certain limit (a so-called single-domain size threshold r_s), the energy of the nucleation of a new DW overtakes the magnetostatic energy of a single domain-particle and thus being single-domain is energetically favorable. The single-domain size limit r_s is usually in the order of a few tens of nanometers and depends on saturation magnetization M_s, anisotropy energy $E(\theta)$, exchange interaction between spins and materials type [6, 8]. From the energy point of view, transition from multi to single-domain regime occurs when E_{ms}=E_{dw} and its corresponding size limit r_s is given by

$$r_s \approx 18 \frac{\sqrt{AK}}{\mu_0 M_s^2}, \tag{1.14}$$

where A is the exchange constant [2].

The dependence of the coercivity H_C on the particle size is depicted in Fig. 1.7(a). As can be seen, in both single & multi-domain regimes, at first H_C increases to a certain maximum and then decreases as the particle size reduces. When the particle size reaches to a so-called superparamagnetic size limit r_{SPM}, H_c vanishes entirely.

In single-domain particles, the magnetization occurs through the homogeneous spin rotation towards the applying field direction. This implies that the magnetization processes are solely prevailed by the spin rotation and the DWs play no substantial role. This can account for the higher H_c usually being

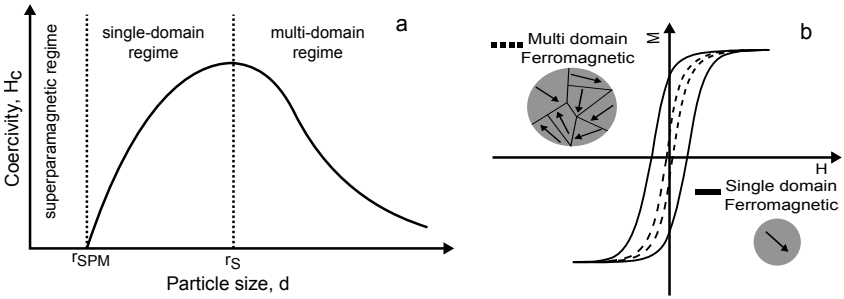

Figure 1.7: (a) Size dependent coercivity in single & multi-domain and superparamagnetic particles and (b) $M - H$ hysteresis loops of single and multi-domain ferromagnetic materials.

observed in single-domain particles compared to multi-domain ones as shown in Fig. 1.7(b). Different magnetization responses originate from the fact that a much higher energy is required to homogeneously rotate the spins than the DWs. The rotation of the DWs can be hindered by extrinsic phenomena such as pinning to impurities and grain boundaries and intrinsic including magnetocrystalline and surface anisotropies.

1.2.3 Superparamagnetism

Superparamagnetic particles are considered to be a special type of single-domain particles in which the balance between the thermal fluctuation k_BT and magnetic anisotropy energy $E(\Theta)$ energy defines the dynamics. As temperature increases, k_BT becomes bigger and eventually at some point it overcomes the energy barrier E_B (cf. section 1.2.1). In this situation, the spins fluctuate quickly and there will be no stable magnetization and thereby the net magnetization can be described by paramagnetic model. Since in this case magnetic moments in a single particle are a group of moments with a much larger net moment compared to an atomic moment of a paramagnet, the system is called superparamagnetic. The superparamagnetism and magnetic anisotropy are two closely related concepts. The superparamagnetism appears when the anisotropy energy barrier E_B can be overtaken by thermal fluctuations and consequently its condition is given by [7]

$$E_B = KV = 25k_BT_B^{sp}. \tag{1.15}$$

It can be deduced that superparamagnetism depends strongly on temperature. Above a certain temperature known as the superparamagnetic blocking temperature T_B^{sp} and in zero magnetic field, the thermal fluctuation is comparable with E_B and thus the net magnetization is zero. However, in an external DC field, the spins start to orient in the field direction as depicted in Fig. 1.8. The superparamagnetic blocking temperature T_B^{sp} is the temperature at which the maximum magnetization is achieved in the zero field cooled (ZFC) magnetization branch. Typical field cooled (FC) and ZFC magnetizations recorded for 13 nm

magnetite nanoparticles are displayed in Fig. 1.9. Generally, below the T_B^{sp} the spins are blocked to the magnetocrystalline anisotropy axis and thereby the superparamagnetism diminishes.

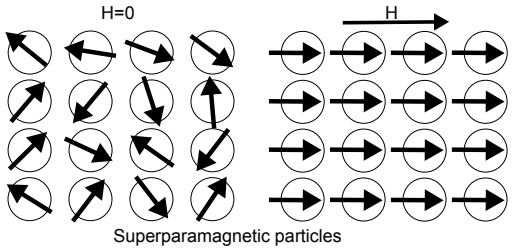

Figure 1.8: Typical behavior of superparamagnetic particles in absence and presence of a magnetic field.

In superparamagnetic particles, the anisotropy energy is comparable to the thermal energy, resulting in flipping of the spins around the anisotropy axis known as the Néel relaxation mechanism. Whereas, in FM particles, the magnetic moment is blocked to the anisotropy axis and the whole particle rotates recognized as the Brownian relaxation process. The relaxation mechanisms in superparamagnetic iron oxide nanoparticles (SPIONs) will be thoroughly discussed in the next section.

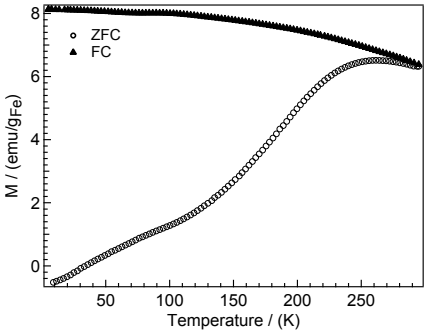

Figure 1.9: FC and ZFC magnetizations obtained for 13 nm magnetite nanoparticles.

The magnetization of non-interacting particles can be modelled by the Langevin function given by

$$L(m, H_{mag}) = \coth(\xi) - \frac{1}{\xi} \qquad \text{with} \qquad \xi = \frac{\mu_0 m H}{k_B T}, \tag{1.16}$$

where k_B is the Boltzmann's constant and m is the particle magnetic moment. The Langevin function can be simplified to $\xi/3$ and $1 - 1/\xi$ for small and

high field values, respectively. The superparamagnetic nanoparticles $M - H$ hysteresis loops can be reconstructed with the Langevin function by assuming that the particles are non-interacting. The particle mean core size and standard deviation can be approximated from the fit provided a certain shape for the size distribution function. For instance, it is agreed that the size distribution shows a Gaussian shape for particles synthesized via colloidal syntheses.

1.2.4 Relaxation mechanisms in SPIONs

The SPIONs reveal different dynamic behavior which needs to be studied and understood, particularly when biomedical applications are targeted. Firstly, some basic concepts such as magnetic core size d_c and hydrodynamic size d_{hydro} have to be defined. Schematically illustrated in Fig. 1.10, the d_c is the diameter of magnetic material in the center of a particle, responsible for magnetic responses. The d_{hydro} is the diameter of the magnetic core plus the thickness of a surrounding shell (designated as hydrodynamic shell). The SPION magnetic moments are aligned in the direction of an applied magnetic field and tend to randomly reorient due to thermal agitation when the magnetic field is switched off. It appears that the magnetic relaxation is an intrinsic behavoir of the SPIONs due to their superparamagnetic nature.

Brownian relaxation

Theoretically, the SPIONs relax via two different relaxation mechanisms. The Brownian relaxation for spherical particles is defined by the rotation of the whole particle around its center of mass and its time constant may be written as

$$\tau_{Brown} = \frac{\pi \eta d_{hydro}^3}{2 k_B T}, \tag{1.17}$$

with η in mPa s the viscosity of the suspending solution and $k_B = 1.3806 \times 10^{-23}$ the Boltzmann's constant in $\mathrm{m^2 kg\ s^{-2}}$. Principally, in the Brownian relaxation process, the inner magnetic moment is blocked to the magnetocrystalline anisotropy axis and thus the whole hydrodynamic volume rotates (see Fig. 1.10).

Néel relaxation

The second relaxation mechanism, describing the flipping of the inner magnetic moment (i.e. atomic magnetic moment) around its magnetocrystalline anisotropy axis, is called the Néel relaxation and is visualized in Fig. 1.10. The Néel relaxation time for spherical magnetic cores can be described by

$$\tau_{Néel} = \tau_0 \exp\left(\frac{K \pi d_c^3}{6 k_B T}\right), \tag{1.18}$$

in which K is the effective magnetocrystalline anisotropy constant and its given values in literature vary from 7 to 20 KJ $\mathrm{m^{-3}}$. The pre-exponential

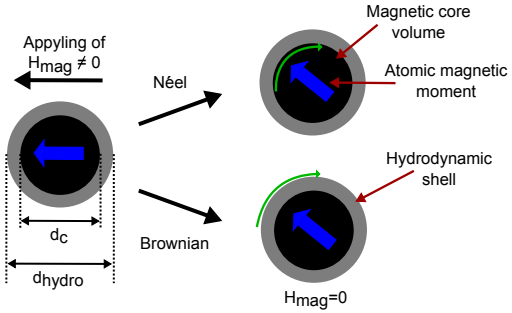

Figure 1.10: Brownian and Néel relaxation mechanisms in superparamagnetic nanoparticles.

parameter τ_0 changes from 10^{-8} to 10^{-12} s. It appears that the Néel relaxation depends exponentially on the magnetic core volume $V_{core} \propto d_c^3$. To measure the Néel relaxation, the Brownian one should be suppressed by means of particle immobilization (designated as immobile sample) in inorganic (e.g. gypsum) or organic (e.g. mannitol, agarose) matrices.

Effective relaxation

The Brownian and Néel relaxation processes happen at different time scales depending on the particle hydrodynamic and core sizes. Also, the fastest relaxation mechanism dominates and prevails the relaxation process. Nevertheless, in a real ferrofluid (liquid suspension of SPIONs) due to the size distribution which exists inevitably, both relaxations occur simultaneously and thus each of them contributes to the total relaxation process to some extent. The total relaxation may be called the effective relaxation which can be given by [9]

$$\tau_{eff} = \frac{\tau_{Brown}\tau_{Néel}}{\tau_{Brown} + \tau_{Néel}}. \tag{1.19}$$

The Brownian, Néel and effective relaxation time τ for 19 nm spherical iron oxide NPs suspended in chloroform with the hydrodynamic shell thickness of 2 nm (typical value taken for oleic acid coated NPs) and the anisotropy constant of 7 KJ m^{-3} were simulated by employing Eqs.1.17, 1.18 and 1.19. The relaxation time versus core and hydrodynamic diameters are plotted in Fig. 1.11.

By looking at Fig. 1.11, an exponential dependence of the Néel relaxation and a third polynomial dependence of the Brownian relaxation on core and hydrodynamic diameters, respectively, are discernible. It can be seen that the relaxation lines intersect at $\approx d_c = 21$ nm, showing that the particles with a smaller d_c (point 1) relax via the Néel process regardless of being mobile or immobile. On the contrary, the ones with a bigger d_c relax either via the Brownian or Néel processes depending on their mobility (points 2 and 3). This means that if the particles rotate freely (point 2), the Brownian process prevails the relaxation, otherwise the Néel process dominates (point 3). Likewise, when

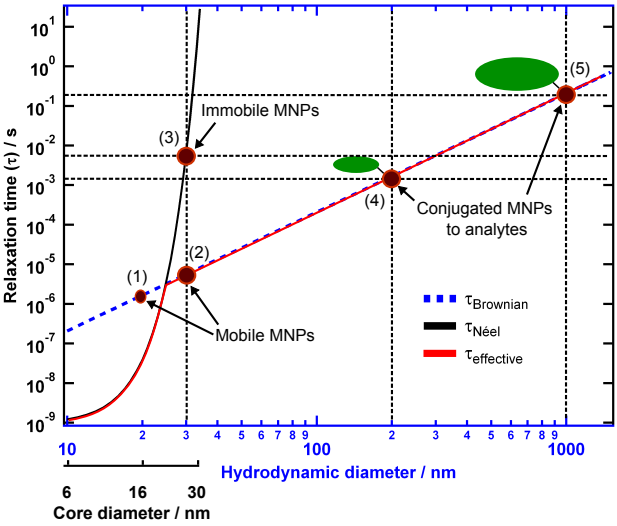

Figure 1.11: Brownian, Néel and effective relaxation time versus core and hydrodynamic diameter for small field amplitudes. The simulation parameters are $d_c = 19$ nm, $\delta = 2$ nm, $K = 7$ KJ m^{-3}, $\tau_0 = 10^{-9}$s, $T = 298$ K.

the particles conjugate to analytes their hydrodynamic size grows, resulting in the increased relaxation time (point 4). Eventually, binding to micro-size analytes triggers a situation in which the particles experience an immobile state and thus the Brownian and Néel time constants are comparable. By further increase of the length of the bound analytes, these will be a situation at which the Brownian relaxation becomes slower than the Néel (point 5 in Fig. 1.11) and consequently the particles tend to relax via the latter process. The concept of switching between relaxation processes via conjugation of analytes with different sizes is the core idea of utilizing magnetorelaxometry as a tool for performing qualitative and quantitative magnetic bioassays.

2 Iron oxide nanoparticles: synthesis, functionalization and applications

Dimensionally and magnetically controlled synthesis of MNPs has gained a significant attention since a decade ago due to their exceptional properties, making them an indispensable candidate for a variety of nanoparticle-based diagnostics and therapeutics. Nowadays, it is widely accepted that physicochemical properties of MNPs such as size distribution, morphology, magnetization, surface chemistry, etc. depend strongly on synthesis method. Also, it is known that tailor-made MNPs are needed to meet the requirements of a specific usage. To date, numerous solution phase chemical syntheses have been employed to fabricate a colloidal suspension of MNPs. Among various procedures, colloidal organometallic syntheses appear to be the most attractive ones regarding size uniformity, crystal perfection and magnetic properties of the resulting MNPs. These synthesis methods result in hydrophobic MNPs, solely dispersible in non-polar solvents, and need to be transferred into water. The phase transfer is an essential necessity for biomedical applications and has been a great challenge by itself. Having particles pulled into water, their cytotoxicity, surface chemistry and long-term stability have to be examined. Finally, one should be able to target a possible application for the synthesized particles based on their structural, magnetic and chemical properties. In this chapter, the major particle synthesis and phase transfer strategies which have been used in the last two decades, their merits and drawbacks will be addressed.

2.1 Iron oxide

Iron oxide can be found in four different phases in nature including $Fe_{1-x}O$ (wüstite), $\alpha - Fe_2O_3$ (hematite), $\gamma - Fe_2O_3$ (maghemite) and Fe_3O_4 (magnetite). Traditionally, they are widely used as iron ores and inexpensive pigments in paints and coatings. In the last two decades, medical and bioanalytical applications of iron oxide nanoparticles have been found particularly by the emerging and growing of nanotechnology and nano-biotechnology. Nowadays, magnetic iron oxide nanoparticles are one of the most commonly used medical agents for a wide variety of diagnostics and therapeutics such as magnetic resonance imaging (MRI) [10–12], hyperthermia [13], homogeneous magnetic bioassays [14–20], magnetic particle imaging (MPI) [21] and targeted drug delivery [22, 23] due to their biocompatibility and non-toxicity.

Wüstite

Wüstite has a defective salt-like crystallographic structure ($Fm\overline{3}m$, space group No. 225 and the nominal lattice *d*-spacing of 4.303 Å). In its unit cell, oxygen atoms occupy the main face-centred cubic (fcc) sites and Fe^{2+} cations fill all octahedral interstitial sites as visualized in Fig. 2.1. The presence of many vacancies in its structure causes the diffusion of Fe^{2+} cations towards the surface and their oxidation to Fe^{3+}. This means that wüstite is a thermodynamically unstable phase which tends to oxidize to magnetite by being exposed to air. Regarding the magnetic properties, wüstite shows antiferromagnetic (AFM) bahavior, revealing a negligible magnetic response even in the presence of a magnetic field owing to its anti-parallel spin configuration (cf. Fig. 1.3).

Magnetite

Magnetite has a cubic crystal structure with the space group of $Fd\overline{3}m$ (No. 227). Theoretically, the unit cell is made up of eight cubic units with the lattice *d*-spacing of 8.396 Å. It contains 56 atoms including 32 oxygen atoms, 16 Fe^{3+} and 8 Fe^{2+} and may be denoted as $\left(Fe^{3+}\right)_8^{tetr}\left[Fe^{3+}Fe^{2+}\right]_8^{oct}O_{32}$. In its unit cell as shown in Fig. 2.2(a), oxygen onions form a closed-packed fcc lattice. Also, there are 32 octahedral (B site) and 64 tetrahedral (A site) sites in the unit cell. The Fe^{2+} cations occupy 1/4 of the octahedral sites (i.e. 8 Fe^{2+}) and Fe^{3+} ones evenly fill 1/4 of the octahedral (i.e. 8 Fe^{3+}) and 1/8 of the tetrahedral (i.e. 8 Fe^{3+}) sites. This crystallographic configuration is called inverse spinel.

From the spin configuration point of view, magnetite is a ferrimagnetic (FIM) material. Its magnetic properties are reflected by the splitting of the 3d orbitals in octahedral and tetrahedral sites as visualized in Fig. 2.2(b) and (c). The 3d orbitals are split into two subsets called e_g and t_{2g} in octahedral sites and t_2 and e in tetrahedral ones due to the influence of oxide ligands. These spin configurations reveal that Fe^{3+} and Fe^{2+} ions have five and four unpaired electrons, respectively. As can be seen, in the octahedral coordination, Fe^{3+} and Fe^{2+} ions are coupled ferromagnetically through the double exchange

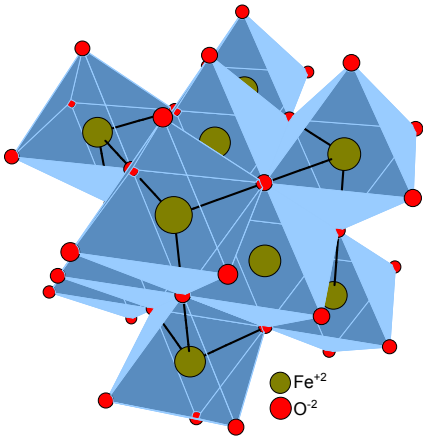

Figure 2.1: Wüstite crystal structure with the space group of $Fm\bar{3}m$ cubic lattice.

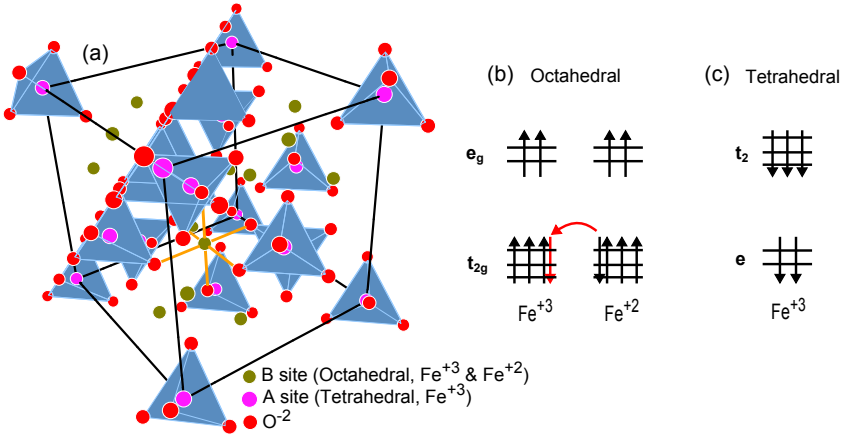

Figure 2.2: (a) Magnetite crystal structure with the space group of $Fd\bar{3}m$ cubic lattice and the visualization of 3d orbitals splitting in (b) octahedral and (c) tetrahedral environment.

mechanism. The electron whose spin is directed in the opposite direction of the others and colored red, can be exchanged between two octahedral coordination sites. On the other hand, the Fe^{3+} ions in tetrahedral and octahedral sites are coupled antiferromagnetically via the superexchange mechanism. This implies that the Fe^{3+} spins cancel out each other and thus merely unpaired spins of Fe^{2+} in octahedral coordination contribute to the magnetization. This magnetic moment configuration accounts for the ferrimagnetism seen in magnetite.

Maghemite

Likewise to magnetite, maghemite has a cubic crystal structure with the lattice d-spacing of 8.33 Å. As it can be deduced from its chemical formula $\gamma - Fe_2O_3$, the only existing Fe^{3+} cations are arbitrarily distributed in 16 octahedral and 8 tetrahedral interstitial sites within the fcc packing of oxygen anions as shown in Fig. 2.3. The Fe^{2+} cation vacancies ($\otimes$) are located in the octahedral sites and their arrangement in the maghemite structure plays a preponderant role in magnetic response of maghemite. When the vacancies are randomly distributed its space group is $Fd\bar{3}m$ (No. 227) and its formula unit may be written as $\left(Fe^{3+}\right)_8^{tetr}\left[Fe^{3+}_{5/3}\otimes_{1/3}\right]_8^{oct} O_{32}$. The described crystal arrangement is known as normal spinel [24]. Since the spins in the octahedral and tetrahedral sites are oriented anti-parallel, maghemite is ferrimagnetic.

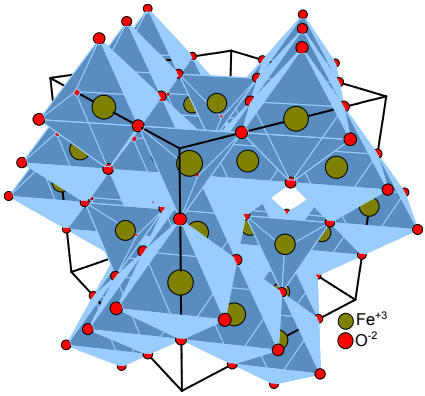

Figure 2.3: Maghemite crystal structure with a cubic crystal structure $Fd\bar{3}m$.

2.2 Synthesis of iron oxide nanoparticles

2.2.1 Co-precipitation

Co-precipitation is a conventional procedure for the fabrication of iron oxide particles such as magnetite (Fe_3O_4) and maghemite (Fe_2O_3) [1]. Normally, the reaction solution consists of a mixture of ferric and ferrous precursors dissolved in a highly basic solution which leaves to react at room or elevated temperatures. In a typical synthesis of magnetite, to a mixture of Fe^{2+} and Fe^{3+} chloride at a 1:2 molar ratio, a basic solution (pH between 8-14) is added dropwise under an inert atmosphere. The overall reaction may be written as

$$Fe^{2+} + 2Fe^{3+} + 8OH^- \rightarrow Fe_3O_4 + 4H_2O \tag{2.1}$$

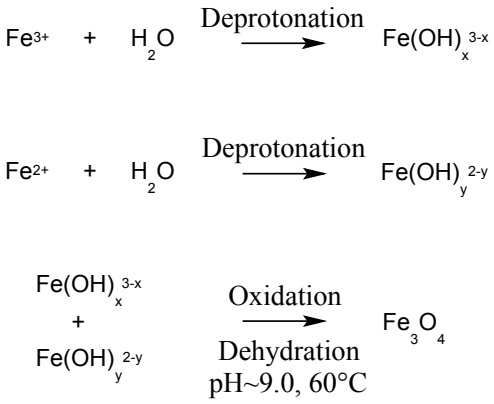

Figure 2.4: Schematic representation of the formation of magnetite particles via co-precipitation of ferric and ferrous chloride salts.

and shown schematically in Fig. 2.4. In one the earliest studies, Massart demonstrated the synthesis of nearly spherical 8 nm magnetite NPs using alkaline precipitation of ferric and ferrous chloride salts under nitrogen [25]. Soon after, it was realized that by adding surfactants to the reaction solution that Massart engineered, a better control over size distribution can be achieved. Lee et al. [26] showed that by adding polyvinlyalcohol (PVA), 4-10 nm magnetite NPs can be stabilized.

The particle physical and chemical properties depend strongly on the nature of the iron salt (chlorides, sulfates, and nitrates), the ferric to ferrous ions ratio, the reaction temperature, the pH value, the ionic strength of the media, etc. Apparently, having a reasonable control over the long listed influential parameters is not a trivial task and thus the reproducibility and robustness of this method is controversial [27]. However, yet the co-precipitation is considered as the easiest procedure for high yield fabrication of iron oxide NPs.

In the same way, the particles fabricated through this approach show a relatively poor crystallinity and imperfect spin ordering on the surface. These phenomena lead to a lower M_s value (30-80 emu g^{-1}) compared to the one reported for bulk iron oxide (90-100 emu g^{-1}) in literature. Besides, the resulting particles via this method show a polydisperse distribution, leading to a broad range of blocking temperatures which eventually hinders their usage for some applications. This feature limits the feasibility of using particles for instance in homogeneous bioassays where size monodispersity is highly required [2].

2.2.2 Hydrothermal synthesis

Due to a remarkable dependence of iron oxide NPs performance on size distribution, crystallinity, surface ordering, etc., there has always been a trend to come up with new synthesis procedures in which less reaction parameters are involved compared to the co-precipitation. The answer was found in performing

the synthesis reaction at higher temperatures and under autogenous or external pressure, which is called hydrothermal synthesis. By applying this method one can have a good control over shape and size distribution especially with the help of surfactants. The hydrothermal method is rather easy to handle since a dozen synthesis parameters such as stirring, dropping rate of the basic solution, precursor injection temperature, etc., affecting the particle properties in the co-precipitation technique, have no contribution. However, usually the resultant particles suffer from a relatively strong aggregation happening during the synthesis. Moreover, since a combination of high temperature and pressure is used, the risk of solid state fusion in addition to general agglomeration is high. In one of the most remarkable studies, Li et al. [28] developed a general strategy for the fabrication of different types of nanoparticles including noble metal, magnetic and superconducting via a liquid-solid-solution reaction. In a typical experiment, a mixture of metal linoleate (solid), ethanol-linoleic acid (liquid) and ethanol-water (solution) was treated under hydrothermal conditions and resulted in 9 nm Fe_3O_4 NPs.

2.2.3 Microemulsion

Microemulsion is a solution phase synthesis which has been recently employed for preparation of metallic and oxide NPs with defined size and shape distribution. A microemulsion is a dispersion of two immiscible liquids: an aqueous and oily phase. There are two types of microemulsion; water-in-oil (W/O) and oil-in-water (O/W). The former one known as reverse micelles is the most widely used. In a typical microemulsion synthesis, water microdroplets are generated in a mixture of an oily phase and surfactants. The synthesized micelles act as micro-reactors, each one having a specific volume which can be tuned by varying the water to surfactant ratio. A water microdroplet is surrounded by an interfacial layer of surfactants and contains a certain amount of metal salts acting as a precursor. The metal salt is subjected to a reduction process and eventually particles are formed inside microdroplets. The availability of the precursor inside micelles determines the particle growth rate [2, 29]. The synthesis reactions are usually carried out at room temperature and under inert atmosphere. The group of Pileni reported the synthesis of Co NPs in a microemulsion system of $Na(AOT) - Co(AOT)_2 -$ water $-$ isooctane which was reduced by sodium borohydride. They also showed the possibility of synthesizing Fe-Cu composite alloy using the same technique [30]. By reducing a micellar solution of ferrous dodecyl sulfate $Fe(DS)_2$ prepared from sodium dodecyl sulfate Na(DS) and ferrous chloride $Fe(Cl)_2$, Pileni et al. synthesized iron ferrite NPs with a size tunable from 4 to 12 nm [31]. Carpenter and co-workers demonstrated the applicability of this method for synthesizing gold-iron core-shell structures using a micellar solution of water, octane and cetyltrimethylammonium bromide (CTAB) [32]. This technique has some certain drawbacks. The major one is related to an amorphous nature of the synthesized NPs. To crystallize the particles, a calcination treatment is applied, causing an inevitable particle agglomeration and coagulation. Besides, the resulting NPs reveal a broad size distribution and also the production yield is rather low compared to the co-precipitation method [33].

2.2.4 Thermal decomposition

Along with the co-precipitation, thermal decomposition is one of the most studied synthesis procedures which has been considered as the most appropriate process for dimensionally controlled synthesis of various types of NPs. Thermal decomposition is classified into two general methods: hot injection and heating up. In 1993, Bawendi and co-workers launched the hot injection as a simple route for the fabrication of high quality semiconductor nanocrystals [34]. In this method the nucleation is induced by rapid injection of organometallic precursors into a hot mixture of solvent and surfactants, resulting in a sudden and short nucleation step which is followed by a slow growth step; two key criteria for synthesizing monodisperse NPs [35]. In a prime example, Alivisatos and co-workers investigated the growth kinetics of colloidal semiconductor nanocrystals synthesized via the rapid injection of a cold mixture of Se:$Cd(CH_3)_2$:tributylphophine into 360°C trioctylphosphine oxide (TOPO) solution [36]. They also pioneered a new hot injection decomposition of an iron Cupferron complex (Cup; *N*-nitrosophenylhydroxylamine, $C_6H_5N(NO)O^-$) as an efficient route for the synthesis of relatively monodisperse maghemite $\gamma - Fe_2O_3$ NPs with a core size of 10 nm [37]. Since the invention of the hot injection decomposition by the Bawendi and Alivisatos groups, numerous studies have been dedicated to providing a deeper understanding of the mechanisms by which particles nucleate and grow [38–43]. This method offers particles with relatively narrow size distribution and high crystal quality, however a dozen preparation steps need to be handled carefully under inert atmosphere, making the whole process quite complicated. Besides, the synthesized NPs show a moderate monodispersity $\delta d_c \approx 10\%$ and further narrowing of the size distribution can only be achieved by size-selective fractionation processes.

Shortly after, the group of Hyeon pioneered another thermal decomposition synthesis methodology based on the heating of a reaction mixture (precursor, solvent and surfactant) up to the reflux temperature of the solvent (usually long chain hydrocarbons such as 1-octadecene, 1-eicosane, etc.) which later on was named heating up decomposition [44, 45]. In this method, iron-oleate synthesized through a mild reaction between $FeCl_3 \cdot 6H_2O$ and sodium oleate at moderate temperature was used as an iron source. The iron-oleate is an environmentally friendly compound and compared to the other common iron precursors such as iron pentacarbonly $Fe(CO)_5$ is less expensive and easier to handle. They demonstrated that by varying reaction temperature and time, iron oxide NPs with a core size from 5 to 22 nm can be produced [44]. Also, they showed the capability of extending this method for the fabrication of other metal oxides such as MnO, CoO, ZnO, $MnFe_2O_4$ and $CoFe_2O_4$. Compared to the hot injection synthesis, the heating up decomposition is less complicated and the synthesized NPs show even a narrower size distribution, allowing one to skip tedious size selection processes. The same group reported a two step synthesis protocol for producing maghemite NPs with a core size between 6 and 15 nm with an exceptional size dispersity. In this procedure, the iron-oleate precursor was synthesized via in-situ reaction of oleic acid and iron pentacarbonly $Fe(CO)_5$ at 403 K in dioctyl ether. The initially resultant iron NPs were further subjected to a controlled oxidation using anhydrous trimethylamine *H*-oxide $(CH_3)_3NO$

as an organic oxidizer and transformed to maghemite NPs [46]. Although they showed the possibility of increasing particle size by a single atomic layer, the two step procedure seems to be sophisticated.

Colvin and co-workers demonstrated the possibility of merging both precursor and particle syntheses in one single process by using FeO(OH) as an iron source [47]. In this process, a mixture of FeO(OH), oleic acid and 1-octadecene is heated for several hours, leading to synthesizing monodisperse magnetite NPs. They showed the particle size increases linearly as the molar ratio of oleic acid to FeO(OH) becomes larger. They also found out that by increasing reaction temperature to 340°C, particles with larger sizes 20-30 nm can be synthesized, but high temperature aging spoils the particle size distribution considerably. Another very promising synthesis strategy in this category was proposed by Sun et al. in which 4 nm magnetite NPs were synthesized via heating up a mixture of iron acetylacetonate $Fe(acac)_3$, phenyl ether, 1,2-hexadecanediol, oleic acid and oleylamine to reflux for half an hour. By using the synthesized tiny NPs as seed, they launched a new strategy for producing large monodisperse NPs. This method later on was called seed-mediated growth [48]. Using the seed-mediated growth approach, Zhang and co-workers fabricated spherical and cubic $CoFe_2O_4$ NPs. They showed that the particle shape can be tuned by varying the growth rate.

As mentioned earlier, formation of NPs is comprised of two steps: nucleation and growth. Practically, to synthesize monodisperse NPs, one should know about nucleation and growth theories in solution based syntheses. Therefore, in the following sections, we briefly review their principles and discuss how one can apply the theories in a real synthesis experiment.

2.3 Synthesis of monodisperse nanoparticles

The theory and mechanism of synthesizing monodisperse colloidal suspensions were originally proposed by La Mer & Dinegar in 1950 [49]. In their study, they showed that to fabricate particles with a well-defined size distribution, the nucleation and growth processes should occur at two different temperatures. This nucleation and growth concept became known as La Mer model and has been exploited extensively to design new solution phase syntheses since it was discovered. To gain a deeper understanding of the La Mer model, the theory of nucleation and growth in solution based syntheses should be reviewed.

2.3.1 Nucleation

In the colloidal synthesis of nanoparticles, several processes are involved. The first one is called pre-nucleation step in which the precursor is transformed into solutes, the species (atoms, ions, molecules) which from now on are denoted by monomers. By random gathering of monomers, initial solid matters (designated as embryos) are born in solution, primarily triggering by thermal fluctuation. The total free energy of the formation of a n-monomer embryo has a Gibbs-like

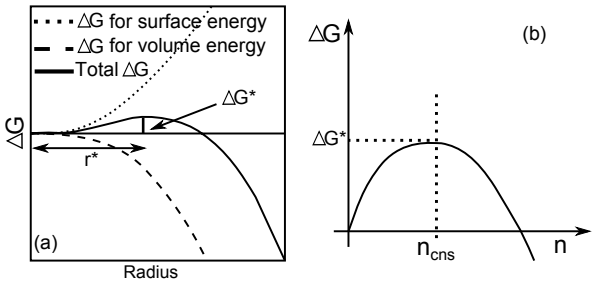

Figure 2.5: Total free energy of nucleation as a function of (a) radius and (b) critical nucleus size.

form and may be given by

$$\Delta G = \Delta G_{volume} + \Delta G_{surface} \Longrightarrow \Delta G = -nk_BT\ln(\frac{C(t)}{C_0}) + 4\pi a^2 n^{2/3}\gamma, \quad (2.2)$$

with n the number of solutes made the embryo, $C(t)$ the monomer concentration at a given reaction time, C_0 the monomer initial concentration, a the effective monomer radius, n the number of constituent monomers of an embryo and σ the surface tension [50]. From Eq. 2.2, it can be deduced that the free energy of formation is defined by the competition between volume and surface energies as plotted in Fig. 2.5(a). In a simple definition, the volume contribution is a gain of energy and thus favourable. On the contrary, the formation of a new surface costs energy and hence is thermodynamically not desirable. The critical nucleus size n_{cns} can be obtained by finding the maximum of ΔG as illustrated in Fig. 2.5(b) and can mathematically be expressed by [51]

$$\frac{\partial \Delta G}{\partial n} = 0 \Longrightarrow n_{cns} = (\frac{8\pi a^2\sigma}{3k_BT[\ln(S)]})^3, \text{with } S = \frac{C(t)}{C_0}, \quad (2.3)$$

with S the relative monomer supersaturation.

And consequently the critical energy barrier ΔG^* of the formation of a stable embryo is obtained by inserting n_{cns} from Eq. 2.3 into Eq. 2.2 and may be written as

$$\Delta G^* = \frac{256\pi^3 a^6 \sigma^3}{27(k_BT)^2[\ln S]^2}. \quad (2.4)$$

Theoretically, an embryo with $n = n_{cns} + 1$ is considered to be stable (a so-called supercritical embryo) and eventually becomes a particle. Any embryo with $n < n_{cns}$ (so called subcritical embryos) blinks for a moment and goes off by redissolving into solution. In other words, the nucleation may be defined as the first irreversible formation of a nucleus (an embryo with $n > n_{cns}$) of the new equilibrium phase. The nucleation rate can be modelled using the Arrhenius form of ΔG^* and may be expressed by

$$\rho(t) = c(t)^2 K_{nc} \exp(\frac{-\Delta G^*}{k_BT}), \text{with } K_{nc} = 4\pi a n_{cns}^{(1/3)} D, \quad (2.5)$$

in which $c(t)$ is the concentration of the embryos consisting of only one monomer at a given time of t and D is the diffusion coefficient of the monomers. Assuming that n-solute embryos are spherical and the monomer packing density within a single embryo is likewise to the random loose packing of spheres, that is 58%, then the embryo radius is $an^{1/3}$ as seen in Eq. 2.5. K_{nc} is the Smoluchowski growth rate describing the irreversible capture of diffusing monomers by nuclei [50]. By looking at Fig. 2.5(b), it can be deduced that the formation of the embryos is not a thermodynamically favorable process since it causes an increase of the free energy.

2.3.2 Growth

After the completion of the nucleation step, the freshly formed tiny crystallites go through a growth step. Depending on the relation between the monomer concentration at the solid/liquid interface C_i and the solubility of the solid (i.e. the particle) C_r, the particles experience two growth modes: diffusion or reaction controlled. The diffusion controlled growth mode was theoretically established by Reiss [52] in which the growth occurs via the diffusion of the monomers from the bulk solution C_b to the solid/liquid interface through a diffusion layer δ which capes each particle. The microscopic view of the diffusion is visualized in Fig. 2.6(a). The monomer flux towards the particle surface can be expressed by applying Fick's first law of diffusion as

$$J = 4\pi x^2 D \frac{dC}{dx}, \tag{2.6}$$

with D the diffusion coefficient of the monomer and x the radius of a spherical plane inside the diffusing layer δ. Provided that there is a constant monomer supply, it can be deduced that J is constant regardless of the value chosen for x. Consequently, Eq. 2.6 can be solved by integration of $C(x)$ from $(r + \delta)$ to r with respect to x and may be written as

$$J = \frac{4\pi D r(r + \delta)}{\delta}(C_b - C_i), \tag{2.7}$$

and considering that $\delta \gg r$, Eq. 2.7 can be rewritten as

$$J = 4\pi r D(C_b - C_r). \tag{2.8}$$

After being carried to the solid/liquid interface, the monomers react on the surface and the growth is initiated. The monomer consumption rate J via the surface reaction can be expressed by

$$J = 4\pi r^2 k(C_i - C_r), \tag{2.9}$$

in which k is the reaction rate coefficient. In general, the growth rate dr/dt can be expressed by a linear equation as

$$\frac{dr}{dt} = \frac{V_m}{4\pi r^2} J, \tag{2.10}$$

with V_m the particle volume. Broadly speaking, the slowest growth mechanism determines the overall growth rate. If $D \ll kr$ and $C_i \approx C_r$, the monomer diffusion is the rate determining step and thereby the growth is prevailed by the diffusion controlled mode. The monomer concentration profile in this growth mode is illustrated in Fig. 2.6(b). The growth rate can be obtained by substituting Eq. 2.8 into Eq. 2.10 and be given by

$$\frac{dr}{dt} = \frac{V_m D}{r}(C_b - C_i). \tag{2.11}$$

As can be deduced from Eq. 2.11, the linear growth rate is inversely proportional

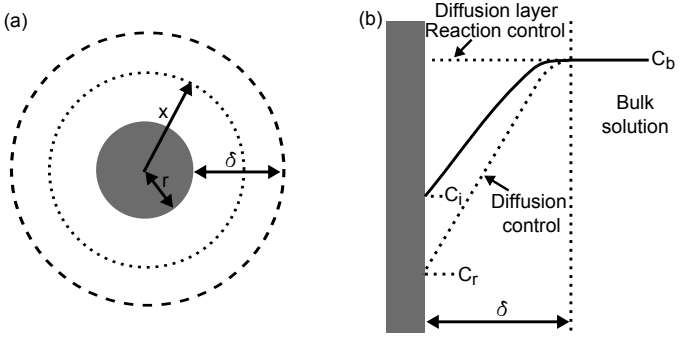

Figure 2.6: The monomer diffusion model through the diffusing layer δ (a) and the monomer concentration profiles of diffusion and reaction controlled growth modes (b).

to the particle radius. This implies that smaller particles grow faster than bigger ones and as a result the size distribution becomes narrower during the growth. Owing to this feature, the Reiss growth model is refereed to as the "size focusing" model as long as the chance of an additional nucleation is skipped. By continuation of the growth at some point, C_i becomes smaller than C_r at which the solid solubility is more favorable than the precipitation and further growth. In this circumstance, the particles shrink, dissolve in the bulk solution as the monomers and eventually re-precipitate. The smaller particles dissolve faster due to their higher curvature and potential. The dissolved monomers precipitate on the bigger particles and thereby the size distribution broadens. This phenomenon is known as the Ostwald ripening process [53].

On the contrary, when $D \gg kr$ and $C_i \approx C_b$ (as shown in Fig. 2.6(b)), the growth is controlled by the surface reaction and its rate can be obtained by inserting Eq. 2.9 into Eq. 2.10 and given by

$$\frac{dr}{dt} = kV_m(C_b - C_i). \tag{2.12}$$

2.3.3 La Mer model

La Mer and Dinegar [49] proposed that the whole process of the formation of particles in solution phase syntheses can be divided into four steps. The dependence of saturation S and nucleation rate on reaction time is shown in Fig. 2.7(a). As can be seen, in the first step, a so-called pre-nucleation step, the precursor is transferred to monomers and S increases gradually until it reaches the critical saturation level $S_{critical}$. In the second step, the solution becomes highly saturated with monomers and becomes ready to initiate an intensive and sudden nucleation. La Mer and Dinegar found that to synthesize monodisperse particles, the nucleation should be delayed to the time when this criterion is fulfilled. This nucleation mechanism is denoted by "burst nucleation". The occurrence of the burst nucleation causes an abrupt drop in the nucleation rate (the red curve in Fig. 2.7(a)) and S. The saturation falls below $S_{critical}$ implying that no further nucleation may occur. Next, a rapidly terminating growth step starts which does not last for a long time due to the lack of monomers. The highlighted region in the figure refereed to as "size focusing" is a window whereby all the available monomers are solely consumed for the growth. Since the diffusion controlled growth rate is very quick, at some point, S becomes equal to one. In this case, the solubility of particles C_r is bigger than the monomer concentration at the particle surface C_i, resulting in the occurrence of the Ostwald ripening processes and broadening of the size distribution as shown in the forth step.

To realize the La Mer nucleation and growth model in a real synthesis experiment, thermal decomposition behavior of the precursor has to be engineered. First of all, the precursor should start to decompose at a relatively high temperature and also in a narrow time/temperature range. In other words, high monomer concentration is required as depicted in Fig. 2.7(b). This condition provides a burst and delayed nucleation, two key criteria for the fabrication of monodisperse NPs. As can be seen in Fig. 2.7(b), at a lower monomer concentration (blue line), the system goes through a gradual nucleation mechanism whereby fewer nuclei with larger critical nucleus sizes n_{cns} are formed (cf. Eq. 2.3). And eventually the size defocusing mechanism spoils the size distribution in the course of growth. Apparently, a precursor with a gradual decomposition behavior is not optimal. Secondly, the nucleation should be intense enough to drop the saturation S well below the $S_{critical}$ to avoid an additional nucleation (multiple nucleation). This is solely achieved when the monomer concentration is high. However, for a period of time, the monomer concentration at the particle surface C_i should be bigger than C_r to trigger a size focusing mechanism as described in Reiss model (the blue window in Fig. 2.7(a)). On the contrary, when the monomer concentration is low, a gradual nucleation occurs over a long period of time, increasing the chance of multiple nucleation. Practically, this means that the growth temperature should be chosen precisely and based on the thermal decomposition behavior of the precursor. Besides, the growth temperature has to be high enough to provide a full decomposition of the precursor. Heating up the reaction mixture to a temperature which is not adequate for a complete decomposition may result in additional nucleations during the growth step.

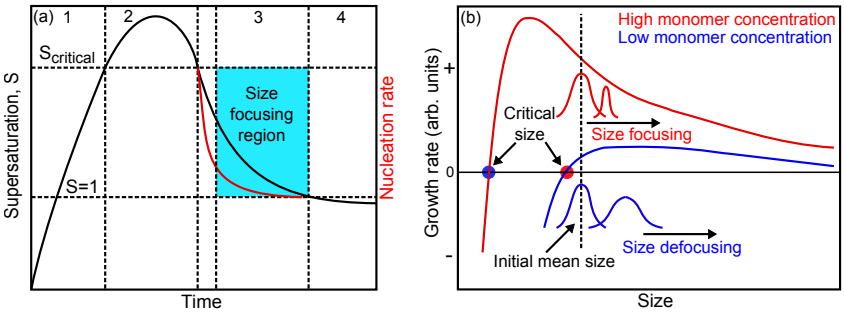

Figure 2.7: La Mer model representing (a) the change of supersaturation S as a function of reaction time and (b) the dependency of growth rate on monomer concentration.

Since La Mer and Dinegar established the model, there has been many attempts to realize the above mentioned criteria experimentally primarily via the hot injection method [54–57]. One of the most fascinating study was conducted by Puntes and Alivisatos in which they showed the feasibility of adapting the La Mer model for the case of cobalt NPs via injection of $Co_2(CO)_8$ in a mixture of *o*-dichlorobenzene, oleic acid and trioctylphosphine oxide (TOPO) [54]. They synthesized spherical and rod shaped cobalt nanocrystals. The heating up decomposition was also considered as a unique synthesis approach to realize the La Mer model. In this method, the engineering of the precursor thermal properties is even more crucial since in this case the nucleation and growth steps are not separated by an external force, that is the temperature drop after the injection in the hot injection method. One of the biggest contribution to this method was made by the group of Hyeon as discussed in the section 2.2.4.

2.4 Magnetic nanoparticles in biomedicine

The most important biomedical applications of MNPs are summarized in the flowchart shown in Fig. 2.8. Depending on size, physicochemical and magnetic properties, MNPs can be utilized either *in vitro* (i.e. an isolated biological environment) or *in vivo* (i.e. direct interaction with living organs in their real state). *In vitro* studies are usually conducted for diagnostic purposes whereas *in vivo* experiments can be used for both diagnostics and therapeutics. In the last decade, iron oxide NPs have been synthesized and optimized as a contrast agent for magnetic resonance imaging (MRI). There has been an increasing trend to assess their capability of being a tracer for *in vivo* imaging and detection of cancer tumors with MRI [10]. In the last few years, a huge progress was made in this field which has been demonstrated in a dozen scientific articles [11, 12]. Magnetic particle imaging (MPI) invented by Gleich and Weizenecker in 2005 [21] is an emerging modality which offers the potential of three-dimensional imaging with high sensitivity, high resolution and high imaging speed. In MPI, the quality and resolution of images depend significantly on the physical properties of MNPs [58, 59].

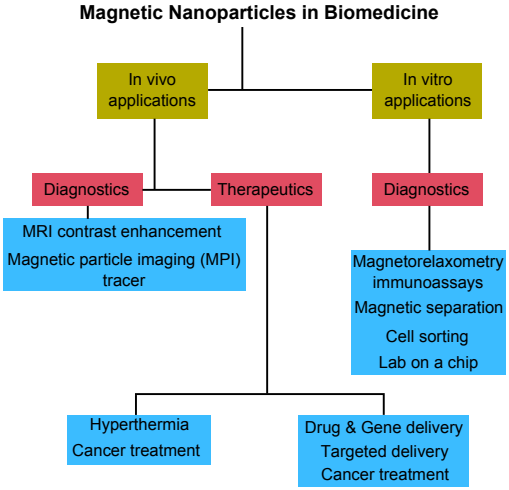

Figure 2.8: Flowchart summarizing different nanoparticle-based diagnostics and therapeutics.

In the last decade, it has been realized that magnetic NPs can be used in a wide variety of applications in which the particle response to dynamic magnetic fields (e.g. alternating and rotating) is exploited as a tool for detection of biological molecules [15–20]. Broadly speaking, these applications are based on the change in the particle Brownian relaxation time constant after the increase in their hydrodynamic size via binding to target molecules. Since the early study conducted by Widder et al.[60, 61] showing the potential of carrying drugs with magnetic microspheres to a targeted place where magnets were placed, the exciting fields of targeted drug delivery and nanomedicine have been emerged. The capability of using magnetic nanoparticles as a vehicle to carry drugs has been demonstrated in a handful of animal trials [22]. Currently, an efficient loading of drugs on the particles is a challenging topic for the researchers and thereby in some new studies the use of magnetic hollow spheres instead of nanoparticles was proposed due to their higher loading capacity [23].

2.4.1 Particle phase transfer

To prepare functional magnetic NPs for the above mentioned applications, their surface has to be engineered in a way to be water soluble, non-toxic and stable against particle interaction and agglomeration. Although it is possible to fabricate iron oxide NPs with a narrow size distribution using non-aqueous colloidal syntheses, these particles are usually capped with hydrophobic (e.g. oleic acid or oleylamine) groups and solely soluble in non-polar solvents. Hence an additional surface modification step is required to make them hydrophilic (so-called phase transfer). This topic has been a focus of several studies since the technological importance of magnetic ferrofluids have been realized [62, 63]. An

especial care should be given to this step since the particle magnetic performance should remain intact and also any particle clustering and agglomeration should be avoided. Broadly speaking, the phase transfer and water solubility strategies can be divided into two main groups: grafting on and grafting to the particle surface.

Grafting on methodology

This method is considered as the most used one in which the particles capped with hydrophobic chains are encapsulated with amphiphilic polymers. Amphiphilic polymers have two chain sides offering both hydrophilic and hydrophobic moieties. One can imagine that the hydrophobic moieties interact with carbon chain of oleic acid molecules via a so called hydrophobic interaction and the hydrophilic side facilitates water solubility and also further conjugation with proteins, antibodies, etc [63]. In a prime example, the group of Parak synthesized an amphiphilic polymer consisting of poly(maleic anhydride) backbone which offers spontaneous reaction with hydrophobic chains on the particles and the amino groups of target molecules and proteins. The transferred particles reveal a good water stability owing to the presence of negatively charged $-COO^-$ groups [64]. Yu et al. [65] coupled an inexpensive amphiphilic polymer, poly(maleic anhydride-*alt*-1-octadecene) (PMAOD), with poly(ethylene glycol) (PEG) via amidation and showed the feasibility of pulling oleic acid capped iron oxide NPs with variable sizes through encapsulation with PMAOD-PEG molecules. Later, Corato et al. [66] furthermore simplified the process by directly using PMAOD for phase transfer reaction without extra coupling with PEG moieties however, with a help of an amine containing cross-linker for stabilization. They showed that this phase transfer strategy is applicable for a wide range of metal, semiconductor and metal oxide nanoparticles.

Shytkova and co-workers took one step forward and proposed even a simpler strategy and proved no need to employ amine cross-linker [67]. They unravelled the configuration of poly(maleic acid-*alt*-1-octadecene) (PMAcOD) units on the particle surface by exploiting the small angle X-ray scattering technique. By applying a different approach, Zhang et al. [68] succeeded in pulling oleic acid coated nanoparticles into water by capping their surface with poly(acrylic acid) and poly(allylamine) via refluxing in hydrophilic glycol solvent at its boiling temperature. They showed that this process can be used for other types of nanocrystals, such as TiO_2 and quantum dots. In a study by Wu et al.[69], van der Waals interactions between oleylamine molecules on particles and fatty-acid chains of PEG sorbitan fatty-acid esters (so-called Tweens) was exploited to stabilize Fe_3O_4 NPs and quantum dots. This reaction was regarded as dual-interaction ligands. They found that the Tween functionalized particles reveal a higher stability compared to the ones stabilized with linear PEG derivative ligands. A typical process is schematically illustrated in Fig. 2.9. Although this process sounds rather straight forward and easy to handle, it is known that the hydrophobic interaction is sensitive to the environment [63].

Grafting to methodology

In the grafting to approach, the original hydrophobic molecules are replaced with hydrophilic ligands. Generally, the ligands comprise of two parts: an anchor and a spacer. To obtain a non-aggregated and stable aqueous suspension, particular attention should be given to the selection of both anchoring and spacer groups. Different anchoring groups such as silane [70, 71], dopamine [72], phosphate [73], nitrodopamine [74] and multidentate catechol have already been utilized [75]. Amongst different spacers, PEG, a synthetic polymer available in linear and branched forms, gains a lot of attention owing to its biocompatibility, versatility and increasing blood circulation time. For quite a long time, PEG has been used as a component in a broad range of pharmaceutical products [63]. Recently, there has been a growing trend to link PEG molecules to iron oxide NPs and hence different conjugation strategies have been proposed [71, 73–82]. The PEG coated particles are also known as "stealth" nanoparticles due to the fact that they are not seen by reticulo endothelial system (RES), making them an ideal candidate for cell labeling. Owing to its chemistry, PEG is dissolved in some organic solvents such as chloroform and toluene in addition to polar solvents. This especial feature enabled Kohler et al. [70] to graft PEG to oleyl amine/oleic acid coated iron oxide NPs dispersed in toluene. In another study, Amstad et al.[74] grafted PEG derivative compounds with different anchoring groups to 9 nm bare magnetite NPs which were originally suspended in N,N-Dimethylformamide (DMF) (polar solvent). Another remarkable feature of using PEG is its capability of being heterobifunctional which means having in one side the anchoring group and on the other side functional groups. The previous studies showed that a variety of functional moieties such as carboxyl, amine, thiol and hydroxyl can be linked to PEG chain which facilitate the conjugation of biological molecules. Lattuada and Hatton exchanged the oleic acid moieties with PEG molecules via employing a citric acid mediated procedure [83]. They proposed a rather general ligand exchange method enabling one to coat particles with other types of polymers such as poly(methacrylic acid) (PAA/PMAA), poly(hydroxyethylmethacrylate) (PHEMA), etc. Xu et al. [84] managed to stabilize oleic acid/TOPO iron oxide NPs via grafting poly(acrylic acid) (PAA) and polyethylenimine (PEI) to their surface using a mild ligand exchange reaction. A typical exchange of oleic acid molecules with nitrodopamine-PEG compounds is visualized in Fig. 2.9.

Coating with inorganic materials

Another method is the coating of iron oxide nanoparticles with inorganic shells such as silica [62]. This method has attracted a lot of attention in the last decade due to its advantageous features [85–89]. The main merits are the simplicity of the coating process and the inertness of silica which eventually offer a reliable protocol for the fabrication of nontoxic markers for biological applications. Another interesting feature is that usually one obtains a relatively thick shell of silica around the particles, reducing magnetic dipole-dipole interactions and facilitates particle stability [62]. In a typical synthesis experiment, firstly, the iron oxide magnetic cores are synthesized via the above mentioned methods and

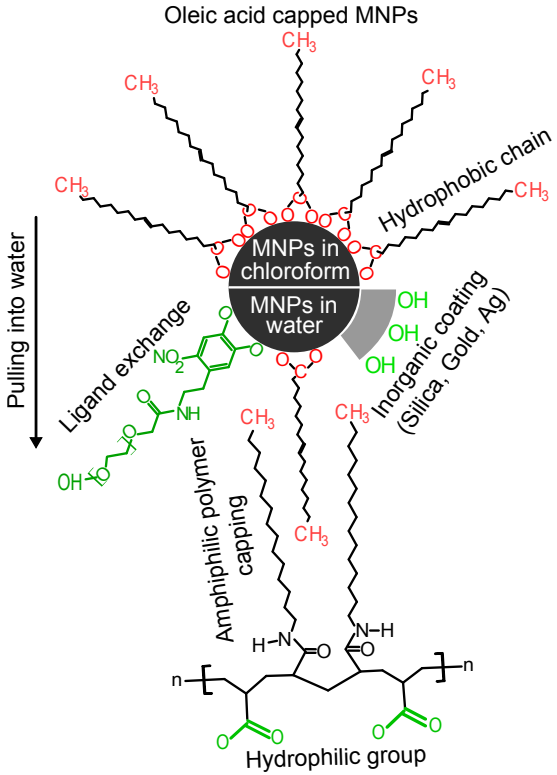

Figure 2.9: General strategies for transferring hydrophobic iron oxide nanoparticles into water.

then they are coated with silica exploiting various methods such as the Stöber and sol-gel processes. For instance, in the Stöber methods, a uniform layer of silica is simply formed by adding tetraethyl orthosilicate (TEOS) into a particle aqueous suspension and its thickness can be tuned from 5 nm to 200 nm by changing ratio of TEOS to water and ammonia concentration. This process was initially proposed by Stöber et al.[90] for the fabrication of monodisperse silica particles. The coating process is rather trivial and straight forward and normally one can get a uniformly sized shell of silica around the particles. Simplicity of this method enabled Ma et al.[91] to incorporate dye molecules in the second layer of silica coating after synthesizing $Fe_xO_y@SiO_2$ via the Stöber methods. The major drawback of this approach is with respect to the particle magnetic properties [91]. It is suggested that capping the particles with a thick and dense shell of silica spoils their saturation magnetization plausibly due to the formation of a magnetically dead layer at the interface. This phenomenon was observed by Deng et al. [92].

2.4.2 Cytotoxicity

Biological and toxicological behavior of magnetic NPs is one of the biggest concerns about using them in biomedicine and bioanalysis. In the last few years, understanding the pathways whereby nanoparticles as an external object react with living beings has been a great research challenge. Recently, it is attempted to understand the interaction of magnetic NPs *in vivo*, to design a potent biomarker which preserve its functionality and does its tasks in biological media. The injected nanoparticles into body first experience a highly ionic and salty biological fluid. Hence the first question which may arise is how stable the particles are against agglomeration and coagulation and whether this would be affected through interaction with all existing living objects such as proteins, cells, macrophages, etc. It sounds like an absolute necessity to explore how the interaction and agglomeration processes firstly threaten the life of the studied living being and secondly how they may influence or even change the particle functionality. Other sophisticated issues are such as: what will happen to the particles on a long term in the body, where do they go and how do they distribute in the body? Particularly in the applications where the particles are manipulated to carry drugs to a specific organ, questions regarding particle uptake and internalization by macrophages may appear. Apparently, addressing all these topics is a non-trivial task since all of them are involved with assessing biological responses. Things become even harder by knowing that the findings can not be extrapolated for the iron oxide NPs coated and functionalized with different chemistries due to a significant dependence of the particle behavior in the body on its composition, size, coating and surface chemistry.

3 Characterization methods

In the world of nanoscience, analyzing physical and chemical properties of nanomaterials is of great scientific and technological importance. At the nanoscale, this task is particularly non trivial due to the length scale one deals with and anomalous behavior of nanomaterials compared to what observed in bulk materials. The characterization issue becomes more sophisticated when it comes to nano-biomaterials which directly target living beings. In the nano-biomaterials one should tackle biological and physicological concerns such as toxicity and biocompatibility, implying that a greater attention has to be paid. For having MNPs capable of being used as magnetic markers, from the physical properties of the particle core encompassing size and shape distribution, crystal structure, phase composition, static and dynamic magnetic properties to the surface chemistry, toxicity, stability in biological fluids and their interaction with the existing living beings have to be identified. The following chapter summarizes the characterization methods which have been used in this thesis to fulfil this necessity.

3.1 Characterization of iron-oleate precursor

In order to identify chemical composition, structure, and thermal decomposition behavior of the synthesized iron-oleate, a variety of analysis methods was used including elemental analysis (EA), fourier transform infrared spectroscopy (IR), thermogravimetric analysis (TGA) and differential scanning calorimetry (DSC).

3.1.1 Elemental analysis

Elemental analysis (EA) is a well known technique in analytical chemistry for determining the composition of an unknown organic compound as well as assessing its purity. In the most common type, the EA analysis is used to measure the mass fractions of carbon (C), hydrogen (H), nitrogen (N) and heteroatoms (X) (halogens, sulfur) which is refereed to CHNX analysis. The EA analysis allows one to determine the empirical formula of an organic compound. The empirical formula is the smallest set of integer ratios of the presenting elements in the compound. In a typical EA experiment, 2-3 mg of the sample is wrapped into a tin foil and burnt at $\approx 1000^{\circ}$C under purging of an excessive oxygen pressure. The resultant mixture of gases including CO_2, H_2O and N_2 are flowed into a gas chromatographer and their mass fractions are measured.

Here, the EA (C & H) analysis was employed to determine the elemental composition of the iron-oleate precursor synthesized at different conditions. The results will be interpreted in section 5.1.

3.1.2 Fourier transform infrared spectroscopy

IR spectroscopy (Bruker Tensor 27) has been recognized as a powerful tool in characterization of organic compounds, and recently has been considered as a reliable technique to analyze the surface chemistry of nanomaterials. Generally speaking, in the IR technique, electromagnetic radiation interacts with the sample and if its frequency matches with the elementary excitations of the targeted molecule, the radiation is absorbed. The absorbed energy triggers a change in the amplitude of molecular vibration and leads to the appearance of absorption bands. To be an IR active molecule, the vibration or rotation of the molecule should cause a net change in its dipole moment. IR spectroscopy can provide structural and bonding information of the constituent molecules [93]. Here, the IR technique has been employed to check the success and degree of the substitution reactions used to synthesize iron-oleate and hydrophilic ligands for transferring iron oxide NPs into water. The exchange of oleic acid (OA) molecules with the hydrophilic ligands on the particle surface after phase transfer reaction was also examined. Moreover, different possible coordination modes of oleate groups with iron in the iron-oleate structure were investigated.

3.1.3 Thermogravimetric analysis

Thermogravimetric analysis (TGA) (Netzsche, Thermisch Analyse, TG 209, Cell) was utilized for two different purposes. Firstly, we have studied the thermal decomposition behavior of the iron-oleate precursor synthesized under

different experimental conditions to optimize the precursor synthesis procedure. TGA analysis enables one to determine the temperatures at which particles are crystallized and the growth process terminates. Accordingly, dependent on the precursor thermal properties, a solvent with a desirable boiling temperature has been chosen. This strategy enables us to synthesize particles with different core size distribution.

In a typical TGA experiment, 5-10 mg of the freshly obtained iron-oleate was loaded into an alumina vial and the weight loss was recorded from 25°C to 500°C at a heating rate of 1°C/min and 3°C/min under flow of nitrogen ($\approx$ 20 mL/min) as a protecting gas to avoid oxidizing of the oleic acid.

The second purpose of performing TGA is to assay the number of the capping ligands (OA in hydrophobic particles and poly(ethylene glycol)(PEG)-nitrodopamine in hydrophilic ones) on the particle surface. For spherical particles, this estimation can be done using Eq. 3.1 given by

$$\text{Weight loss fraction} = \frac{(\frac{\pi}{a}d_c^2)(\frac{M}{N_A})}{(\frac{\pi}{6}d_c^3\rho + (\frac{\pi}{a}d_c^2)(\frac{M}{N_A}))} \tag{3.1}$$

with d_c the mean core diameter, a the head area of a single binding molecule, M the molecular weight of the capping ligands, N_A the Avogardo constant. Having assumed that the iron oxide density ρ is 5.18 g cm^{-3}, OA and PEG molar masses M are 282 and 3900 g mol^{-1} and N_A is 6.022141$\times$10^{23} mol^{-1}, the head area of a single OA molecule and the number of PEG molecules per nm^2 of the particle surface is approximated and the results are discussed in sections 5.5.2 and 5.5.3.

For this type of assessment, 5-8 mg particles were dried under high vacuum at 40°C. Next, the dried powder was loaded into an alumina vial and heated from 25°C to 900°C under flow of a mixture of nitrogen ($\approx$ 10 mL/min) and oxygen ($\approx$ 20 mL/min).

3.2 Particle size and morphology characterization

One of the prime aims of this thesis is studying the mechanisms whereby monodisperse SPIONs are crystallized. For doing so, size and morphology distribution of the particles synthesized at different conditions have to be investigated. Transmission electron microscopy (TEM) and fluxgate magnetorelaxometry (MRX) have been employed as two complementary techniques.

3.2.1 Transmission electron microscopy

TEM is a versatile technique for analyzing particle size and morphology distribution as well as crystal structure via diffraction and imaging techniques. First, we briefly review the principles of the technique in both imaging and diffraction modes.

A typical TEM microscope consists of three types of lenses including an objective, an intermediate and a projection lens. A schematic representation of the electron path rays in imaging and diffraction modes are depicted in Fig. 3.1.

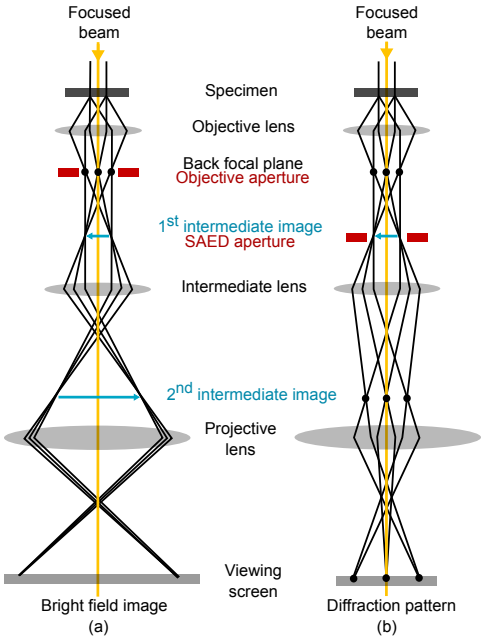

Figure 3.1: Ray paths in a transmission electron microscope in (a) imaging mode and (b) selected area diffraction mode.

In a simple description, the objective lens generates a diffraction pattern in the back focal plane (BFP) and forms an image in the 1st intermediate image plane. Therefore, both imaging and diffraction modes are present at the same time and the intermediate lens defines which one appears in the 2nd intermediate image plane which is eventually magnified by the projection lens on the viewing screen. Usually, bright field (BF) imaging is utilized for general size and morphology studies. However, switching between BF, dark Field (DF) and high resolution TEM (HRTEM) can be obtained by inserting an objective aperture in the BFP to only pick up the beams required for the formation of the desired image [94].

Here, for general size and morphology investigations, a Philips CM12 (100 kV) microscope was used. TEM samples were made by dropping a very diluted particle suspension in chloroform on carbon-coated copper grids and let it dry completely. High resolution TEM experiments were performed with a double spherical aberation corrected field emission microscope (JEOL, 200 kV) as described in section 3.3.1.

3.2.2 Fluxgate magnetorelaxometry

Magnetorelaxometry (MRX) is a relatively new technique for investigating MNP dynamics. To date, MRX experiments have been conducted using different magnetic field sensors such as superconducting quantum interference devices

(SQUIDs) [95–97] and fluxgates [98]. It has been realized that SQUID MRX has certain drawbacks such as extremely low operation temperature (liquid nitrogen or helium required) and its sensitivity to environmental magnetic disturbances. Since a decade ago, attentions drew towards fluxgate magnetic field sensor which can be operated at room temperature [99] and does not need a sophisticated instrumentation. The first version of the fluxgate MRX was built using one fluxgate sensor [100]. Soon after, the authors have shown that by using two fluxgate sensors in a differential configuration (illustrated in Fig. 3.2), a factor of two enhanced signal can be achieved [98]. This means a factor of $\sqrt{2}$ improvement in the signal-to-noise ratio (SNR). Also, in the former version with one fluxgate sensor, only particles which are close to the sensor contribute to the signal due to the $1/r^3$ dependence of the magnetic field produced by a magnetic moment upon its distance to the fluxgate sensitive core.

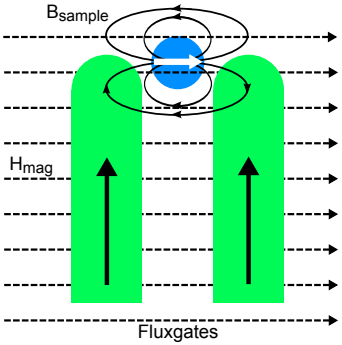

Figure 3.2: Differential configuration of two fluxgate magnetometers.

In the fluxgate MRX set up used here, a homogeneous magnetic field is generated by two Helmholtz coils being positioned perpendicularly. The sample is positioned symmetrically between two fluxgate magnetometers which are placed in the set up in a way that their sensitive axes are oriented perpendicularly to the magnetic field and hence to the sample magnetic moment (cf. Fig. 3.2). Ideally, this implies that when there is no magnetic sample, no magnetic field from the Helmholtz coil is seen by the sensors [98].

In a typical MRX experiment, first, the magnetic field is off and owing to the superparamagnetic behavior of particles, the net magnetization is zero (cf. Fig. 3.3, step 1). Afterwards, a magnetizing field with a magnitude of 2 mT is exerted for 2 seconds to align the magnetic moments in its direction (denoted as step 2). Next, the magnetizing field is switched off rapidly and the signal decay is recorded for 1.5 seconds (designated as step 3). Ultimately, the magnetic moments are distributed randomly due to thermal agitation and thus the magnetic signal drops to zero. The whole process is rather quick and depending on particle size takes from a few microseconds to a few seconds.

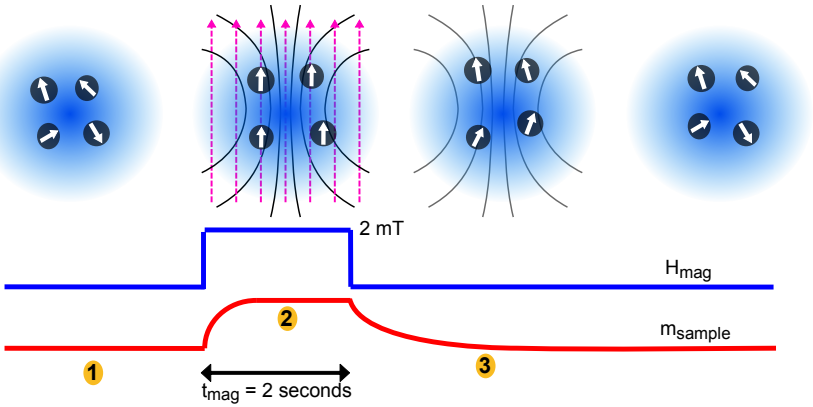

Figure 3.3: Schematic visualization of the magnetorelaxometry measurement principles.

Both relaxation mechanisms can be measured using fluxgate MRX depending on whether the particles are mobile or immobile (cf. section 1.2.4). To obtain information about the particle magnetic core, the magnetic relaxation of the immobile sample (i.e. Néel relaxation) has to be analyzed. To do this, the model describing the time dependent relaxation signal named moment superposition model (MSM) originally proposed by Chantrell et al. [101] was exploited [99]. Provided that the sample contains non-interacting spherical superparamagnetic particles showing a lognormal core size distribution $f(d_c, \mu_c, \sigma_c)$ given by

$$f(d_c, \mu_c, \sigma_c) = \frac{1}{\sqrt{2\pi}\sigma_c d_c} \exp[-\frac{(\ln d_c - \ln \mu_c)^2}{2\sigma_c^2}], \tag{3.2}$$

in which μ_c and σ_c are geometric mean and standard deviation, respectively, and d_c is the particle core diameter, the magnetorelaxation signal m_r after turning off the magnetizing field may be written as

$$\begin{aligned} m_r(t, t_{mag}, H_{mag}) = M_s \int_0^\infty f(d_c, \mu_c, \sigma_c) \cdot \frac{\pi}{6} d_c^3 L(d_c, H_{mag}) \\ \cdot\{1 - \exp[-\frac{t_{mag}}{\tau_{NH}(K, d_c, H_{mag})}]\} \\ \cdot \exp[-\frac{t}{\tau_N(K, d_c)}] dd_c, \end{aligned} \tag{3.3}$$

where t_{mag} and H_{mag} are the magnetizing time and field, M_s is the saturation magnetization and τ_{NH} and τ_N are the Néel relaxation in the presence and absence of the magnetizing field, respectively [102].

3.3 Structural and crystallographic analyses

Phase composition and crystal structure of iron oxide nanoparticles have a great influence on their magnetic properties. For instance, some oxide phases such as wüstite and hematite are antiferromagnetic, nearly showing no magnetic response. Also, the magnetization saturation and anisotropy constant depend significantly on the particle composition. Another example is the dependence of the single domain size limit (cf. section 1.2.2) on the composition [8]. Deep understanding of the structural and crystallographic features of SPIONs enables one to fabricate optimal particles for different applications.

3.3.1 High resolution electron microscopy

High resolution transmission electron microscopy (HRTEM) is a promising analysis tool for identifying the crystal structure and imaging the lattice structure of nanomaterials. The HRTEM technique allows one to investigate the phase distribution within a single particle by performing fast fourier transform (FFT) analysis. As discussed in the section 3.2.1, a HRTEM image is generated by inserting an especial objective aperture in the BFP. The sharpness of an image relies substantially on the quality of the projection lens.

Herein, a double spherical aberration corrected field emission HRTEM microscope (JEOL, 200 kV) able to magnify down to less than 1 Å was utilized. For HRTEM imaging, the sample preparation is of crucial importance. Therefore, the particles were washed several times through the solvent-antisolvent chemistry (refer to section 4.4). The resulting clean particle suspension was diluted very much and then a drop of the suspension was dried on a carbon-coated TEM copper grid. Image J software was exploited to perform FFT analyses on HRTEM images as well as determining the lattice fringes.

3.3.2 X-ray and electron diffractions

Powder X-ray diffraction (XRD) is presumably the most known and used technique for studying the structure of long-range ordered materials. In a simple definition, a XRD machine is made of two parts: a X-ray source and a detector. The X-ray source is a beam of energetic electrons (typically ≈ 35 keV) shining to a solid target (e.g. Copper) and resulting in the generation of X-ray photons. The XRD technique is based on the Rayleigh (elastic) scattering of photons and hence a collimated and monochromatic X-ray beam is required. In crystalline materials, the incident X-ray beam is reflected by a set of lattice planes if the Bragg's conditions are fulfilled. Bragg's diffraction law, initially proposed by William Lawrence Bragg and William Henry Bragg, says that the diffraction solely happens from those planes which make an angle equal to a Bragg angle θ_B with the incident beam and given by

$$n\lambda = 2d_{(hkl)}sin(\theta_B), \tag{3.4}$$

with λ is the electron wavelength, $d_{(hkl)}$ is the interplanar lattice spacing and n is an integer number describing the diffraction order [103]. In other words,

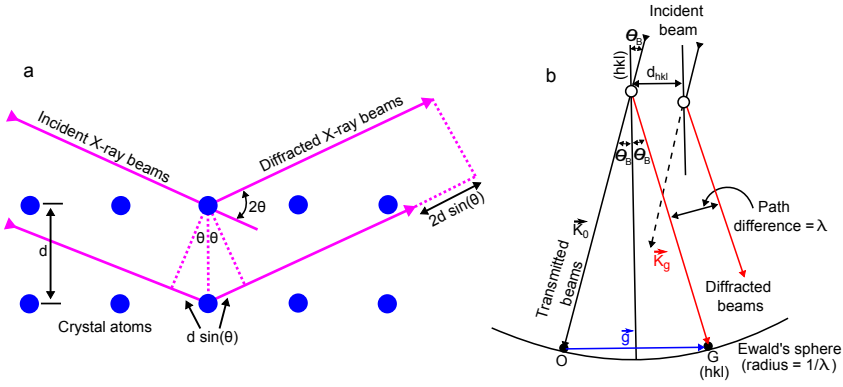

Figure 3.4: (a) Schematic illustration of Bragg's law for X-ray diffraction from crystal planes with lattice spacing d and (b) representation of the diffraction conditions in the reciprocal space.

Bragg's law states that the path difference between two beams reflected by two parallel lattice planes is an integer multiplication of λ. A schematic depiction of the diffraction phenomena from crystal atoms is shown in Fig. 3.4(a). Here, the XRD measurements were carried out on the dried particles using PANalytical X'Pert PRO machine using Cu $K_{\alpha 1}$ X-ray source ($\lambda = 1.5406$ Å) scanning 2θ from 5° to 90° with the step size of 0.033°.

By switching the TEM operation mode to the diffraction one (cf. section 3.2.1), selected area electron diffraction (SAED) of the sample can be obtained. The SAED is a potent tool for characterizing the crystal structure of crystalline materials. The diffraction phenomena in both XRD and TEM are based on identical physical principles.

In TEM, the electron wavelengths are in the range of ≈ 0.06Å (i.e. 200 keV), far below a typical interplanar lattice spacing ≈ 3Å, which results in small Bragg angles $\approx 10^{-3}$ rad. This implies that Eq. 3.4 can be simplified using the small angle approximation and be rewritten as

$$n\lambda = 2d_{(hkl)}\theta_B. \tag{3.5}$$

For geometrical interpretation of the diffraction conditions, the concept of reciprocal lattice together with Ewald's sphere are used as visualized in Fig. 3.4(b). A diffraction pattern is the planar projection of the reciprocal lattice on the TEM viewing screen. In other words, a diffraction pattern is a two dimensional reciprocal lattice. A direct fcc lattice is defined by three basis vectors $\vec{a}_1$, $\vec{a}_2$ and $\vec{a}_3$ given by

$$\vec{a}_1 = \frac{a_1}{2}(\vec{i} + \vec{k}), \quad \vec{a}_2 = \frac{a_2}{2}(\vec{i} + \vec{j}), \quad \vec{a}_3 = \frac{a_3}{2}(\vec{j} + \vec{k}),$$

$$a_1 = a_2 = a_3 \quad \text{and} \quad \alpha = \beta = \gamma \tag{3.6}$$

with $\overrightarrow{i}$, $\overrightarrow{j}$ and $\overrightarrow{k}$ unit vectors of a Cartesian coordinate system. A reciprocal lattice of a fcc lattice, likewise to its direct lattice, is also specified with three basis vectors $\overrightarrow{b}_1$, $\overrightarrow{b}_2$ and $\overrightarrow{b}_3$ in a way that the following relations fulfil [104].

$$\overrightarrow{a}_i \cdot \overrightarrow{b}_j = \begin{cases} 1 & \text{if } i = j, \\ 0 & \text{if } i \neq j. \end{cases} \tag{3.7}$$

The reciprocal vectors can be expressed by

$$\overrightarrow{b}_1 = 2\pi \frac{\overrightarrow{a}_2 \times \overrightarrow{a}_3}{\overrightarrow{a}_1(\overrightarrow{a}_2 \times \overrightarrow{a}_3)}, \overrightarrow{b}_2 = 2\pi \frac{\overrightarrow{a}_3 \times \overrightarrow{a}_1}{\overrightarrow{a}_1(\overrightarrow{a}_2 \times \overrightarrow{a}_3)}, \overrightarrow{b}_3 = 2\pi \frac{\overrightarrow{a}_1 \times \overrightarrow{a}_2}{\overrightarrow{a}_1(\overrightarrow{a}_2 \times \overrightarrow{a}_3)} \tag{3.8}$$

In fact, these vectors correspond to the basis vectors of a direct body centred cubic (bcc) lattice. It is understood that the reciprocal lattice of a fcc lattice is in fact a bcc one. The lengths of the basis reciprocal vectors are proportional to the inverse lengths of the direct basis vectors and may be expressed by

$$|\overrightarrow{b}_1| \propto \frac{1}{|\overrightarrow{a}_1|}, \quad |\overrightarrow{b}_2| \propto \frac{1}{|\overrightarrow{a}_2|}, \quad |\overrightarrow{b}_3| \propto \frac{1}{|\overrightarrow{a}_3|}. \tag{3.9}$$

Accordingly, a typical node in the reciprocal space can be defined by

$$B_H = h\overrightarrow{b}_1 + k\overrightarrow{b}_2 + l\overrightarrow{b}_3, \tag{3.10}$$

with (hkl) "Miller indices" of crystalline planes.

The diffraction in the reciprocal space can be visualized exploiting the Ewald's sphere as shown in Fig. 3.4(b). The Ewald's sphere is a reflecting sphere with the radius of $1/\lambda$. In figure, $\overrightarrow{K_0}$ is the incident beam vector (a so-called direct or transmitted beam), $\overrightarrow{K_g}$ is the scattered beam vector and $\overrightarrow{g}$ is a vector drawn from the origin of the reciprocal space O to the diffraction spot G, oriented perpendicularly to the diffracting plane and is called the diffraction vector. Using the Ewald's sphere, diffraction occurs when the following vectorized equation fulfils [103].

$$\overrightarrow{k_g} = \overrightarrow{k_0} + \overrightarrow{g}. \tag{3.11}$$

Each reciprocal lattice point that the sphere touches will give a diffracted beam. An electron diffraction pattern is thus a projection of a plane section through the reciprocal lattice.

3.3.3 Electron energy loss spectroscopy

To gain information about the electronic structure of iron oxide NPs, electron energy loss spectroscopy (EELS) was employed. In EELS, an incident electron beam interacts with atoms of the crystalline material and scatters inelastically,

and thereby its kinetic energy and momentum change [105, 106]. The inelastic scattering occurs due to the interaction of the incident electron beam with the surrounding electrons. This means that the electron shells can be identified by this technique. In a typical EELS experiment as shown in Fig. 3.5, the incident electron (100-300 keV) is guided through the spectrometer by tilting the TEM screen to a vertical position, passes through a magnetic prism located below the TEM imaging screen and disperses in the dispersion plane depending on its kinetic energy. In modern TEM microscopes, the EELS spectrometer is integrated into the TEM imaging column to preserve the column vertical and avoid image instability causing by tilting the TEM screen in the older versions.

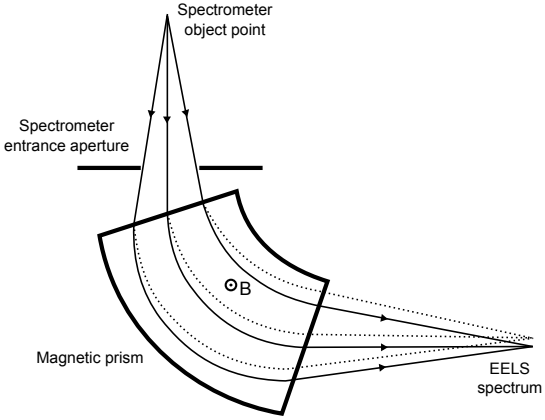

Figure 3.5: Schematic view of an EELS spectrometer in a direction perpendicular to the magnetic field.

EELS experiments were carried out using the HRTEM microscope equipped with an EELS spectrometer. The spectra usually sit on a rich background which has to be removed for further quantitative studies. For doing that, a power law function, $f(E) = AE^{-\lambda}$, is fitted to the onset of each edge and the best fit is subtracted from the spectrum [107]. This step can usually be done using TEM operating software.

3.4 Hydrodynamic properties

In any application where the particles have to be used in suspension, the issues of particle clustering and sedimentation become major concerns. This is extraordinarily crucial when it comes to biomedical applications owing to additional interactions which may occur between particles and the living beings such as cells, proteins, etc. Needless to mention that the interaction situation is even stronger in magnetic NPs due to strong attractive magnetic dipole-dipole interactions. Therefore, it is of great importance to know the hydrodynamic properties of magnetic NPs prior to conducting any biomedical experiments.

3.4.1 Photon cross-correlation spectroscopy

Dynamic light scattering (DLS) and photon correlation spectroscopy are standard tools for determining the hydrodynamic size of nano and micro-sized objects in suspension. In a simple definition, a DLS device is made of three main components: a laser source, a cell and a photomultiplier detector and basically it traces the Brownian motion of particulate objects in a dispersion medium. Generally, the sample is illuminated with an incident laser beam (a light) which is either absorbed or scattered by the particles. The properties of the scattered light are defined by a quantity called the scattering vector $\overrightarrow{q}$ described as the difference between the incident and scattered light and its magnitude is given by

$$q = \frac{4\pi R_{index}}{\lambda_0} \sin(\frac{\theta}{2}), \tag{3.12}$$

with R_{index} the refractive index of the dispersion medium, θ the scattering angle and λ_0 the incident light wavelength.

From this equation, it is realized that q^{-1} has the dimension of length and commonly its quantity varies between 10 and 1000 nm.

The most common method to analyze the registered events (i.e. the scattered light) at the detector is the use of the autocorrelation function $G_2(\tau)$ of the intensity of the scattered light $I(t)$ which may be given by

$$G_2(\tau) =< I(t) \cdot (I)(t+\tau) > . \tag{3.13}$$

The $G_2(\tau)$ is made of the scattered light intensity detected at a random observation time t times the intensity registered at a time delay τ. This means that for a short delay time, the scattered intensities (particle positions) are highly correlated and thus $G_2(\tau)$ is large. On the contrary, for a long delay time, the intensities are not correlated, showing that $G_2(\tau)$ is almost zero. The characteristic decay time τ^* is inversely proportional to the translational diffusion coefficient D in $\mathrm{m}^2\ \mathrm{s}^{-1}$ and the scattering vector by

$$\tau^* = \frac{1}{2Dq^2}, \text{ with } D = \frac{k_B T}{3\pi\eta d_h}, \tag{3.14}$$

in which η is the dispersion medium viscosity in kg $\mathrm{m}^{-1}\mathrm{s}^{-1}$.

If there is a large enough number of particles in the measuring volume, the intensity autocorrelation function can be expressed by

$$G_2(\tau) = Bg_1^2(\tau) + A, \tag{3.15}$$

with A and B+A the baseline and intercept of the correlation function, respectively. For non-interacting monodisperse particles the so-called field correlation function is given by

$$g_1(\tau) = \exp(-\Gamma\tau). \tag{3.16}$$

The B/A ratio is known as the instrumental factor, indicating the number of constructive interference events counted on the detector. The largest ratio is gained when all the registered events on the detector have the identical $\overrightarrow{q}$, meaning the same scattering angle θ. The autocorrelation function shows an exponential decay versus the delay time with the decay rate Γ related to the translational diffusion coefficient by [108]

$$\Gamma = Dq^2. \tag{3.17}$$

Considering Eq. 3.14 and 3.17, it can be seen that the decay rate Γ is inversely proportional to d_h. For polydisperse samples, there is a decay rate Γ_i for each corresponding size d_h^i. Therefore, $g_1(\tau)$ (Eq. 3.16) becomes a sum of exponential components and given by

$$g_1(\tau) = \sum_{i=1}^{n} c_i \exp(-\Gamma_i \tau), \tag{3.18}$$

where c_i presents a weighing factor for the particles with the diffusion coefficient of D_i. After calculating the field correlation function from the experimentally measured $G_2(\tau)$, the set of decay rates $(\Gamma_i, i = 1, \cdots, n)$ and weighing factors $(c_i, i = 1, \cdots, n)$ can be obtained by applying an inversion solution to Eq. 3.18. To extract the unnormalized form of the field correlation function, $G_1(\tau) = B^{0.5} g_1(\tau)$, some information about the baseline A is required. After evaluating the baseline, $G_1(\tau)$ can be expressed by [108]

$$G_1(\tau) = \sqrt{G_2(\tau) - A}. \tag{3.19}$$

To date, two different types of methods have been applied for the inversion solutions. The first type is the one which does not requires any prior knowledge. The most commonly used one in this category is the cumulants analysis, valid for monodisperse particles. In this case, since there is just one decay rate, $\ln G_1(\tau)$ decays linearly versus delay time with the slope Γ inversely proportional to the particle size via Eq. 3.14 and 3.17.

By having a polydisperse sample, $\ln G_1(\tau)$ deviates from its linear shape particularly at large τ. This deviation is used to determine the polydispersity index. The decay rate and the polydispersity index can be calculated by fitting the correlation function plotted in semi-log scale with a 3^{rd} order polynomial function as given by

$$\ln(G_1(\tau)) = a + b\tau + c\tau^2, \tag{3.20}$$

where b is the z-average diffusion coefficient and $2c/b^2$ is the polydispersity index. The major drawback of the cumulants analysis is that it is only valid for mono-modal particles [108].

One of the well known methods from the second type of methods used for the inversion solutions is a non-negative least square (NNLS) algorithm. In fact, the NNLS is a least squares method whereby only positive contributions to the

intensity weighted distributions are taken into account. The idea of applying NNLS instead of the least squares originates from a physically unreasonable size distributions obtained using the latter one. However, to do the NNLS analysis, some prior knowledge such as the baseline A, the weighing factor c_i and the decay range (i.e. the particle size range) should be known. This approach enables one to resolve the size modality existing in polydisperse samples.

One of the main concerns about the light scattering measurement is that to what extent single or multiple scattering events are registered at the detector. The single scattering is a condition in which the incident light is scattered only by one particle before counting at the detector. The multiple scattering is a phenomenon where the incident laser is scattered multiple times by different particles prior to being registered at the detector, resulting in a destructive interference of the scattered lights and a reduced B/A quantity. This decreases the quality of the correlation function and eventually results in less accurate calculations. In the recently developed photon cross-correlation spectroscopy (PCCS) machines (e.g. Nanophox, Sympatec GmbH), the cross-correlation measurement mode is used in which instead of just using one laser source, two laser beams are interacting with the sample. This technique has been shown to be a reliable approach for eliminating the destructive multiple scattering events.

The final resulting distribution function can be presented in number, intensity or volume weighted distributions. Note that the original signal is intensity weighted. The number distribution is the real distribution of the sample without any dependence on the particle size. The intensity weighted distribution scales with r^6 and thus large clusters dominate the measurements. The volume weighted distribution scales with r^3 and thus is less sensitive to the presence of big clusters. Hence it is the most common way of presentation. In this thesis, all the analyses have been performed using the NNLS algorithm.

In order to probe the particle stability against temperature, a series of temperature dependent PCCS measurements have been carried out on aqueous samples. To do this, a diluted aqueous suspension of the particle was heated up from 25°C to 40°C in 5°C steps inside the PCCS machine with 10 min stabilization time prior to the respective PCCS experiment.

3.5 Magnetic properties

3.5.1 Mössbauer spectroscopy

Mössbauer spectroscopy is based on the Mössbauer effect found by Rudolf Mössbauer for which the Nobel prize in physics was awarded to him in 1961 [109]. Principally, when a nucleus emits a γ ray, its energy E_γ is smaller than the nuclear transition energy ΔE due to the recoiling of the nucleus with the energy of E_R ($E_\gamma = \Delta E - E_R$). Owing to an identical recoil process happening in the absorber, the emitted γ ray would be resonantly absorbed only if its energy was greater than the nuclear transition energy ($E_\gamma = \Delta E + E_R$). The recoiling phenomenon results in two separated emission and absorption energy distributions as schematically depicted in Fig. 3.6.

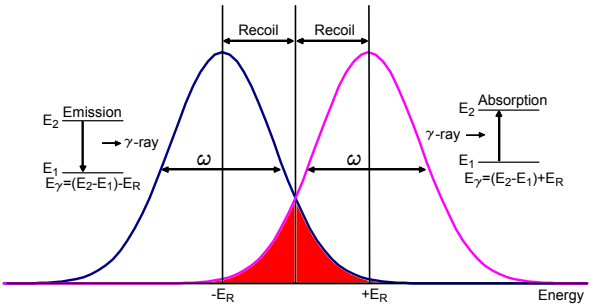

Figure 3.6: Schematic representation of the recoiling phenomena during emission and absorption of γ ray.

In contrast to the described emission and absorption phenomena involving recoil, the Mössbauer effect is a recoil-free nuclear resonance absorption of γ radiation. Mössbauer discovered that when the γ ray energy is low enough to excite any phonons, the whole mass of the solid overtake recoil, thus recoil vanishes. This process is called a recoil-free event whereby the energy of the emitted γ ray is equal to the nuclear transition energy ($E_\gamma = \Delta E$) and the emission and absorption energy profiles (shown in Fig. 3.6) overlap. Having the emitted and absorbed γ ray with an identical energy results in resonance and the appearance of a spectrum with a single absorption line. The resulting spectrum can tell a lot about the interaction of an atom's nucleus with its environment and the oxidation state of oxide materials. For studying the particle phase composition Mössbauer absorption experiments were performed using the 14.4 keV gamma ray transition of ^{57}Fe, that has an abundance of about 2% in natural iron. We used a conventional Mössbauer spectrometer with ^{57}CoRh as gamma ray source kept at room temperature. The absorber temperature can be varied from 4 K to 300 K using a LakeShore 336 temperature controller. The experiments were performed on $\approx$ 20-30 mg of freshly synthesized and dried nanoparticles. The samples were stored in an air-free atmosphere until measured.

3.5.2 M-H hysteresis loops

Static magnetization measurements were employed to probe particle magnetization and measure their saturation magnetization. The measurements have been performed using a Magnetic Property Measurement System (MPMS-XL, Quantum Design) magnetometer at room temperature. In a typical experiment, the sample magnetic moment is measured as a function of an external magnetic field increasing stepwise up to 5 T. In fact, at each field, the particle magnetic moments are let to reach the saturation magnetization possible to be achieved at that specific field. Owing to this feature, these measurements are categorized as the static ones and thus the dynamic magnetic behaviors play no significant role. The magnetization curve can be fitted with the Langevin function given in Eq. 1.16, allowing us to estimate sample magnetic moment distribution.

3.5.3 Field and zero field cooled hysteresis loops

Zero field cooled (ZFC) measurements are considered to be a powerful analysis method for determining the presence of different phases in iron oxide NPs due to a significant difference between Verwey transition temperature T_V characteristic of magnetite and the Néel temperature T_N of wüstite phase [110, 111]. To perform a ZFC analysis, the immobile sample is firstly cooled to 5 K in zero magnetic field and then the change in the magnetic moment as a function of temperature increasing stepwise to room temperature is recorded in a magnetic field of 1 mT. The immobile samples were prepared by solidification of 80 μL of the particle suspensions in chloroform with $\approx$ 80 mg gypsum.

Moreover, the exchange bias energy, triggered from the spin coupling at the interface of FIM and AFM phases, is seen in particles consisting of both phases [111]. Field cooled (FC) hysteresis loops were recorded to verify the hypothesis of a simultaneous presence of a mixture of both FIM and AFM phases in particles. The FC experiments have been carried out on the identical immobile samples likewise to ZFC via cooling them from room temperature to 5 K in a magnetizing field of 5 T prior to recording the hysteresis loops. The ZFC hysteresis loops were acquired by setting a nominal field of -0.03 mT to compensate the residual magnetic field of the system. It should be mentioned that in all the hysteresis measurements the virgin curve starts to be recorded at the magnetic remanence. Furthermore, any diamagnetic and paramagnetic effects of the measuring capsule (made of polycarbonate) and gypsum were subtracted from the original results through performing the same measurements on a pure gypsum sample made in the exactly same fashion.

3.5.4 AC susceptibility

AC susceptibility (ACS) has been used to study the dynamic magnetic properties of SPIONs [112]. In an ACS experiment, an alternating magnetic field with a small driving field (i.e. 95 μT in the used setup) and frequency ω is applied to MNPs and their response is picked up by the detection coils. This dynamic response, depending on the particle relaxation mechanisms and time constants, is a complex magnetic susceptibility $\chi(\omega)$, consisting of both real $\chi'(\omega)$ and imaginary $\chi''(\omega)$ terms and may be given by

$$\chi(\omega) = \chi'(\omega) + i\chi''(\omega). \tag{3.21}$$

The real and imaginary part can be described using Debye's theory and can be expressed by

$$\chi'(\omega) = \frac{\chi_0}{1 + (\omega\tau_{eff})^2},$$

$$\chi''(\omega) = \frac{\chi_0\omega\tau_{eff}}{1 + (\omega\tau_{eff})^2}, \tag{3.22}$$

with χ_0 the DC magnetic susceptibility and τ_{eff} the effective relaxation time constant (cf. Eq. 1.19).

Generally, increasing the frequency results in a monotonic dropping of $\chi'(\omega)$ and the appearance of a maximum peak in $\chi''(\omega)$ at $\omega_m\tau = 1$ [112]. Generally, one would expect to observe two peaks in a typical $\chi''(\omega)$ plot. The one appearing at low frequency range ($\approx$ 0.1-20 kHz) is related to Brownian relaxation and the second one emerging at high frequency range ($\approx$ 1-10 MHz) is attributed to Néel relaxation process. In the thesis, an ACS set up with a frequency range from 1 kHz to 1 MHz was used and due to small particle core size and anisotropy constant, only the Brownian imaginary peak has been observed [113]. In the simplest sense, the imaginary peak position ω_m can be used to calculate the particle relaxation time and extract the particle hydrodynamic size d_h using the Brownian relaxation equation (cf. Eq. 1.17). This is however a naive approach since a real magnetic ferrofluid always shows a size distribution. Chung et al. [114] proposed a model for the analysis of $\chi''(\omega)$ by taking a lognormal size distribution function (cf. Eq. 3.2) into account which can be expressed by

$$\chi''(\omega) = \chi_0^* \int_0^\infty f(d_h) \int_0^\infty \frac{d_c^6 \cdot f(d_c) \cdot \omega\tau_{eff}}{1 + (\omega\tau_{eff})^2} dd_c dd_h,$$
$$\text{with } \chi_0^* = \frac{\mu_0 n M_s^2}{3k_B T} (\frac{\pi}{6})^2, \tag{3.23}$$

in which $f(d_h)$ is the hydrodynamic size distribution.

We have used the model to extract the hydrodynamic distribution parameters d_h and σ_h by assuming typical magnetite bulk values for M_s = 480 KA m^{-1} and K = 7 KJ m^{-3} and lognormal distributions. The ACS measurements have been performed on 150 μL particle suspensions in chloroform or water.

3.5.5 Rotating magnetic field measurement

In the last few years, it has been realized that by analyzing the particle response to dynamic magnetic fields (e.g. alternating and rotating) and particularly its changes through binding to biomolecules one can build a platform for homogeneous magnetic bioassays. Since the primary aim of this study is to present the capability of iron oxide nanoparticles as a tracer for magnetic bioassays, it is of crucial importance to evaluate their response to dynamic magnetic fields. To do so, a fluxgate-based rotating magnetic field (RMF) measurement system was used [20]. The top view of the RMF setup is shown in Fig. 3.7(a). The RMF setup is made of two main components: 2-axis Helmholtz coils and fluxgate sensors. The fluxgate arrangement with respect to the magnetic field is likewise to the fluxgate MRX setup discussed in section 3.2.2. In a typical experiment, 150 μL particle suspension is positioned in its designated place labeled in Fig. 3.7(a) and then a rotating magnetic field of 1 or 5 mT with a frequency up to 5 kHz is exerted. Afterwards, the phase lag φ between the rotating field vector H and the particle magnetic moment m is calculated as schematically illustrated in Fig. 3.7(b). The measured phase lag can be used to analyze the change in the particle hydrodynamic size after being conjugated to biomolecules. Detailed information about the setup electronics, data acquisition and processing can be found in [20].

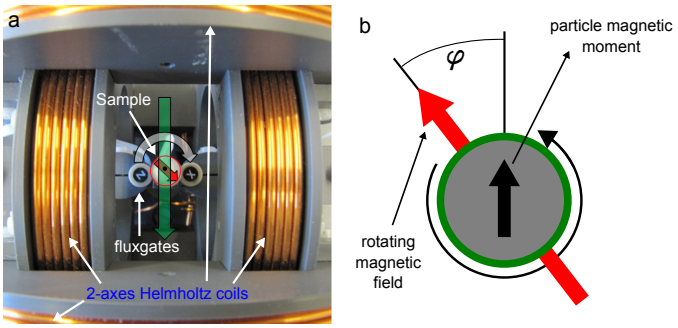

Figure 3.7: (a) Top view of the fluxgate-based rotating magnetic field setup and (b) schematic illustration of the induced phase lag φ between the rotating field vector H and the particle magnetic moment m.

The fluxgate-based RMF setup was also used to measure the flux density B of particle suspensions denoted by $B-H$ measurements in the following text. Since these measurements are fast and easy to handle, they can be considered as preliminary quasi static magnetization measurements, providing a quick estimation of the particle magnetic properties.

3.5.6 Nuclear magnetic resonance spectroscopy

Nuclear magnetic resonance (NMR) spectroscopy is widely recognized as a powerful analysis tool for determination of the chemical structure and purity of an unknown organic compound. From a theoretical point of view, when a static magnetic field B_0 is applied to a nucleus with angular momentum $\overrightarrow{I}$, it will precess around the direction of field (z-direction). The z-component of $\overrightarrow{I}$ being I_Z is given by

$$I_Z = m\hbar. \tag{3.24}$$

The magnetic moment of the nucleus is related to $\overrightarrow{I}$ by

$$\overrightarrow{\mu} = g_N \mu_N \overrightarrow{I}. \tag{3.25}$$

In Eq. 3.24, m is the magnetic quantum number which can take values from $m = I, I+1 \cdots, -I$ in which I is the angular momentum quantum number. It can be discerned that m can get $2I+1$ different values, implying that an equal number of orientations are allowed to be taken by $\overrightarrow{I}$ and $\overrightarrow{\mu}$. This feature of the nuclei in the magnetic field is named directional quantization. For proton NMR (^{1}H NMR), m has two values $\pm 1/2$, implying that there are two energy levels. The angular momentum precession frequency (Larmor frequency) ν_L is given by

$$\nu_L = |\frac{\gamma}{2\pi}|B_0, \tag{3.26}$$

with γ the gyromagnetic ratio.

In a proton NMR experiment, the nuclei are exposed to a static magnetic field, causing energy level splitting. A radio frequency (RF) field, applied perpendicular to the static magnetic field, will induce absorption and emission transitions between two discrete energy levels only if its frequency ν coincides with Larmor frequency ν_L [115]. From the quantum mechanics point of view, only transitions in which $\Delta m = \pm 1$, single quantum transitions, are allowed.

^{1}H NMR spectra were acquired with a Bruker Avance 400 MHz spectrometer at room temperature(RT) ($\approx$ 5 mg sample in D_2O or $CDCl_3$). Chemical shifts are given in ppm with respect to the residual solvent signals.

3.6 Cytotoxicity and uptake assessments

3.6.1 Cytokine determination

The levels of interleukin (IL)-6 and interleukin (IL)-10 were determined by specific ELISA using matched antibody pairs and recombinant cytokines as the standards. Ninety six-well micro titer plates were coated with the corresponding purified anti-murine capture monoclonal anti-IL-6 or -IL-10 antibody (Pharmingen, San Jose, California, USA) at 2 μg mL^{-1} in sodium bicarbonate buffer overnight at 4°C. The wells were washed and then blocked with 3% bovine serum albumin-PBS before the cell culture supernatant samples and the appropriate standard were added to each well. Biotinylated rat monoclonal anti-IL-6 or -IL-10 antibody (Pharmingen) at 2 μg mL^{-1} was added as the second antibody. Detection was performed with streptavidin-peroxidase and the plates were developed using $3, 3', 5, 5'$-Tetramethylbenzidin (TMB).

3.6.2 Lactate dehydrogenase assay

The Lactate dehydrogenase (LDH) enzyme level was measured in the supernatant of S. pyogenes-infected cells using the CytoTox 96 (Promega, USA) according to the manufacturer's instructions. Briefly, 50 μL supernatant of the treated macrophages was transferred into a 96-well enzymatic assay plate. Subsequently, 50 μL reconstituted substrate mix was added to each well and then the plate was incubated for 30 min at RT. Absorbance was measured at 490 nm. The cytotoxicity percentage can be calculated by

$$\text{dead cells (\%)} = \frac{\text{sample LDH release} - \text{spontaneous LDH release}}{\text{maximum LDH release} - \text{spontaneous LDH release}} \times 100. \tag{3.27}$$

The spontaneous release is the amount of LDH released from the cytoplasm of uninfected macrophages and the maximum release is the amount released by total lysis of uninfected cells after treatment with 0.1% Triton X-100.

3.6.3 Particle cellular uptake investigations

The particle cellular uptake by macrophages was explored by a TEM microscope equipped with a Libra 120 plus energy-filter TEM (Zeiss, Germany) with a column-integrated Omega energy-filter. The samples were prepared according to the procedure established by Roming et al. [116]. Possible deviations from the procedure caused by OsO_4 was excluded. The wide range parallel EELS (WR-PEELS) was set from -20 eV to 1018 eV with an energy resolution of 1.3 eV. Electron spectroscopic imaging (ESI) was utilized to acquire Fe-elemental maps. The ESI analysis was carried out based on the three-window method with the energy-slit set to 10 eV and the width to 711 eV, 690 eV (W1) and 660 eV (W2). The recorded images and analytical data were processed with iTEM-software (OSIS, Münster, Germany) and CorelDraw-Suite.

4 Particle synthesis, phase transfer and functionalization procedures

It is well known that the robustness and reproducibility of the colloidal synthesis of magnetic NPs is the biggest obstacle in scaling up the particle production. This is due to the complexity and multidimensional space of the influential synthesis parameters. Therefore, the optimization of the colloidal synthesis method and control over the process are absolute necessities. These goals can solely be achieved by approaching the problem systematically. Design of experiment (DOE) methodology is a powerful tool for planning and evaluating experiments. Applying DOE enables one to shrink the number of experiment runs, avoid wasting materials and time on carrying out a dozen of experiments and also at the same time lose no crucial information about the investigated system.

4.1 Air-free techniques

Synthesis of iron precursor, iron oxide NPs and hydrophilic ligands need to be performed under inert atmosphere in order to avoid undesirable oxidation reactions. Generally, there are two main techniques for handling air sensitive compounds and reactions. The newest method is the use of a glovebox being easily operated and also offers space to store air sensitive materials. However, the cost of the glovebox and the unhandiness of wearing its big gloves are considered as its major drawbacks. The other technique is the Schlenk line named after its inventor Wilhelm Schlenk [117]. A typical Schlenk line consists of an inert gas supply and a vacuum pump unit which are connected to a three ways distributor. This configuration allows one to frequently and quickly switch between gas purging and evacuation until an air-free atmosphere is obtained. Also, this technique enables one to load liquids and solids into a reaction vessel against the flow of an inert gas. Furthermore, it can easily be used for degassing and drying of a reaction mixture. These two features are required in the synthesis methodology used in this study. Therefore, an argon-based Schlenk line was set up and its overall view is shown in Fig. 4.1. The setup was also used for vacuum filtrations.

Figure 4.1: Image of the argon Schlenk line used for handling air sensitive compounds and reactions.

4.2 Chemicals

$FeCl_3.6H_2O$ (98%), 1-octadecene (ODE, 90%), tetracosane (TC, 99%), docosane (DC, 90%), hexane (95%), ethanol (99.8%), chloroform (99.9%), dopamine hydrochloride, sodium nitrite (97%), sulfuric acid (98%), N-methylmorpholine,

celite (503), deuterium oxide (D_2O, 99.9 atom % D), N, N'-Disuccinimidyl carbonate, ethanolamine, N, N-Dimethylformamide (DMF) and Phosphate Buffered Saline (PBS, 0.01 M, pH=7.4 & pH=7.2, 150 mM NaCl and 150 mM $NaSO_4$) were purchased from Sigma-Aldrich. Oleic acid (99%) and sodium oleate (97%) were purchased from TCI. Triethylamine (99.5%), hydrochloric acid (25%) and $CDCl_3$ were purchased from Carl Roth GmbH. Hydroxyl-terminated poly(ethylene glycol) NHS ester (HO-PEG-NHS, M_w 3500 Da) was purchased from Jenkem Technology. Herceptin antibody was supplied by Max-Planck-Institute for Experimental Medicine, Göttingen, Germany. Recombinant human HER2 protein was purchased from eBioscience. All the chemicals were utilized "as received" and without further purification.

4.3 Synthesis of iron-oleate

In a typical synthesis of Fe-oleate (denoted by Fe-OLA), initially 76 mmol of sodium oleate was poured into a round bottom flask connected to a Schlenk line and degassed three times using evacuation-filling with argon. Next, 24 mmol of $FeCl_3.6H_2O$, dissolved in a mixture of 36 mL distilled water, 48 mL of ethanol, and 84 mL of hexane, were loaded into the flask using the Schlenk line technique. The mixture was heated to reflux and kept for 4 h under flow of argon. After cooling the mixture down to room temperature, the resultant dark reddish top layer was washed intensively three times with 20 mL distilled water in a separatory funnel and next hexane was evaporated off using a rotary evaporator. The resultant reddish waxy product was dried in a vacuum oven at 70°C for 24 h [118].

4.4 Particle synthesis: design of experiment

The SPIONs synthesis experiments were planned and analyzed by exploiting factorial DOE methodology. The chosen factors and levels are summarized in Table 4.1. The amount of solvent (317°C (pure ODE), 327°C (3:1 w/w, ODE:TC), 337°C (2:1 w/w, ODE:TC)) and the molar ratio of oleic acid to Fe-OLA were kept constant to 10 mL and 3, respectively, in all experiments. The sample synthesis conditions are listed in Table 4.1.

Table 4.1: Low, medium and high levels chosen for design of experiments

Factor	Levels		
	-1	0	+1
Fe-OLA concentration (c) (mmol)	1.5	1.75	2
Reaction time (t) (min)	30	45	60
Reaction temperature (T) (°C)	317	327	337
Heating rate (r) (°C/min)	1	2	3

In a typical synthesis procedure, Fe-OLA, oleic acid and the solvent were loaded into a three-neck round bottom flask attached to a Schlenk line. The mixture was degassed at 100°C using the Schlenk techniques to remove any remaining traces of impurities and water and was filled with argon in the last stage. Subsequently, the mixture was heated to the desired temperature at the specific heating rate (using a PID temperature controller) and kept for the designated time under flow of argon (cf. Table 4.1). The resulting suspension was cooled down to 60°C and then the particles were washed by adding a 3:1 acetone/hexane mixture and separated by centrifuging. This process was repeated twice to eliminate impurities. The obtained particles are readily dispersible in chloroform [118]. From now on, the oleic acid coated NPs are denoted by NP-OA.

4.5 Extension of design of experiment

To furthermore explore the effect of the reaction temperature, we have planned a set of synthesis experiments in which the temperature increases up to 357°C while the other parameters were set to their highest selected values (cf. Table 4.1). Additionally, to study how particle size and morphology evolve with growth time, we have traced a single synthesis experiment by taking aliquots at certain intervals. The results of these experiments are presented and discussed in section 5.3.

4.6 Phase transfer

The NP-OA particles are readily dispersed in non-polar solvents such as chloroform and toluene. However, for biomedical applications, an aqueous colloidal suspension of particles is required. For this purpose, oleic acid molecules covered the particle surface should be replaced or/and encapsulate with hydrophilic counterparts. Recently, Amsted et al. showed a strong binding of nitrocatechols (e.g. nitrodopamine and nitro-DOPA) as a anchor group to 5 nm iron oxide NPs [74]. Interestingly, the binding capability of the mentioned anchors to the particles with bigger core sizes (22-24 nm) which principally show a significantly stronger magnetic interaction has not yet been investigated. On the other hand, not much information regarding the biocompatibility and toxicity of these compounds is available. Hence in this study, nitrodopamine was chosen as an anchoring group and poly(ethylene glycol) (PEG) was picked up as a spacer to provide hydrophilicity and stability and also offer active sites for further functionalization. PEG is one of the most promising candidates for stabilization of magnetic nanoparticles due to its help in facilitating of blood circulating and its biocompatibility. Besides, PEG is able to reduce non-specific particle-cell interaction (e.g. reduction of non-specific uptake by macrophages) [78]. To synthesize appropriate hydrophilic ligands, the hydroxyl activated PEG moieties and nitrodopamine were conjugated via a mild reaction which is described in the next sections.

4.6.1 Synthesis of nitrodopamine

Nitrodopamine was synthesized using the recipe reported by Malisova et al. [119]. Typically, dopamine hydrochloride (1.94 g, 10 mmol) and sodium nitrite (1.54 g, 22 mmol) were dissolved in 25 mL distilled water and cooled down to 0°C in a salt-ice bath. Subsequently, 10 mL sulfuric acid (17.4 M) was added dropwise to the mixture and eventually a mustard colored precipitate was formed. The resultant mustard colored slurry was stirred at room temperature overnight, and then the precipitate was filtered and rinsed thoroughly with distilled water until no trace of acid was detected. Afterwards, it was rinsed again several times with methanol. The product was dried at 40°C in high vacuum for two days and then stored in a vacuum desiccator (1,483 g, yield=63%). The chemical shifts based on ^{1}H NMR (400 MHz, D_2O, δ) analysis are: 7.73 (s, 1H, arom. H-d), 6.90 (s, 1H, arom. H-c), 3.32 (t, 2H, CH_2), 3.23 (t, 2H, CH_2). The NMR spectrum is shown in Fig. 5.33 and discussed in section 5.5.1. The chemical structures of initial and final materials are illustrated in Fig. 4.2.

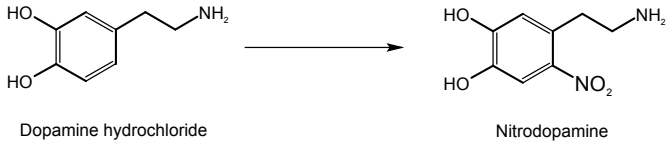

Figure 4.2: Chemical reaction presenting the synthesis of nitrodopamine

4.6.2 Conjugation of HO-PEG to nitrodopamine

Nitrodopamine (30 mg, 0.128 mmol) and N-methylmorpholine (20 mL) were loaded in a mixture of 10 mL ethanol and 2 mL chloroform. To this mixture, HO-PEG-NHS (500 mg, 0.14 mmol) was added and stirred at RT overnight. The crude product was filtered over celite (503), the filter material was washed with chloroform, and then the resultant clear green-yellowish solution was evaporated to dryness. The final product was dried at high vacuum and kept in a vacuum desiccator [119]. The chemical shifts based on ^{1}H NMR (400 MHz, $CDCl_3$, δ) are: 7.60 (s, 1H, arom. H-g), 6.93 (s, 1H, arom. H-f), 3.95 ppm (s, 2H, $CH_2 - c$), 3.2-3.8 (m, CH_2CH_2O, PEG-a,b; 2 × CH_2-d,e). The NMR spectrum is displayed in Fig. 5.33 (cf. section 5.5.1).

4.6.3 Particle phase transfer via PEGylation

The NP-OA suspensions in chloroform were transferred into water using a robust and efficient ligand exchange reaction. Typically, 1 mL of the particle suspension containing 8.9 μmol (0.5 mg) iron was mixed with 3.9 μmol (14.2 mg) of HO-PEG-nitrodopamine, incubated at RT (Thermomixer comfort, Vaudaux-Eppendorf) for 20 h while being stirred at 800 rpm. Afterwards, 10 μL triethylamine was added to block the remaining active groups and then the

mixture was incubated for another 4 h. After evaporating the solvent and drying the particles under vacuum at RT, the particles were dispersed in distilled water. Next, excessive unbound ligands were removed by ultra-centrifuging at 10000 g for 20 minutes. This process was repeated four times. The obtained pellets of the particles were dispersed in distilled water, filtered through a 200 nm syringe filter to eliminate big clusters, and stored at 4°C. The phase transfer process efficiency is about 75%. The PEGylated particles are designated as NP-PEG.

4.7 Particle functionalization with Herceptin

In order to activate the PEGylated NPs for a subsequent coupling with Herceptin antibodies, the hydroxyl terminated PEG moieties should be activated. Here, N, N'-Disuccinimidyl carbonate, a small homobifunctional NHS ester crosslinking reagent, was used to convert the hydroxyl terminal groups to NHS-carbonate ones using the protocol established by Hermanson [120]. In a typical experiment, first, the NP-PEG particles were transfered into DMF by centrifugation at 12000 rpm for 10 min. This process was repeated four times to completely exchange the solvent. After having the particles suspended in DMF ($\approx$ 0.5 mg_{NPs} mL^{-1}), 6 mg N, N'-Disuccinimidyl carbonate was added to the suspension and the mixture was incubated for 2 h at RT while being mixed at 800 rpm. Subsequently, the particles were washed three times with DMF to eliminate by-products. At last the particles were quickly washed with ice-cold water to eliminate any remaining traces of DMF prior to being redispersed in 1 mL phosphate buffer saline (coupling buffer, pH=7.4) containing 0.5 mg Herceptin and incubated for 2 h at RT while being gently shaken. Afterwards, 30 μL ethanolamine was added into the mixture to convert the unreacted NHS sites to the original hydroxyl groups. Next, an additional half an hour incubation was applied. The particles were washed three times with the coupling buffer, dispersed in 1 mL distilled water and stored at 4°C.

4.8 Isolation and infection of macrophages

Macrophages were derived from femur and tibia bone marrow of female C57BL/6 wild type mice. Bone marrow was flushed out of the bones by using ice-cold complete cell culture medium consisting of Dulbecco's Modified Eagle Medium (DMEM) medium (10 mM 2-(4-(2-Hydroxyethyl)- 1-piperazinyl)-ethansulfonic acid (HEPES), 2 mM L-glutamine, 100 U mL^{-1} penicillin, 100 mg mL^{-1} streptomycin and macrophage colony stimulating factor (PAN Biotech, Germany) at a concentration of 50 ng mL^{-1}) and cultured for 7 days at 37°C, 5% CO_2. At day 7, differentiated macrophages were harvested, counted, adjusted to 106 cell mL^{-1} and added to a 48-well tissue culture plate (250 mL $well^{-1}$) for infection. Macrophages were treated with the NP-PEG suspenions in DMEM medium at iron concentration varying from 1:10 (NP-PEG:DMEM) to 1:1000. The cells treated with 1μg mL^{-1} LPS (Sigma Aldrich, St. Louis, USA) served as a positive control and the non-treated ones as a negative control. Supernatants were collected after 24 h and used for ELISA and LDH determination.

5 Results and discussions

Iron oxide magnetic nanoparticles as biomarkers for biomedicine and bioanalysis have to be analyzed from different aspects. The information coming from the magnetic core such as size, shape, crystal structure, composition, magnetic moment and relaxation behavior are considered at first. A schema of analysis methods is displayed in Fig. 5.1. Next, the particle hydrodynamic properties, chemistry of surrounding organic compounds, toxicity and interaction with living objects seem to play a significant role in defining their suitability for *in vitro* and *in vivo* applications. In this chapter, the results obtained by employing the methods described in chapter 3 are presented and discussed. We attempt to find a correlation between the results obtained from different techniques to ultimately provide a more complete picture of iron oxide nanoparticles.

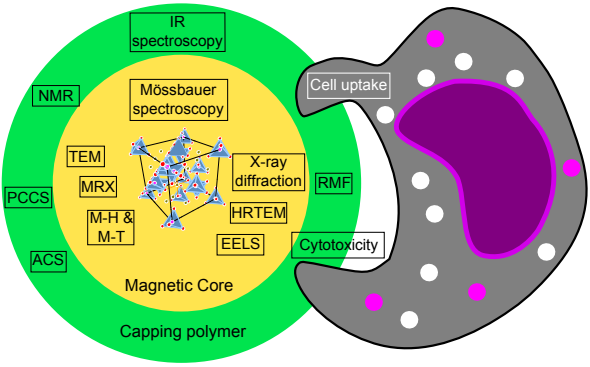

Figure 5.1: Schema of physicochemical and toxicological characterization techniques of magnetic nanoparticles.

5.1 Chemical and thermal properties of iron-oleate

Having an iron containing precursor with appropriate physicochemical properties is a vital necessity for establishing a reproducible and robust synthesis procedure. Hence, the synthesized precursor has to be characterized from different aspects. In this study, iron-oleate (Fe-OLA) was chosen owing to its promising properties (as discussed in section 5.2.3), making it a capable candidate for fabrication of monodisperse iron oxide NPs. The Fe-OLA is synthesized via a mild chemical substitution reaction (refer to section 4.3) which may be written as

$$C_{18}H_{33}NaO_2 + FeCl_3 \cdot 6H_2O \longrightarrow Fe - OLA \tag{5.1}$$

First of all, one should estimate the chemical structure of the synthesized compound. To do so, the actual percentage of hydrogen and carbon in the Fe-OLA was measured by using the EA technique (refer to section 3.1.1). The obtained results are summarized in Table 5.1.

Table 5.1: Elemental analysis results of the Fe-OLA compound

Sample notation	results (%)	
	C	H
Fe-OLA	70.53	11.59
$(C_{17}H_{33}COO)_2(C_{17}H_{33}COOH)FeO_{0.5} \cdot \frac{1}{2}H_2O$	70.6	11.07

Experimentally measured H and C percentages are in good agreement with the nominal values calculated for Fe-oleate compound with the chemical structure consisting of three oleate groups and a half of water molecule. To assess to what extent the substitution reaction was successfully performed, IR spectroscopy was employed in addition. The IR analysis was carried out on both oleic acid and the synthesized Fe-OLA and the obtained spectra are shown in Fig. 5.2.

By looking at the IR spectrum of the Fe-oleate, three bands in the range of 1400-1600 cm^{-1} appear which are absent in the IR spectrum of oleic acid. The observed bands at 1442, 1523 and 1595 cm^{-1} can be attributed to carboxylate (COO^-) groups, indicating the success of the substitution reaction. The coordination mode of carboxylate groups can be deduced from the COO^- bands separation (Δ). The separation between the bands at 1523 and 1442 cm^{-1} is $\Delta = 81$ cm^{-1}, presumably relating to bidentate mode. The bands at 1595 and 1442 cm^{-1} show a separation of $\Delta = 153$ cm^{-1}, attributing to bridging mode. The structure of Fe-OLA compound with the two mentioned coordination modes is illustrated in Fig. 5.3.

Since the particles are synthesized via the heating up procedure, knowing the thermal behavior of the Fe-OLA is required to design an appropriate synthesis scheme and chose suitable parameter ranges for temperature and heating rate. To investigate the thermal decomposition behavior of the Fe-OLA, TGA was employed as described in section 3.1.3. The TGA results are presented and discussed in section 5.2.3.

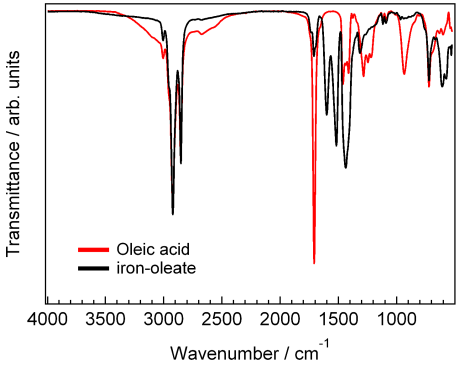

Figure 5.2: IR spectra of synthesized Fe-OLA and commercial oleic acid.

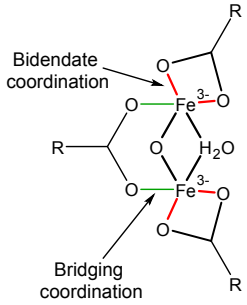

Figure 5.3: Schematic illustration of the chemical structure and the carboxylate coordination modes of the synthesized Fe-OLA.

5.2 Oleic acid capped nanoparticles

5.2.1 Core and hydrodynamic size distributions

In order to optimize the synthesis reaction, the particles fabricated via the DOE experiments (cf. Section 4.4) were characterized thoroughly. Firstly, the particle core and hydrodynamic size distributions were evaluated. In this study, the particle core size distribution was assessed using two complementary approaches based on different measurement principles. Firstly, the TEM technique was exploited as a direct method as described in the section 3.2.1. The overall TEM views of all the samples are shown in Fig. 5.4. The corresponding size histograms are plotted beside each image. By fitting the histograms with Gaussian functions, the particle mean core diameters and standard deviations were extracted as tabulated in Table 5.2. At first glance, it can be discerned that all the particles are monodisperse. Another feature which is immediately seen is that the particles can be divided into two categories with respect to their core size modality. Apparently, the particles fabricated at the higher chosen heating rate (R5, R6, R7, and R8) show mono-modal size distributions. In

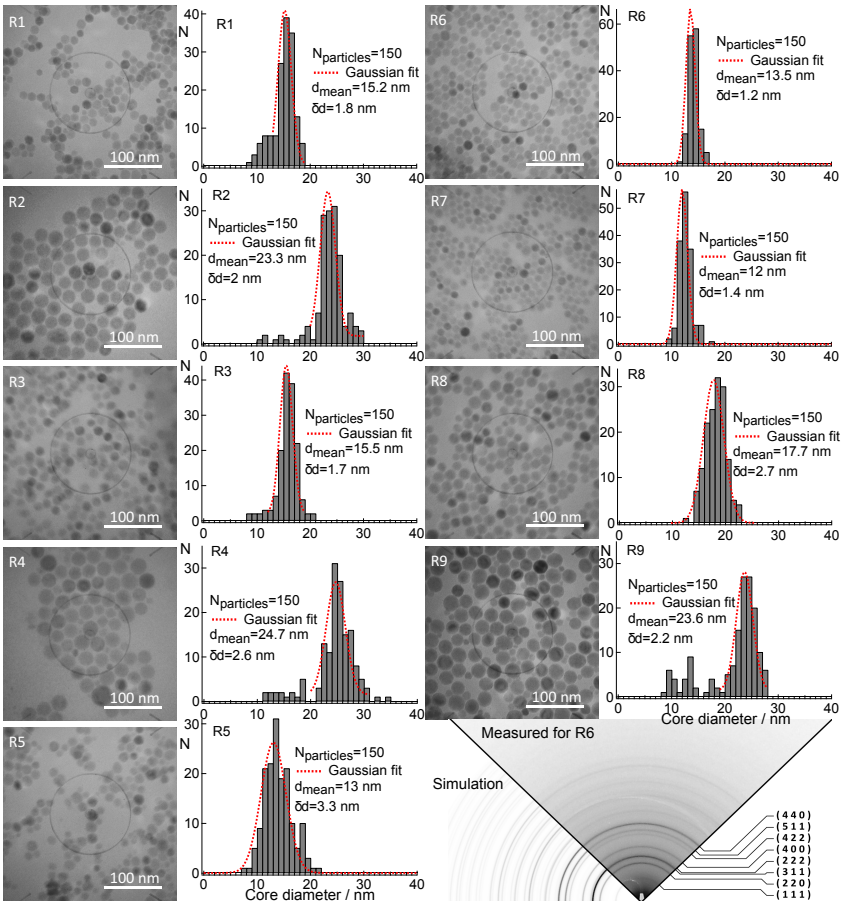

Figure 5.4: Survey TEM images of the synthesized SPIONs and their corresponding size distributions; a typical SAED pattern taken from a mono-layer of sample R6 at 100 kV and the simulated SAED pattern for Fd$\bar{3}$m spinel phase are depicted on the bottom right corner [118]. N=number of particles. © 2013 IEEE copyright.

contrast, those synthesized at the lower heating rate (R1, R2, R3, R4, and R9) reveal multi-modal size distributions, indicating a significant effect of the heating rate on the particle size distribution (cf. Table 4.1).

The destructive influence of reaction time on particle size distribution is deduced from comparing the TEM images of the samples synthesized at the same heating rate but different reaction time. This phenomenon is plausibly triggered by the occurrence of the Ostwald ripening processes with prolongation of the growth step. A typical selected area electron diffraction (SAED) ring pattern taken from a mono-layer of 13 nm particles (R6) is presented on the bottom right

Table 5.2: SPIONs synthesis conditions, hydrodynamic diameters d_{hydro}, core sizes μ_{core} and d_{core}, size distributions σ_{core} and δd_{core}, measured B and normalized flux densities $\frac{B}{V_{mean}}$ [118].

Sample name	R1	R2	R3	R4	R5	R6	R7	R8	R9
Reaction temp.	-1	+1	-1	+1	-1	+1	-1	+1	0
Reaction time	-1	-1	+1	+1	-1	-1	+1	+1	0
Heating rate	-1	-1	-1	-1	+1	+1	+1	+1	0
Fe-OLA con.	-1	+1	+1	-1	+1	-1	-1	+1	0
d_{hydro}(nm)(PCCS)	21	25	29	30	22	22.5	17	36	26
μ_{core}(nm)(MRX)	16	17.8	16	22	11.7	13	13	16	19.5
d_{core}(nm)(TEM)	15.2	23.3	15.5	24.7	13	13.5	12	17.7	23.6
σ_{core}(MRX)	0.14	0.15	0.16	0.13	0.23	0.20	0.16	0.17	0.14
δd_{core}(%)(TEM)	11.8	8.5	11	10.5	25	9	11.6	15	9.3
B(nT)[a]	3877	551	3510	1562	846	5452	3274	3764	1078
$\frac{B}{V_{\text{mean}}}$[b]	0.41	0.04	0.39	0.07	0.22	1.1	0.6	0.47	0.06

[a] Flux density B was measured at 10 mT for a sample volume of 150 μL. The sample's Fe molar concentration was adjusted to 70 mM

[b] Flux density B value at 2 mT and the mean volume of a single particle core calculated by taking the core values from MRX were utilized.

corner of Fig. 5.4. The pattern can be indexed to inverse spinel structure of iron oxide; its corresponding $d_{spacing}$ was calculated to be 8.345 Å, matching well to the $d_{spacing}$ of magnetite. For comparison, a simulated diffraction pattern of the spinel structure is shown. A perfect match with the measured pattern is discernible [118].

The particle magnetic relaxation signal was recorded using the MRX setup [99]. The recorded signals versus time are plotted in Fig. 5.5(a). The fast relaxing graphs are zoomed in for the sake of clarity and shown in the inset of the figure. These measurements were carried out on immobile samples (particles embedded in gypsum matrix) to block the particle Brownian motion and evaluate particle Néel relaxation mechanism. The particle core diameters and size distributions were derived using the MSM model given in Eq. 3.3. For the fit, it was assumed that the particle core size distribution is a lognormal function (Eq. 3.2). What is observed in the magnetic relaxation curve is the drop of the magnetic signal with time. It can be seen that by increasing the particle size from 13 to 22 nm, the magnetic relaxation drops more gradually and the relaxation time increases remarkably owing to the exponential dependence of the Néel relaxation time on the particle core volume (Eq. 1.18). Notably, some discrepancy from this expected general trend can be observed here. For example, the sample R5 (μ_c= 11.7 nm) reveals a shallower decay compared to R1 (μ_c= 16 nm) and R7 (μ_c= 13 nm). This phenomenon can be explained by the broader size distribution of R5 as clearly perceived from TEM images [118].

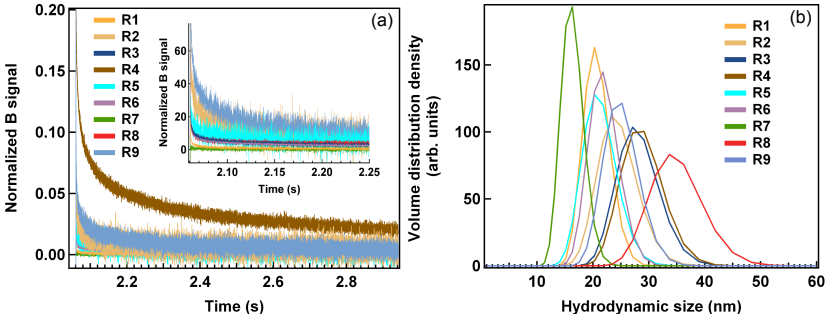

Figure 5.5: (a) SPIONs magnetic relaxation signals recorded by fluxgate magnetorelaxometry at a magnetizing field of 2 mT applied for 2 seconds and (b) volume weighted hydrodynamic size distribution of particle suspensions in chloroform [118]. © 2013 IEEE copyright.

Having particles with monodisperse magnetic core size distribution does not necessarily mean that the particles are well dispersed and non agglomerated in a suspension state. Therefore, it is vital to analyze the particle hydrodynamic size distribution to figure out which experimental synthesis condition leads us to a non-clustered sample. The particle volume weighted hydrodynamic size distributions are plotted in Fig. 5.5(b). At first glance, it is seen that all the samples show a uniform and narrow size distribution. By taking a closer look at the results, it is discerned that those particles synthesized at a Fe-OLA concentration of 1.5 mmol (R1, R6, R7) reveal a narrower size distribution compared to the ones prepared at a Fe-OLA concentration of 2 mmol. The results are summarized in Table 5.2. A presence of a small fraction of agglomeration and eventually size broadening is seen in the samples grown for 60 min (R3, R4, and R8). This observation suggests the occurring of the Ostwald ripening and an additional nucleation step (the presence of 8-12 nm NPs in R3 and R4 TEM images) with prolongation of the growth step [118].

5.2.2 Static and dynamic magnetic properties

Particularly for magnetic ferrofluids, by studying the particle dynamic properties solely by employing scattering based measurements such as PCCS, some features may be overlooked. Therefore, we have evaluated the particle dynamic properties from another aspect using ac susceptibility (ACS). The normalized real and imaginary part of the frequency dependent ac susceptibility measurements are shown in Fig. 5.6(a). The measurements were carried out at conditions described in section 3.5.4. Unlike PCCS which is solely based on particle Brownian motion, in ACS both Brownian and Néel relaxations take place. As discussed in section 3.5.4, the Brownian peak seen in the imaginary part can be modelled using an adapted Debye model given in Eq. 3.23 [114, 121]. Clear Brownian peaks were observed only for R2, R4 and R9 in the measurement window. By taking the core properties from MRX, M_s= 480 kA m^{-1} and K= 7 kJ m^{-3}, we have modelled the results for R4. A hydrodynamic diameter of 28 nm was

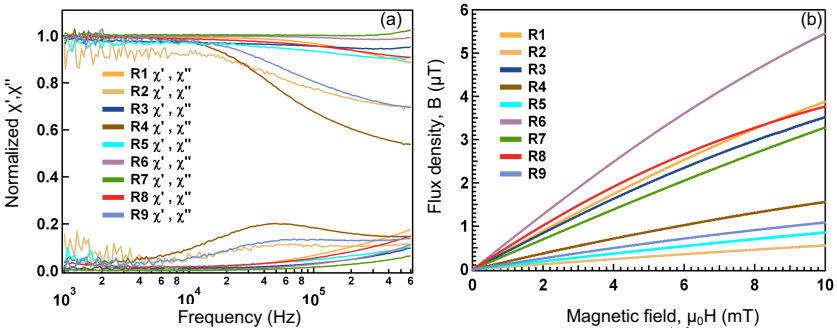

Figure 5.6: (a) Normalized real and imaginary part of the frequency dependent as susceptibility measurements and (b) Flux density B versus magnetic field H performed on 150 μL SPION suspensions in chloroform; the $B-H$ samples have 70 mM Fe [118]. © 2013 IEEE copyright.

obtained, matching with the PCCS value. It is worth noting that for most samples, the real part retains constant up to 600 kHz due to their small core sizes and the consequent domination of the Néel mechanism [118].

Particles with appropriate magnetic properties are required for biomedical applications. To gain a qualitative impression about the particle magnetic moment, the flux density B was measured using a fluxgate-based measurement setup [20]. In a typical measurement, 150 μL particle suspension with an iron concentration of 70 mM is placed into the setup and a DC magnetic field $\mu_0 H$ up to 10 mT is applied. Fig. 5.6(b) shows the results. Since the measured B signal depends on the sample geometrical position with respect to the fluxgate sensor, it is not the sample flux density. Nevertheless, it relates to the sample magnetic moment m_{sample} via $B = G \cdot m_{sample}$, with G a geometry factor. Provided that for small magnetic fields the $L(m,H)$ term is proportional to $\xi/3$ and performing simple mathematics, the relation between B and M_s is given by [118]

$$\frac{B}{V_{mean}} \propto M_s^2. \tag{5.2}$$

To be restricted to the linear magnetization regime, the B values at 2 mT were taken to calculate the B/V_{mean} term. The resultant values are tabulated in Table 5.2. Interestingly, those particles fabricated at the heating rate of 3°C/min (R6, R7, and R8) reveal higher magnetizations compared to the ones prepared at the low heating rate (R2, R4, and R9). This finding is in contrast to the expected increase in the linear magnetization susceptibility by enlarging the particle size. This anomalous behavior of bigger particles will be addressed thoroughly in the section 5.3. However, a reasonable size dependent magnetization behavior is seen for the samples with the comparable magnetic core diameter and size distribution (R1, R3, and R8) as long as the mean core size is below 18 nm [118].

5.2.3 Particle formation and growth mechanisms

The particle hydrodynamic and core size results were analyzed using a linear multiple regression model and exploiting Statistica 7 software. We find the hydrodynamic diameter depends on reaction temperature and time, Fe-OLA concentration and their interactions via an empirical model given by [118]

$$\begin{aligned} d_{hydro}(nm) = 25.4(nm) + 0.3(nm) \times (T - 327) + 0.18(nm) \times (t - 45) \\ +10.75(nm) \times (c - 1.75) + 0.01(nm) \times (T - 327) \times (t - 45) \\ +0.48(nm) \times (t - 45) \times (c - 1.75), \end{aligned} \quad (5.3)$$

with T, t and c in °C, minute and mmol, respectively. The model shows a reliable coefficient of determination of $R^2 = 0.96$ [118].

We succeeded in deriving a reasonable model if and only if the 2-factor interaction terms $T \times t$ and $t \times c$ are involved in the fit. The 2D contour plots of the model equation are visualized in Fig. 5.7. The plots represent the simultaneous impact of two synthesis parameters on the hydrodynamic diameter while the other parameters are set to their medium levels.

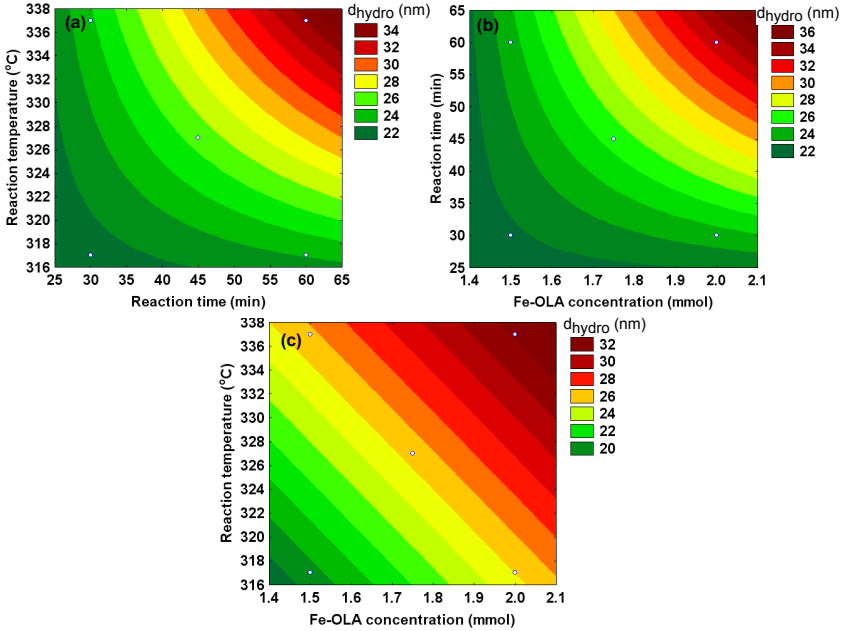

Figure 5.7: Contour plots showing the dependencies of the particle hydrodynamic size on reaction temperature and time and Fe-OLA concentration [118]. © 2013 IEEE copyright.

A noticeable feature which is deduced from the curved contour lines in both Figs. 5.7 (a) and (b) is the non linear dependencies of the hydrodynamic diameter on reaction temperature and time and reaction time and Fe-OLA concentration. It can be seen in both (a) and (b) that the hydrodynamic diameter grows up to $\approx$ 36 nm when both parameters are set to their high levels. The change in the hydrodynamic diameter is marginal when any of them is set to its low level. Conversely, the hydrodynamic diameter shows a linear dependence on reaction temperature and Fe-OLA concentration (shown in Fig. 5.7 (c)) as no interaction term between these two parameters is involved in Eq. 5.3. If one of them increases within the chosen range, the hydrodynamic diameter grows for about $\approx$ 6 nm no matter the other one is set to its low or high level [118].

After analyzing the core diameters acquired from MRX and TEM dependence on the varied factors, no empirical model with a reliable coefficient of determination R^2 was found. It has to born in mind that the DOE statistical analysis of results makes sense only if no qualitative changes such as phase transformation occur in samples. Despite not being able to derive an empirical model for particle core growth, we find that the particle core diameter grows linearly by decreasing the heating rate from 3°C/min to 1°C/min and increasing the reaction temperature from 317°C to 337°C. There is a good agreement between the particle core diameters obtained from MRX and TEM with the exception of R2, R4 and R9. Some general reasons can be given for these discrepancies. The first one is the assumption of a mono-modal lognormal distribution (Eq. 3.2) taken in MRX analysis although the particles show a multi-modal size distribution in TEM. The anomalous magnetization behavior observed for this set of samples in the $B - H$ measurements (5.6(b)) can also account for this observation. It seems that there is a fraction of non-magnetic/paramagnetic phase in the larger particles. This topic is discussed more fully in section 5.3.

We have realized that in order to establish a reproducible synthesis reaction, we have to gain a deeper understanding of the dominating nucleation and growth processes in the current synthesis reaction. This led us to study the thermal decomposition behavior of Fe-OLA by TGA to elucidate the correlation between the core properties (mean core diameter, size modality and size broadening) and the nucleation and growth phenomena. Fig. 5.8 displays the TGA results acquired at a heating rate of 3°C/min. Obviously, four clear weight loss steps labeled with a, b, c and d are seen. The step a, launched at around 160°C and terminated at 260°C, can be related to the dissociation of two symmetric oleate groups with lower binding energies. The second weight loss step b, occurred from 260°C to 310°C, can be assigned to the dissociation of the third oleate molecule. The dissociation process can be described by the ketonic decarboxylation reaction given by [118]

$$Fe(RCOO)_3 \xrightarrow{\Delta} RCOR + RCOOFe - O + CO_2 \tag{5.4}$$

Additionally, we have monitored the dissociation behavior of oleate groups by IR spectroscopy on both fresh Fe-OLA precursor and a sample taken from the R5 experiment at 0 min aging time. The IR spectra are plotted in Fig. 5.9. It

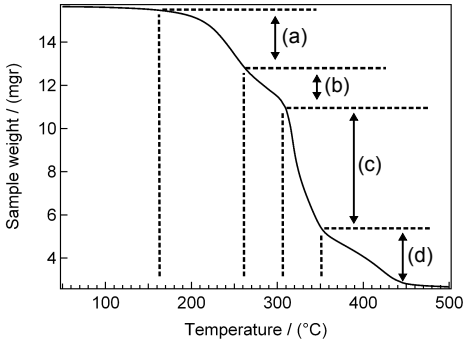

Figure 5.8: TGA plot of the synthetic Fe-OLA recorded at a heating rate of 3°C/min [118]. © 2013 IEEE copyright.

can clearly be seen that the -COO^- bands in the 1400-1700 cm^{-1} range vanish after heating to ≈ 317°C. This attributes to the dissociation of the coordinating oleate groups via Eq. 5.4 and a gradual saturation of iron oxygen units bound to oleic acid groups (designated as monomers). Eventually, the monomers saturate and reach the supersaturation level $S_{critical}$. These circumstances result in the nucleation of tiny monodisperse primary crystallites (ref. section 2.3.3). It can be concluded that the nucleation processes obey the La Mer model [118].

The most prominent weight loss step c, happening between 310°C and 350°C, is attributed to the formation of a huge amount of monomers and the consequent onset of burst and sudden nucleation. For further examination, the sample taken for the IR measurements was analyzed by TEM to assess if the primary crystallites have already been formed. Notably, no particles are crystallized at temperatures below 317°C. Another feature is that such a huge weight loss happens in a short period of time indicating a quick consumption and transformation of monomer building blocks into monomers. This type of decomposition behavior is a prerequisite for the synthesis of monodisperse NPs. By further heating above 350°C (d), the organic compounds are steadily vaporized [122].

Based on the nucleation theory (cf. section 2.3.1), the nucleus critical size n_{cns} depends inversely on temperature and the relative monomer saturation S. Accordingly, by delaying the nucleation to higher temperatures with increasing the heating rate, S rises and therefore many nuclei with small n_{cns} crystallize. The occurrence of such an intensive nucleation causes a significant drop in the monomer concentration, yet enough to provide an intensive and short growth step. The delayed nucleation and quickly terminating growth mechanisms account for the formation of highly monodisperse NPs with relatively small core sizes ≈ 12-14 nm in R6 and R7 [123]. Owing to a drastic consumption of the monomer in the nucleation and growth processes, the reaction system experiences a lack of the monomer for further growth and thereby the growth mode switches to the reaction controlled one. Consequently, the Ostwald ripening process occurs which widens the particle size distribution. The occurrence of size defocusing mechanisms can clearly be seen in R8 which aged for 60 min [118].

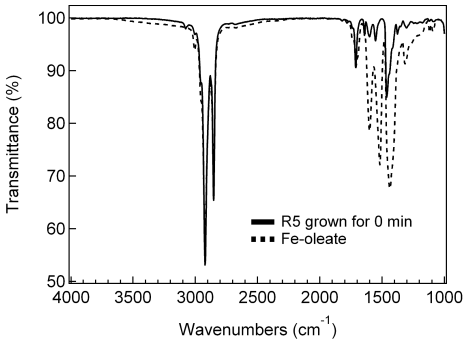

Figure 5.9: FTIR spectra of Fe-OLA and a sample taken from the R5 experiment at 0 min growth [118]. © 2013 IEEE copyright.

By decreasing the heating rate to 1°C/min, we expect that the previously discussed Fe-OLA decomposition steps, Fig. 5.8, in particular the step c, shift towards lower temperatures and reveals a slower decay. This phenomenon has been proven experimentally by Palchoudhury et al. [122]. This circumstance has two general consequences on the nucleation and growth. The first one is the happening of a premature nucleation which means that the nuclei do not form via the burst nucleation mechanism after reaching to the $S_{critical}$ but oppositely via a gradual process and at lower S values. This leads to the formation of fewer nuclei with bigger critical sizes, coinciding with Eq. 2.3. Another impact is the occurrence of a gradual growth process. In this condition, the synthesis reaction never reaches to the $S_{critical}$ and for a long period of time a small quantity of the monomer is fed into the system. By looking at the TEM images of R2 and R4 (1°C/min for 60 min), it is seen that the particles with a mean core size of $\approx$ 24 nm can be synthesized via this strategy, but they show a rather broad and even multi-modal size distribution [118].

Since the nucleation energy barrier (cf. Eq. 2.4) is larger than the growth, the nucleation rate is more easily affected by temperature change than the growth. This means if the reaction system is gradually heated up from $\approx$ 310°C to the reflux temperature, an additional nucleation may occur. This explains the presence of tiny nanocrystals in R2, R4 and R9. Particles with a mean magnetic core diameter $>$ 20 nm can be produced if the heating rate is retarded to 1°C/min. Nonetheless, due to the aforementioned mechanisms, these particles are susceptible to size broadening and often show a bi-modal size distribution. Notably, as deduced from the $B-H$ results, the larger particles reveal deteriorated magnetic properties. These topics are addressed in section 5.3.5.

Ex-situ monitoring of particle crystallization and growth

To more deeply evaluate the crystallization and growth mechanisms proposed in the previous section, we have studied how the particle size distribution and morphology evolve in the course of the growth process. For this purpose, we

have monitored the R8 synthesis experiment by taking aliquots after 0, 10, 30, 45 and 60 minutes of the growth. Fig. 5.11 shows the survey TEM images of the aliquots.

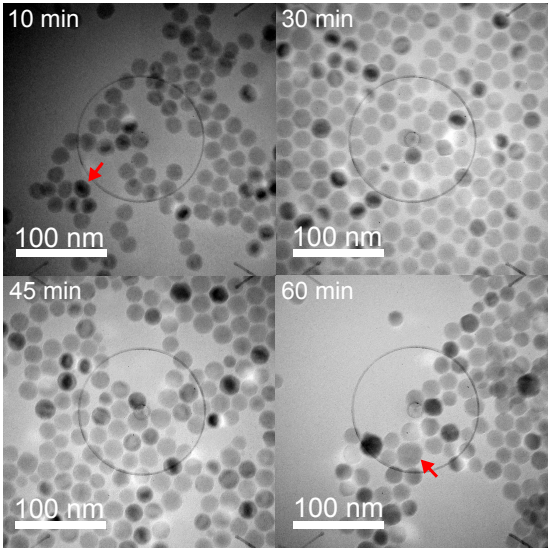

Figure 5.10: Temporal evolution of the particle size and shape in the course of growth in the synthesis reaction performed at c=2 mmol, t=60 min, T=337°C and r=3°C/min.

Remarkably, no particles were extracted from the sample taken at 0 min and therefore no TEM image is shown. Interestingly, after 10 min of aging at 337°C, non uniformly shaped particles with a mean core size of 17.4 nm were formed. Some particles show an elongated irregular morphology marked with white arrow in the figure. Besides, these particles are not faceted and apparently not well crystalline. In fact, this finding helps us to understand how fast the burst nucleation and fast growth mechanisms can result in the formation of such large particles. After 30 min of aging, a significant change particularly in the particle morphology is observed. The faceted particles with octahedral morphology, making a uniform monolayer on the TEM grid, evolve. The appearance of such an ordered monolayer is an indication of the particle size monodispersity. Notably, the growth time has a marginal effect on the particle mean core size and morphology and any substantial change in both features is barely detectable over the monitored period of time. However, it seems that the particle size deviation tends to become broader by further aging to 60 min. The size broadening caused by the Ostwald ripening starts to happen after the monomer supply is depleted as discussed thoroughly in section 5.2.3. The existence of some bigger particles, marked with black arrow, is an evidence of the happening of the aforementioned size broadening mechanisms.

The change in the particle hydrodynamic size distribution versus the growth time is shown in Fig. 5.11. Obviously, the state of particle clustering does depend on the growth time unlike to the particle core size. Interestingly, during the first 45 min of the aging process, although the particle core size remains nearly unchanged, but a decreasing trend in the hydrodynamic size is observed as plotted in Fig. 5.11(b). The particles formed after 10 min show a broad size distribution with a mean hydrodynamic diameter of 33 nm. Notably, these particles are transformed to monodisperse 23-24 nm NPs after 30-45 min of aging at 337°C. It seems that the freshly born particles are vesicles filled with two to three particles covered with more than a layer of OA molecules, explaining their larger hydrodynamic size. Provided that the length of a single OA molecule is ≈ 2-2.5 nm [78] and by knowing from the TEM studies that the mean core size is ≈ 18 nm, it can be concluded that the particles obtained after 30 and 45 min of refluxing are capped with a single layer of OA molecules. However, by further aging from 45 to 60 min, the hydrodynamic size rises from 24 to 40 nm and its deviation becomes much broader (Fig. 5.11(a). The OA molecules tend to decompose to compounds with higher molecular weight by keeping at high temperatures for a long time. This phenomenon is experimentally characterized by observing a gradual rise in the reflux temperature from 10 to 60 min of aging. The decomposed OA molecules leave the particle surface, resulting in a shorter particle to particle distance and stronger magnetic dipole-dipole interactions.

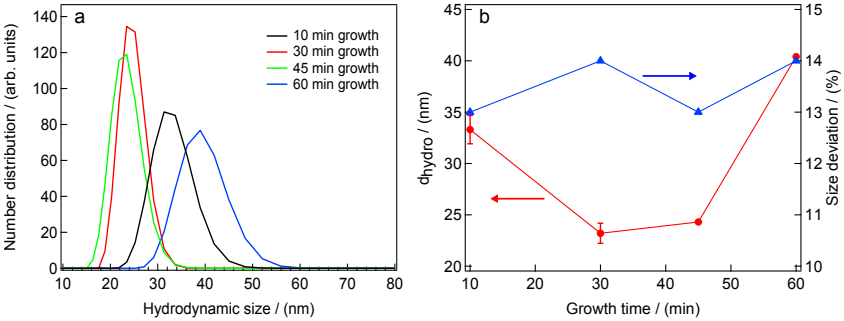

Figure 5.11: (a) Time dependent change in particle hydrodynamic size distribution and (b) temporal evolution of particle hydrodynamic size and size deviation during the growth process in the synthesis reaction performed at c=2 mmol, t=60 min, T=337°C and r=3°C/min.

To find out how the particle magnetic properties change with the growth time, the sample flux density B as a function of a DC magnetic field $\mu_0 H$ was measured. The $B-H$ curves are plotted in Fig. 5.12(a). Interestingly, the particles show a slight growing trend in the magnetization up to 45 min of the growth and then it soars to higher values as plotted in Fig. 5.12(b) (blue line). Notably, the particle mean core size changes marginally over the growth period as shown in the same graph (red line).

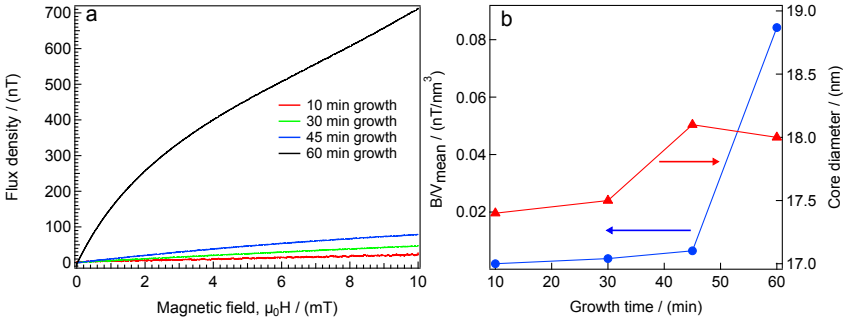

Figure 5.12: (a) Flux density B versus magnetic field $\mu_0 H$ measured on the aliquots taken at different growth times and (b) growth time dependent change in particle core size and B/V_{mean} values. The $B-H$ measurements were performed on 150 μL of particle suspensions with an iron concentration of 10 mM Fe. The synthesis conditions are c=2 mmol, t=60 min, T=337°C and r=3°C/min (cf. Table 4.1).

It seems that the particles undergo significant structural and compositional changes via aging at the reflux temperature. On the one hand, the particle degree of crystallinity increases by further letting the reaction mixture to mature. This can easily be deduced by comparing the TEM images of the 10 and 30 min aliquots. Besides, it is generally agreed that the particles fabricated via chemical processes suffer from a poor spin ordering particularly on the surface. It appears that keeping for a longer period of time at 337°C facilitates the crystal reconstructing and ordering and shrinks the thickness of a so-called magnetic dead layer on the particle surface. Nevertheless, if we compare the magnetic properties of small 12-13 nm NPs with 22-24 nm ones discussed in Fig. 5.6, a huge difference in their magnetic properties is seen which can not solely be attributed to their higher atomic ordering and crystallinity and thinner magnetic dead layer. The unusual dependence of the particle magnetic properties on its core size interested us to explore the particle structural, compositional and magnetic properties. The results on these matters are discussed in section 5.3.

5.2.4 Robustness of the synthesis procedure

In this section, we present and discuss the robustness of the developed synthesis process by three times repeating two different sets of experiments. In the identical synthesis trials, the Fe-OLA from various precursor synthesis batches was used to additionally assess and show the stability of the precursor synthesis method. Typical TEM micrographs of the three particle batches synthesized using the experimental conditions given in Table 5.2 for R8 are displayed in Fig. 5.13. The analyzed size histograms are shown below their corresponding images. Apparently, all three batches reveal comparable size and morphology distributions.

To show that the reproducibility of the synthesis procedure is independent of the chosen experimental conditions, we have repeated R8 at T=357°C three times. Fig. 5.14 depicts the recorded TEM images of the batches, labeled

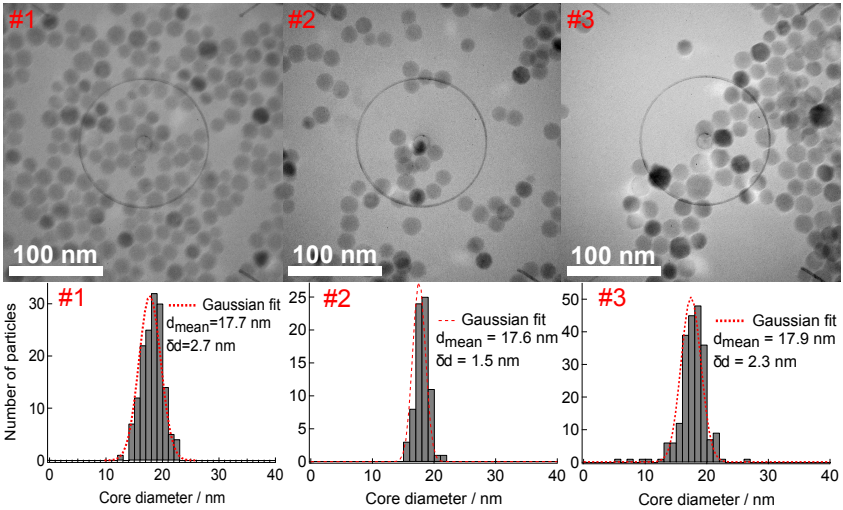

Figure 5.13: Typical TEM images of three samples synthesized by repeating R8 experimental conditions: c=2 mmol, t=60 min, T=337°C and r=3°C/min.

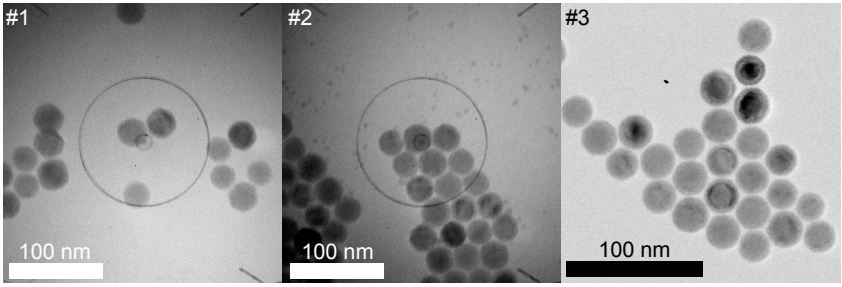

Figure 5.14: Survey TEM images of three samples produced at c=2 mmol, t=60 min, T=357°C and r=3°C/min synthesis conditions.

with #1, #2 and #3. All three samples show a narrow size distribution with faceted morphology. Based on these two series of experiments, the reliability and robustness of the investigated synthesis method can be understood.

5.3 Correlating structural, compositional and magnetic properties

Having optimized the particle synthesis process and shown its reliability for producing particles with identical size and shape distributions, we become motivated to correlate the particle size distribution to structural, compositional and magnetic properties for a broad range of mean core sizes. This approach

ultimately allows us to find out the reasons for the observed anomalous magnetization behavior in larger NPs. To this end, we have synthesized three sets of samples with a mean core diameter of 13, 18 and 24 nm to systematically study how the particle magnetic properties depend on their size, crystal structure and phase composition. Since the iron oxide phases are prone to oxidation even by storing at ambient conditions, the freshly synthesized particles were studied. The 13 and 18 nm NPs were synthesized by performing R6 at 2 mmol and R8, respectively. To synthesize 24 nm NPs, the reflux temperature increased to 357°C whilst the other synthesis parameters were set similar to the R8. To accomplish this task, a wide variety of characterization techniques such as HRTEM/SAED, XRD, Mössbauer spectroscopy and field and zero field cooled magnetization measurements were employed. The findings are the topics of the next sections.

5.3.1 High resolution TEM and SAED studies

The HRTEM, SAED and FFT analyses were used to investigate the correlation between particle crystal structure and its magnetic core size. Fig. 5.15 (a) shows a typical TEM micrograph of 13 nm iron oxide NPs. The particle size distribution was evaluated using ImageJ software and the histogram is plotted in Fig. 5.15 (b). It can be seen that the particles reveal a narrow size distribution with a mean diameter of 13±1 nm. The SAED technique was employed to unravel the particle crystal structure. The SAED pattern taken from stacks of particles to provide an overall picture is shown in the inset of Fig. 5.15 (c). To analyze the patterns, we have exploited the line scan technique to generate a line scan pattern out of its corresponding SAED one. Fig. 5.15(c) shows the line scan pattern obtained for the 13 nm NPs. The peak positions match with the powder diffraction file (No: 01-089-0688) of the magnetite phase (black marks) and also the SAED pattern is characteristic of magnetite NPs [47, 124].

To gain a deeper understanding of the particle crystal structure, the HRTEM technique was employed. The HRTEM micrograph of a 13 nm particle is displayed in Fig. 5.16(a). The particle is a perfectly ordered single crystal with a truncated octahedral morphology. To approximate the interplanar $d_{spacing}$ of the crystallographic planes aligned parallel to the electron beam, a plot profile was taken from a selected section as displayed in Fig. 5.16(b). An ordered plot profile was obtained indicating the ordering of the crystal planes. The lattice $d_{spacing}$ was estimated to be 0.251 nm, matching well with $\{311\}_{Fe_3O_4}$. The contribution of $\{311\}_{Fe_3O_4}$ and $\{422\}_{Fe_3O_4}$ planes can be found in the FFT generated pattern as shown in Fig. 5.16(c). In order to see the crystal arrangement of $\{422\}_{Fe_3O_4}$ planes, the particle lattice image was reconstructed by the inverse FFT technique after excluding the $\{311\}_{Fe_3O_4}$ spots. The reconstructed lattice image is displayed in Fig. 5.16(d). The $d_{spacing}$ of the crystalline planes was estimated to be 0.168 nm, in agreement with $\{422\}_{Fe_3O_4}$. From the particle morphology evolution point of view, the particle shape is determined by the competition between the bulk and surface/interface energies. The energy order of the main crystallographic planes in a cubic structure may hold, $\sigma\{111\} < \sigma\{001\} < \sigma\{101\}$. By only considering the effect

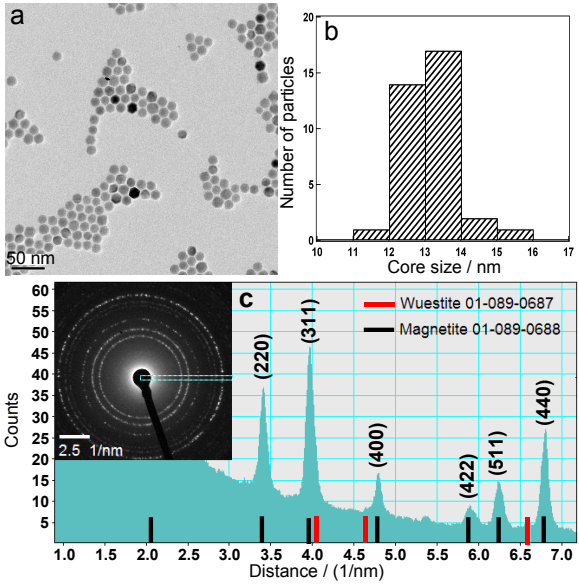

Figure 5.15: (a) Typical TEM micrograph of 13 nm NPs, (b) its corresponding size histogram and (c) line scan pattern obtained from SAED pattern shown in the inset [124]. Reproduced by permission of The Royal Society of Chemistry.

of the surface energy, particles tend to form octahedrals surrounded by {111} planes. Nonetheless, the surface area of the main planes reveals a different sequence in which $s\{111\} > s\{101\} > s\{001\}$. Hence by allowing for the impact of the surface area, a truncated octahedral (Wigner-Seitz crystal [104]) will be the most stable morphology of magnetite NPs as visualized in the inset of Fig. 5.16(a).

The particle mean core size grows to 18 nm by increasing the reaction time to 60 min whilst the other synthesis conditions are kept similar to what used for the former sample. A survey TEM image is depicted in Fig. 5.17(a). The particles reveal a narrow size distribution with a mean diameter of 18±1.5 nm as plotted in Fig. 5.17(b). To analyze the particle size distribution, a typical TEM image containing few hundred particles was analyzed analogously to the 13 nm NPs. Notably, the particle size deviation has not shown a substantial alteration after the growth. Fig. 5.17(c) reveals the acquired line scan pattern for the 18 nm NPs and its corresponding SAED pattern is displayed in the inset. It can clearly be seen that by further growth of the particle size from 13 to 18 nm, the line scan peaks broaden and shift towards the interplanar spacing values coinciding with the powder diffraction file (No: 01-089-0687) of FeO (red marks) [124].

Interestingly, by solely increasing the growth temperature to 357°C and preserving all the other parameters likewise to the former sample, the mean core size rises to 24±1.3 nm as shown in Fig. 5.18(a). Obviously, the particles are

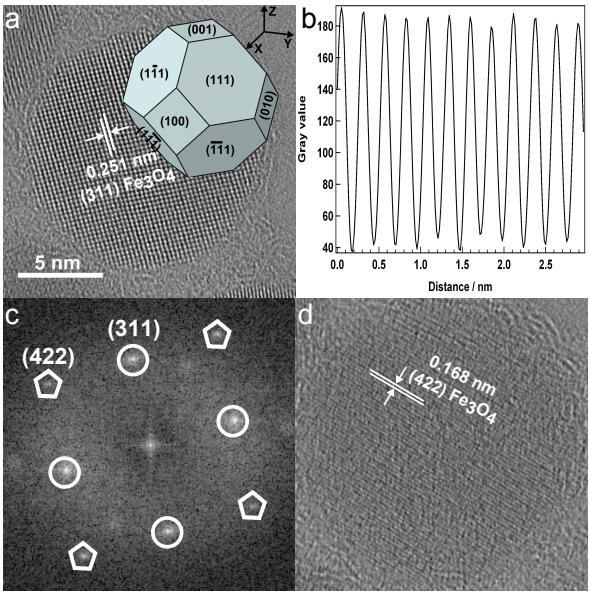

Figure 5.16: (a) HRTEM image of a single 13 nm NPs; the inset is a 3D visualization of a Wigner-Seitz crystal, (b) plot profile taken from a selected area, (c) the corresponding FFT generated pattern and (d) the inverse FFT reconstructed lattice image after filtering the $\{311\}_{Fe_3O_4}$ spots.

highly monodisperse faceted octahedrons with a standard size deviation $< 6\%$ (Fig. 5.18(b)). What is easily noticeable in the line scan pattern obtained for these particles, shown in Fig. 5.18(c), is that the peaks positions shift further towards the nominal peaks positions of FeO (e.g. compare the $\{111\}_{FeO}$ position in Fig. 5.18(c) and Fig. 5.17(c)). Also, those peaks become more distinct and pronounced. This observation indicates that the 24 nm NPs contain a larger fraction of FeO phase compared to the 18 nm ones. For the sake of simplicity, only the major diffraction peaks of FeO and Fe_3O_4 are marked in the line scan patterns.

It is known that the iron-oleate is decomposed via the ketonic decarboxylation reaction (5.4) in which CO and H_2 reductive gases are released [122]. This circumstance leads to the reduction of Fe^{3+} to Fe^{2+} in monomers (i.e. the building blocks), resulting in the formation of tiny crystallites primarily made of FeO. FeO is a non stoichiometric and thermodynamically unstable phase of iron oxide with a defective NaCl crystal structure whereby oxygen atoms occupy a fcc sublattice and Fe^{2+} fills tetrahedral and octahedral interstitial sites. Owing to a large number of vacancies in its structure, travelling of oxygen atoms from surface towards the center and Fe^{2+} atoms from the center towards the interface of FeO and Fe_3O_4 cause oxidation of Fe^{2+} to Fe^{3+}. Hence FeO tends to transform to the thermodynamically most stable phase, i.e. magnetite.

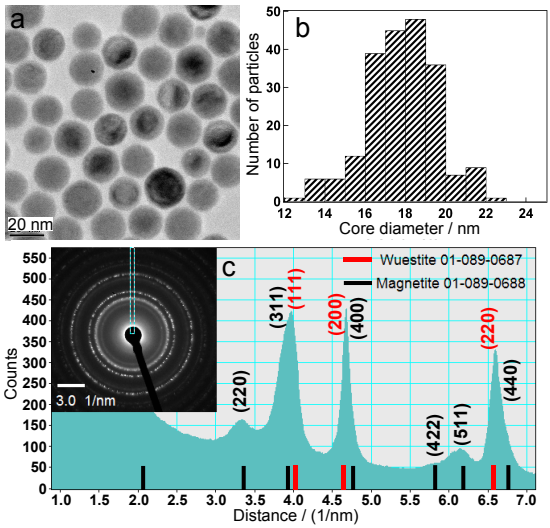

Figure 5.17: (a) Typical TEM micrograph of 18 nm NPs, (b) its corresponding size histogram and (c) line scan pattern acquired from SAED pattern illustrated in the inset [124]. Reproduced by permission of The Royal Society of Chemistry.

Since the diffusion length is rather short in the 13 nm NPs, a complete oxidation to magnetite may occur in the course of growth, cooling and separation. Further growth of the particle size to 18 and 24 nm, literally meaning a longer diffusion path, hampers the oxidation process. This eventually leads to the formation of FeO/Fe_3O_4 NPs [124].

To identify the crystal structure of these biphasic particles and also in an attempt to approximate the phase distribution within a particle, the HRTEM technique was utilized. The HRTEM image of a 18 nm NPs is depicted in Fig. 5.19(a). The contribution of $\{311\}_{Fe_3O_4}$ crystallographic planes is seen in the FFT pattern shown in Fig. 5.19(b). Besides, the spots (marked with squares) can simultaneously be ascribed to $\{400\}_{Fe_3O_4}$ and $\{200\}_{FeO}$ planes. In order to identify the orientation of these crystalline planes, the plot profiles were recorded from the particle core and shell. Fig. 5.19(b) shows the profile taken in the direction of the blue arrow. The fringe is estimated to be 0.218 nm, coinciding with $\{400\}_{Fe_3O_4}$ and $\{200\}_{FeO}$ lattice fringes. The profile recorded in the direction of the green arrow is plotted in Fig. 5.19(d) and the approximated fringe is 0.268 nm, matching with $\{311\}_{Fe_3O_4}$ lattice fringe.

In order to exclude the contribution of some crystallographic planes and being solely restricted to one crystalline direction at a time, we have performed a series of inverse FFT image reconstruction while certain diffraction spots are filtered. At first, the image was reconstructed after masking the $\{400\}_{Fe_3O_4}$ and $\{200\}_{FeO}$ spots as shown in Fig. 5.19(e). In the reconstructed lattice image, the $\{311\}_{Fe_3O_4}$ planes are barely discernible in the center and also being oriented in various directions in the shell as if they form several crystalline domains.

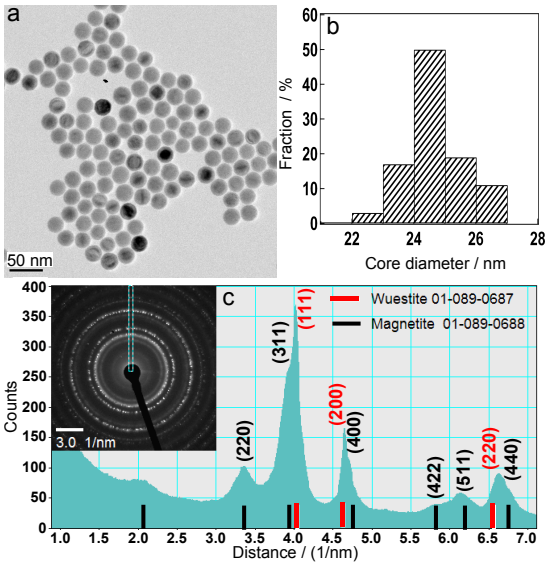

Figure 5.18: (a) Typical TEM micrograph of 24 nm NPs, (b) its corresponding size histogram and (c) line scan pattern obtained from SAED pattern displayed in the inset [124]. Reproduced by permission of The Royal Society of Chemistry.

The presence of lattice dislocations can easily be seen too. This circumstance induces strain in the particles, characterized by atomic displacement, as seen in the FeO/Fe_3O_4 NPs (marked with a white zig-zag in Fig. 5.19(e)). This phenomenon has been observed by Levy et al.[125] in iron oxide NPs synthesized via seed-mediated growth. In another attempt, the image was re-generated after filtering the $\{311\}_{Fe_3O_4}$ spots and the resultant image is revealed in Fig. 5.19(f). Interestingly, the $\{400\}_{Fe_3O_4}$ and $\{200\}_{FeO}$ planes are well ordered in the center and barely differentiable in the shell. It is worth mentioning that the crystal structure is nearly free of dislocations in the center [124].

Fig. 5.20(a) shows the HRTEM image of a single 24 nm NP. Obviously, a more defective structure containing some twinning defects is identified for this sample. Its FFT pattern, shown in Fig. 5.20(b), resembles the one acquired for the 18 nm NPs. The pattern presents the contribution from all the aforementioned crystalline planes. A noticeable feature in this pattern is the appearance of several diffraction spots assigned to $\{311\}_{Fe_3O_4}$. They nearly form a diffraction ring (white circle) indicating that the Fe_3O_4 planes form several crystalline domains on the shell. To approximate the lattice fringes at different spots, the plot profile analysis was carried out. The profile obtained on the shell in the direction of the blue arrow is demonstrated in Fig. 5.20(c). The interplanar $d_{spacing}$ of the planes in this direction is 0.199 nm, agreeing with the nominal $d_{spacing}$ of $\{400\}_{Fe_3O_4}$. The profile #2 and #3 fringes, Fig. 5.20(d) and (e), correspond to a lattice $d_{spacing}$ of $\{311\}_{Fe_3O_4}$ and $\{200\}_{FeO}$, respectively.

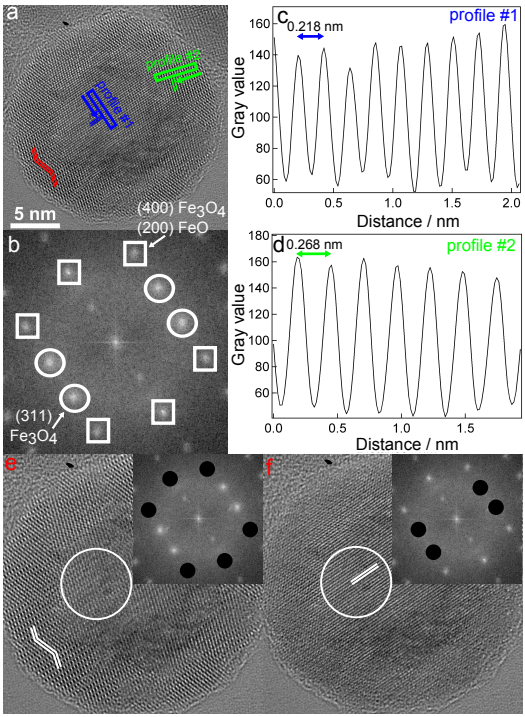

Figure 5.19: (a) HRTEM micrograph of a single 18 nm NPs, (b) its corresponding FFT pattern, plot profiles taken from the particle (c) core and (d) shell and the inverse FFT reconstructed lattice images after masking (e) $\{400\}_{Fe_3O_4}$ and $\{200\}_{FeO}$ and (f) $\{311\}_{Fe_3O_4}$ spots; the masked SAED patterns are shown in the inset [124]. Reproduced by permission of The Royal Society of Chemistry.

For the inverse FFT reconstruction, this sample was treated analogously to the 18 nm NPs. The reconstructed image after excluding the contribution of the $\{400\}_{Fe_3O_4}$ and $\{200\}_{FeO}$ spots is shown in Fig. 5.21(a). The generated image reveals a non-crystalline center surrounded by those aforementioned domains consisting of the $\{311\}_{Fe_3O_4}$ planes. Having reconstructed the image by masking the $\{311\}_{Fe_3O_4}$ spots, a well ordered crystalline structure spreading through the whole particle is seen as displayed in Fig. 5.21(b). On the whole, it was found that by filtering the planes exclusively attributed to Fe_3O_4, a neat crystal structure is reconstructed. Conversely, by masking both FeO and Fe_3O_4 planes, an image with a disordered center and differently directed domains on the shell is generated. In summary, it can presumably be assumed that FeO and Fe_3O_4 phases are mainly located in the center and the shell of the particles, respectively. Besides, it appears that an epitaxial growth of Fe_3O_4 from the surface towards the inner regions is accounted for the formation of the crystalline domains and the induction of lattice defects and strained regions [124].

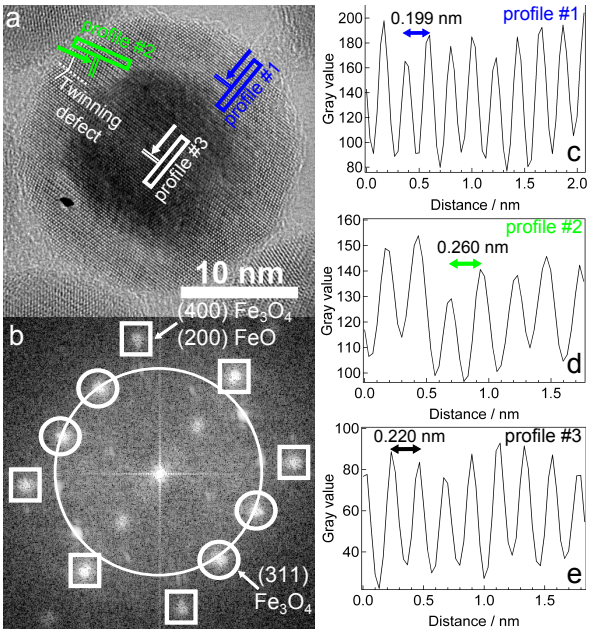

Figure 5.20: (a) HRTEM image of a 24 nm NP, (b) its associating FFT pattern and plot profiles taken from particle (c),(d) shell and (e) core [124]. Reproduced by permission of The Royal Society of Chemistry.

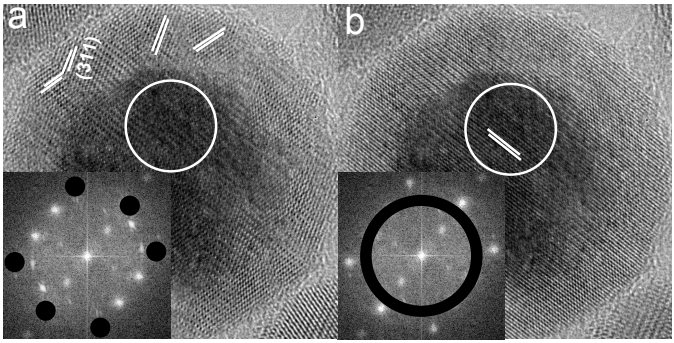

Figure 5.21: Inverse FFT reconstructed lattice image of the 24 nm NPs shown in Fig. 5.20 after masking (a) $\{400\}_{Fe_3O_4}$ and $\{200\}_{FeO}$ and (b) $\{311\}_{Fe_3O_4}$ spots; the masked FFT patterns are shown in the inset [124]. Reproduced by permission of The Royal Society of Chemistry.

5.3.2 Powder X-ray diffraction investigations

In addition to the HRTEM and electron diffraction studies, powder X-ray diffraction (XRD) was exploited. XRD enables one to evaluate particle crystal structure, crystallinity and average crystallite size. The XRD patterns of the 13, 18 and 24 nm NPs are shown in Fig. 5.22. At first glance, it can be seen that all three samples are crystalline, presenting well distinct diffraction peaks. For the 13 nm NPs, all the observed peaks can be indexed to Fe_3O_4 (black indices). The peaks relating to the other iron oxide phases were not detected. The XRD pattern of the 18 nm NPs is similar to what observed for the 13 nm NPs. However, the peaks become narrower owing to an increased particle crystallite size. Interestingly, no diffraction peaks attributing to FeO were observed in this sample. This is in contradiction to what has been deduced from the SAED line scan analysis. The reason for this inconsistency may be linked to the fact that this sample was measured after 50 days of storage at the ambient conditions. It seems that even aging at the ambient conditions facilitates the oxidation process particularly when the diffusion length is rather short.

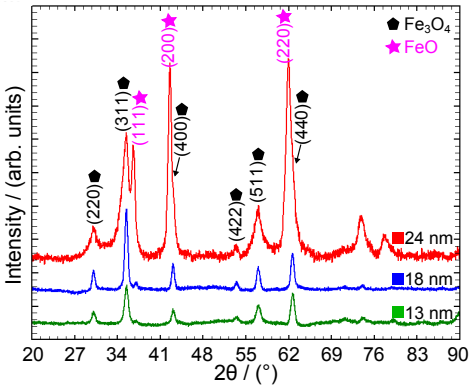

Figure 5.22: Powder X-ray diffraction patterns of 13, 18 and 24 nm NPs [124]. Reproduced by permission of The Royal Society of Chemistry.

The XRD diffraction pattern of the 24 nm NPs differs significantly from the two former samples. In its pattern, in addition to the typical Fe_3O_4 diffraction peaks, the major characteristic peaks of FeO can also be discerned (purple indices). It is noticeable that the $\{311\}_{Fe_3O_4}$ and $\{111\}_{FeO}$ peaks become well separated. The appearance of the well distinct FeO diffraction peaks is a compelling evidence of the formation of crystalline FeO core in the course of nucleation and growth. By considering that this sample was also kept on shelf for a period of time similar to the 18 nm NPs prior to the measurement, we can infer that in the larger particles, the oxidation process becomes substantially retarded due to a longer diffusion pathway.

The particle average crystallite size was estimated from the Scherrer equation given by

$$d = \frac{K\lambda}{\beta \cos(\theta)}, \tag{5.5}$$

with K the shape factor usually assumed to be 0.94, λ the wavelength of the incident Cu $K_{\alpha 1}$ X-ray source, β the full peak width at half the maximum intensity (FWHM) and θ the Bragg angle both in radians.

The Fe_3O_4 and FeO crystallite sizes were calculated by taking the FWHM of the $\{311\}_{Fe_3O_4}$ and $\{111\}_{FeO}$ peaks, respectively. The obtained values are summarized in Table 5.4. The crystal cell parameter of the 13 nm NPs was found to be 8.381 Å by refining its XRD pattern with the Rietveld method (χ^2= 3.36) using the FullProf-Suite software [126]. It is worth highlighting that for the 13 nm pure magnetite NPs, the XRD and TEM results match perfectly. Notably, the estimated values start to diverge as the particle size increases to 18 nm. For the 24 nm NPs, the Fe_3O_4 and FeO crystallite sizes are about 6 and 14.6 nm, respectively, and the overlap between the TEM and XRD results becomes even poorer. These discrepancies can plausibly be attributed to the existence of the strained regions and lattice defects in the biphasic particles as already discussed in section 5.3.1. Diverging between the particle mean core sizes analyzed from XRD and TEM has been observed by Luigjes et al. [127] for 20 nm iron oxide NPs. The correlation between the particle core sizes estimated from different methods is addressed and discussed in the next sections.

5.3.3 Electron energy loss spectroscopy

As discussed in section 3.3.3, EELS is a potent tool for investigation of the electronic structure of different phases of iron oxide. In this study, the EELS experiments were performed on few selected particles during the HRTEM studies. Fig. 5.23(a) shows the EELS spectrum obtained for the 13 nm NPs. The inset depicts the TEM micrograph of the particle on which the EELS experiment was performed. At first glance, the presence of several sharp edges ranging from 530 to 560 eV and 700 to 730 eV can easily be seen. The former ones are attributed to the oxygen K edge and the latter ones to the Fe $L_{2,3}$. The features are superimposed on a rich continuously decreasing background typically characterized by a power law function (cf. section 3.3.3). It can clearly be seen that the oxygen K edge is composed of four distinct peaks annotated with A, B, C and D. In one of the earliest studies, Colliex et al. [128] exploited EELS to distinguish between different Fe-O compounds particularly by resolving the oxygen K and Fe $L_{2,3}$ edges. They found that the oxygen K edge, particularly the A and C bands, changes as the oxidation state switches from FeO to $\gamma - Fe_2O_3$. Also, they showed that the C band does not exist in FeO and $\alpha - Fe_2O_3$. The oxygen K edge recorded for the 13 nm NPs is the characteristic of Fe_3O_4.

Remarkably, in the EELS spectrum of the 18 nm NPs (Fig. 5.23(b)), the C band diminishes almost completely and the A band's intensity relative to the B' one decreases compared to the 13 nm NPs. These phenomena indicate

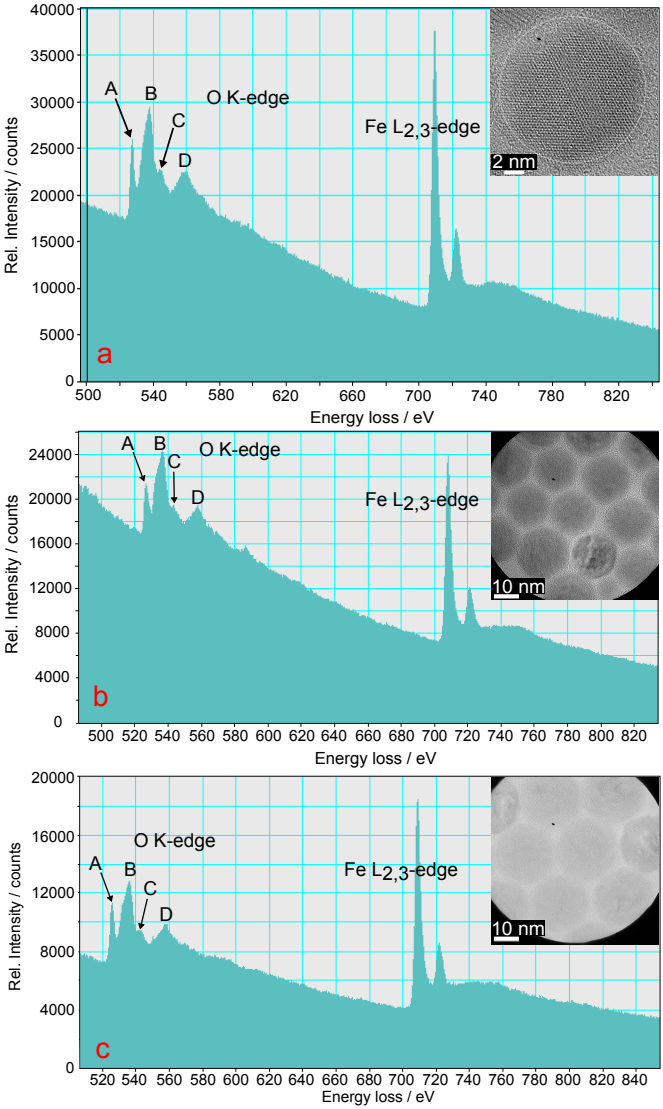

Figure 5.23: EELS spectra of (a) 13 nm, (b) 18 nm and (c) 24 nm nanoparticles presenting both oxygen K and iron $L_{2,3}$ edges. The TEM images of the studied particles are shown in the inset.

the presence of a fraction of FeO in these particles. Colliex et al. [128] showed that for a pure FeO thin film, the A band vanishes nearly and the C one is barely detectable. The 24 nm NPs were treated analogously to the former ones. Fig. 5.23(c) shows the EELS spectrum of these particles taken from few selected particles as shown in the inset. The pattern resembles the one observed for the 18 nm NPs.

From the first view, all three samples show a similar profile at higher energy regimes showing two lines corresponding to L_3 and L_2 at $\approx$ 710 eV and $\approx$ 720 eV, respectively. In the last two decades, there has been an interest to determine the composition of iron oxide compounds by comparing the relative intensity of L_3:L_2 [128, 129]. Recently, Jasinki et al. [130] conducted a series of spatially resolved EELS experiments on iron oxide NPs and compared different quantification methodologies. Broadly speaking, the L_3:L_2 intensity rises from $\approx$ 4.6 to $\approx$ 6.5 as the oxidation state evolves from FeO to $\alpha - Fe_2O_3$ [130]. Qualitatively, by comparing Fe $L_{2,3}$ edge seen in Figs 5.23(a), (b) and (c), it is seen that the L_3:L_2 intensity decreases by growing the particle size from 13 to 24 nm and its consequent phase transformation from pure Fe_3O_4 to a mixture of FeO and Fe_3O_4. Deeper investigations and quantitative analyses of the EELS spectra are beyond the scope of this study.

5.3.4 Mössbauer spectroscopy

To shed a light into the particles' constituent phases, ^{57}Fe Mössbauer (MS) absorption spectroscopy has been employed. Assuming a similar recoil-free fraction of absorption (f-factor) for all phases, their relative quantities are the same as the relative areas under their corresponding subspectra. The shapes of the Mössbauer spectra of Fe_3O_4 and FeO differ significantly [131, 132], enabling one to differentiate their contributions. MS measurements were performed on all three samples at 15 K, 215 K and 295 K (RT). These temperatures were chosen in order to offer a detailed insight into the different magnetic states of the NPs. At 15 K, the magnetic moment fluctuations of the NPs with a diameter of a few nanometer are expected to be much slower than nuclear Larmor precession ($\approx$ GHz). Therefore, relaxational line broadening is negligible. Generally, it is agreed that FeO shows a very complex spectrum at low temperatures which strongly depends on its exact composition [131]. This implies that a reliable analysis of the low temperature spectra, particularly in the studied FeO/Fe_3O_4 NPs where the spectrum is a superposition of different subspectra, is hard to accomplish. Consequently, to elucidate the presence of FeO in these particles, we have also recorded MS spectra at temperatures well above the Néel temperature T_N of FeO ($\approx$ 200 K) which are 215 K and RT. In these spectra, the nonmagnetic contribution of FeO can easily be distinguished from the other Fe compounds which still reveal magnetic hyperfine splitting [124].

The MS spectra of the 13 nm NPs at different temperatures are shown in Fig. 5.24(a). The observed spectra are typical for pure magnetite NPs [132]. At 15 K, the magnetic hyperfine pattern consists of sharp resonance lines, while at higher temperatures lines broaden and the splitting collapses. The spectrum obtained at 15 K was fitted satisfactorily using five magnetic subspectra with the hyperfine parameters corresponding to magnetite NPs [132]. The analyzed

hyperfine parameters are summarized in Table 5.3. For the spectra obtained at 215 K and RT, we had to apply a different fitting strategy using two subspectra corresponding to magnetite A- and B-site and a hyperfine field distribution simulating the relaxation effects. The changes between low and high temperature spectra can be attributed to the Verwey transition, occurring in magnetite at $\approx$ 120 K [133]. These findings are consistent with earlier analysis on magnetite NPs by Dézsi et al. [132]. Notably, the ad hoc introduced hyperfine field distribution provides no physically adequate description of the eventual dynamic line broadening in this temperature range. Nevertheless, it gives sufficient information for an estimate of the hyperfine parameters.

Table 5.3: Analyzed hyperfine parameters of ^{57}Fe Mössbauer spectrum of 13 nm nanoparticles measured at 15 K [124]. Reproduced by permission of The Royal Society of Chemistry.

Component	IS^a (mm/s)	QS^b (mm/s)	$B_{hf}{}^c$ (T)	A^d (%)	w^e (mm/s)
a	0.25	0	50.5	37	0.2
b1	0.39	0	52.7	30	0.23
b2	0.57	0.01	51.0	6.6	0.47
b3	0.85	-0.55	48.9	8	0.30
b4	0.73	1.92	37.0	5	0.15
b5	0.70	0.01	48.8	14	0.37

^{a}isomer shift relative to Fe metal at RT
^{b}quadrupole splitting=$1/2e^2$qQ
^{c}hyperfine magnetic field at ^{57}Fe nuclei
^{d}area corresponding to each spectral component
^{e}line width

The MS spectra of the 18 nm NPs are displayed in Fig. 5.24(b). The low temperature spectrum resembles the one observed for the 13 nm particles yet with an additional broad structure lying below the six lines. This broad feature can be attributed to FeO and an interfacial FeO/Fe_3O_4 phase. Owing to the complexity of FeO's low temperature spectrum, no detailed analysis has been carried out on this spectral component. For an approximate description, we used two hyperfine field distributions with isomer shifts (IS) of $\approx$ 1.14 mm/s (D1) and $\approx$ 0.22 mm/s (D2), being tentatively attributed to FeO and the aforementioned interfacial phase with spectral fractions of 9% and 11%, respectively. The remaining part of the spectrum was fitted utilizing a similar procedure applied for the low temperature spectrum of the 13 nm NPs (cf. Table 5.3). Interestingly, a more collapsed spectrum at 215 K was observed for these particles compared to the 13 nm ones, indicating a smaller anisotropy energy barrier and a smaller superparamagnetic blocking temperature T_B^{sp}.

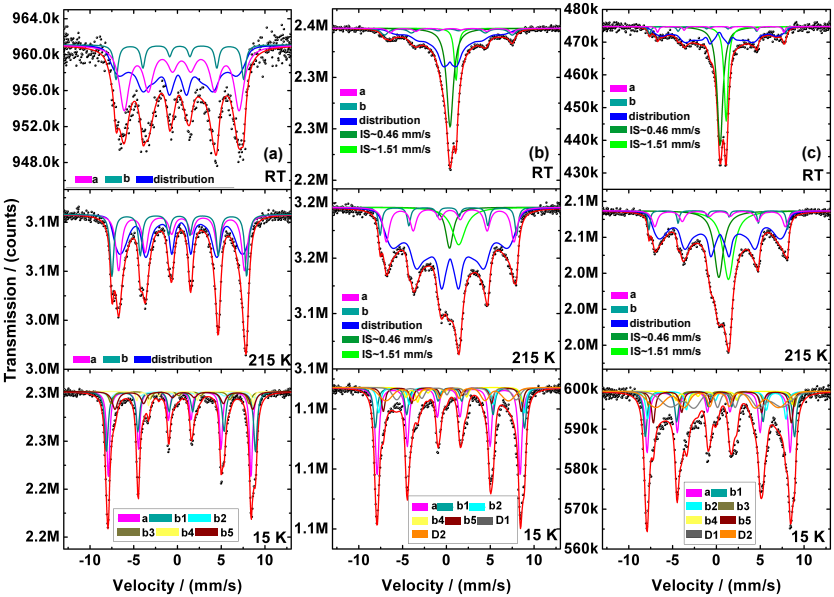

Figure 5.24: Mössbauer spectra of (a) 13 nm (b) 18 nm and (c) 24 nm iron oxide nanoparticles recorded at different temperatures. The solid red lines are least-squares fits of the experimental data to a superposition of different spectral components [124]. Reproduced by permission of The Royal Society of Chemistry.

Another feature of the high temperature spectra is the appearance of a paramagnetic component with an IS of ≈ 1.51 mm/s, characteristic of Fe^{2+} in FeO [131]. The remaining part of the spectrum was fitted using the model applied for the 13 nm NPs with an additional non-magnetic contribution due to the fast fluctuating moments of the superparamagnetic particles with an IS ≈ 0.46 mm/s. At room temperature the spectrum collapses almost completely since now the dominating fraction of the superparamagnetic moments is fluctuating faster than the nuclear Larmor precession frequency. The fraction ofFeO at both 215 K and 295 K is equal to $\approx 8\%$, matching with the value obtained for the 15 K fit. Moreover, the fits support a fractional amount of 11% approximated for the intermediate phase from low temperature fit.

The 24 nm particles were treated analogously to the previous sample and the resulting MS spectra are shown in Fig. 5.24(c). The collapse of the spectra at different temperatures resembles clearly that observed for the 18 nm NPs, indicating a comparable blocking temperature for both samples. The fractions of FeO and the interfacial phase were estimated to be $\approx 18\%$ and $\approx 20\%$, respectively. In summary, the Mössbauer measurements revealed an increased fraction of FeO and the intermediate FeO/Fe_3O_4 phase with increasing particle size [124].

Table 5.4: Volume weighted content (in %) and size of Fe_3O_4 and FeO in FeO/Fe_3O_4 NPs obtained from Mössbauer, XRD and SVD reconstructions.

d_{TEM} [a]	Fe_3O_4	FeO	FeO/Fe_3O_4 [b]	$d^{MS}_{Fe_3O_4}$	$d^{MS}_{FeO/Interm.}$ [c]	$d^{XRD}_{Fe_3O_4(311)}$	$d^{XRD}_{FeO(111)}$	$d^{M-H}_{Fe_3O_4}$ [d]
13	100	-	-	13	-	12.8	-	12.8
18	80	8	12	≈8	≈10	17	-	14.8
24	64	18	20	≈7	≈17	6	14.6	-

[a] Diameters are given in nanometer

[b] FeO/Fe_3O_4 interfacial phase

[c] Volume contents of both FeO and the intermediate phase are taken into calculation

[d] Saturation magnetization values are taken from $M-H$ measurements presented in section 5.3.5

Having assumed that both FeO and Fe_3O_4 phases have a perfect spherical shape located in the centre and on the shell, respectively, we have converted the phase volume fraction approximated from the Mössbauer measurements to its actual diameter. Admittedly, these assumptions are far from the actual phase distribution within a single particle. However, they have only been made to give a dimensional impression. The estimated diameters for Fe_3O_4 and FeO plus the intermediate phase are tabulated in Table 5.4. For the 24 nm sample in which we succeeded in estimating the crystallite size of both phases, there is a good agreement between the crystallite sizes and the phase diameters estimated after applying the conversion method on the Mössbauer results.

5.3.5 Magnetic properties

After performing extensive crystallographic investigations and correlating particle phase composition and crystal structure to its size, it is essential to know how these AFM/FIM NPs behave magnetically. To achieve this goal, the particle magnetization as a function of external magnetic field $M-H$ and temperature $M-T$ were studied. Fig. 5.25(a) shows the $M-H$ curves measured on particle suspensions in toluene at RT. It can clearly be seen that the magnetization in the 13 nm NPs soars to high values at relatively low fields and then grows steadily and reaches the saturation magnetization of $M_s^{13} = 397$ kA m^{-1}. It is noticeable that in the 18 and 24 nm FeO/Fe_3O_4 NPs, M_s drops nearly to half of this value ($M_s^{18} = 177$ kA m^{-1}, $M_s^{24} = 179$ kA m^{-1}). The reduced M_s values can be attributed to the presence of paramagnetic FeO and differently ordered Fe_3O_4 domains. In these biphasic NPs, reaching the saturation magnetization becomes more gradual as the particle size and the volume fraction of FeO increase. This indicates that the FeO/Fe_3O_4 NPs have a smaller magnetic moment, retarding the aligning process.

To gain more detailed information about the magnetic moment distribution $f(m)$ of the particles, we have reconstructed the $M-H$ curves with the Langevin function $L(m,H)$ (cf. Eq. 1.16) using singular value decomposition (SVD) methodology. First, let us to give a brief description about the SVD technique [124].

Singular value decomposition (SVD) methodology

Singular value decomposition (SVD) is a method to find the best fit to original data points. In a sense, it can be considered as a linear least squares fitting method. What SVD does in fact is the breaking of a rectangular matrix A into the product of an orthogonal U, a diagonal S and the transpose of an orthogonal matrix V. This can be expressed by

$$A_{KN} = U_{KK} S_{KN} V^T_{NN}. \tag{5.6}$$

If we consider our problem in which we look to fit the experimentally measured M values with the Langevin function, SVD can be applied to transform the Langevin function into a series of linear equations and eventually build a design matrix A. The particle magnetic moment distribution can be expressed by

$$MV_t =< m >= \sum_i n_i m_i L(\xi_i) \Delta m_i, \tag{5.7}$$

where m is the sample net magnetic moment, n_i is the number density of the particles having m_i and V_t is the total particle volume. All the values should be given in the SI units. Now, if we build the design matrix A for a range of magnetic field amplitude and moment distribution, Eq. 5.7 can be converted into a matrix format and given by

$$\begin{bmatrix} M(H_1) \\ M(H_2) \\ \vdots \\ M(H_K) \end{bmatrix} = A \begin{bmatrix} n_1 m_1 \\ n_2 m_2 \\ \vdots \\ n_N m_N \end{bmatrix} \quad \text{with} \quad A = \begin{bmatrix} A_{11} & A_{12} & \cdots & A_{1N} \\ A_{21} & A_{22} & \cdots & A_{2N} \\ \vdots & \vdots & \ddots & \vdots \\ A_{K1} & A_{K2} & \cdots & A_{KN} \end{bmatrix} \tag{5.8}$$

in which

$$A_{ji} = L(\frac{\mu_0 m_i H_j}{k_B T}) \frac{\Delta m_i}{V_t} \qquad \text{with} \qquad \Delta m_i = m_{i+1} - m_i. \tag{5.9}$$

By applying SVD (Eq. 5.6) to matrix A, Eq. 5.8 can be rewritten as

$$\begin{bmatrix} M(H_1) \\ M(H_2) \\ \vdots \\ M(H_K) \end{bmatrix} = U \begin{bmatrix} S_1 & 0 & \cdots & 0 & 0 & \cdots & 0 \\ 0 & S_2 & \cdots & 0 & 0 & \cdots & 0 \\ \vdots & \vdots & \ddots & \vdots & \vdots & \cdots & \vdots \\ 0 & 0 & \cdots & S_N & 0 & \cdots & 0 \end{bmatrix} V^T \begin{bmatrix} n_1 m_1 \\ n_2 m_2 \\ \vdots \\ n_N m_N \end{bmatrix} \tag{5.10}$$

The S_i are the singular values, representing the number density of each unknown vector of $n_i m_i$. To avoid the inclusion of the experimental errors into the calculation, one has to set a threshold S_{min} and set the S_i components to 0 if $S_i < S_{min}$. Ultimately, the $n_i m_i$ vector can be expressed by

$$\begin{bmatrix} M(H_1) \\ M(H_2) \\ \vdots \\ M(H_K) \end{bmatrix} = U \begin{bmatrix} S_1 & 0 & \cdots & 0 & 0 & \cdots & 0 \\ 0 & S_2 & \cdots & 0 & 0 & \cdots & 0 \\ \vdots & \vdots & \ddots & \vdots & \vdots & \cdots & \vdots \\ 0 & 0 & \cdots & S_{N'} & 0 & \cdots & 0 \\ \vdots & \vdots & \cdots & \vdots & \vdots & \cdots & \vdots \\ 0 & 0 & \cdots & 0 & 0 & \cdots & 0 \end{bmatrix} V^T \begin{bmatrix} \widetilde{n}_1 m_1 \\ \widetilde{n}_2 m_2 \\ \vdots \\ \widetilde{n}_N m_N \end{bmatrix} \quad (5.11)$$

$$\begin{bmatrix} \widetilde{n}_1 m_1 \\ \widetilde{n}_2 m_2 \\ \vdots \\ \widetilde{n}_N m_N \end{bmatrix} = V \begin{bmatrix} 1/S_1 & 0 & \cdots & 0 & 0 & \cdots & 0 \\ 0 & 1/S_2 & \cdots & 0 & 0 & \cdots & 0 \\ \vdots & \vdots & \ddots & \vdots & \vdots & \cdots & \vdots \\ 0 & 0 & \cdots & 1/S_{N'} & 0 & \cdots & 0 \\ \vdots & \vdots & \cdots & \vdots & \vdots & \cdots & \vdots \\ 0 & 0 & \cdots & 0 & 0 & \cdots & 0 \end{bmatrix} U^T \begin{bmatrix} M(H_1) \\ M(H_2) \\ \vdots \\ M(H_K) \end{bmatrix} \quad (5.12)$$

In each SVD reconstruction, four initial parameters have to be taken: m_{min}, m_{max}, Δm_i and S_{min}. Since the moment distribution is estimated using the nonlinear region of the $M - H$ curves, m_{min} and m_{max} can initially be approximated from the following relations:

$$\frac{\mu_0 m_{min} H_{max}}{k_B T} = 1 \quad \text{and} \quad \frac{\mu_0 m_{max} H_{min}}{k_B T} = 1 \quad (5.13)$$

The SVD method has already been applied to reconstruct the $M - H$ curves of magnetic ferrofluids by Berkov et al. [134]. They have shown its capability for the estimation of the particle core size distribution.

The fits for all three samples (solid lines) are plotted in Fig. 5.25(a). Clearly, there is a good agreement between the measured and reconstructed curves for all the samples. Fig. 5.25(b) depicts the number density magnetic moment distribution. A uniform magnetic moment distribution was obtained for the 13 nm NPs, giving a mean core diameter of 12.8 nm. A peak seen at around 4×10^{-21} A m^2 is somehow an artifact, appearing due to yet increasing M

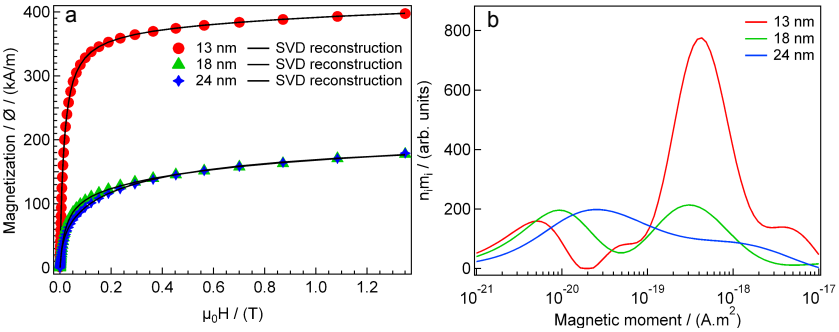

Figure 5.25: (a) Experimentally measured (markers) and simulated (solid lines) $M-H$ magnetization curves of the three samples suspended in toluene measured at RT and (b) particle magnetic moment distributions obtained from the SVD reconstruction [124]. Reproduced by permission of The Royal Society of Chemistry.

values even at high fields. This effect has been observed by Yoshida et al. [135]. Noticeably, a broad moment distribution was found for the FeO/Fe_3O_4 NPs. Depending on particle size and capping density of oleic acid, the particles experience different oxidation paces, implying that dimension and quality of Fe_3O_4 phase vary from one particle to another. This can explain the observed wide moment distribution in these biphasic particles. It is worth noting that the estimated core size from TEM, XRD and $M-H$ measurements matches well for the 13 nm pure magnetite NPs. Conversely, the estimated values diverge as the particle size and the fraction of FeO enlarge. This phenomenon has already been shown by Luigjes et al.[127] for spherical iron oxide NPs synthesized via decomposition of iron-oleate [124].

Field and zero field cooled magnetizations

The zero field cooled (ZFC) $M-H$ hysteresis loops of the immobile samples taken at 5 K are shown in Fig. 5.26(a). The immobile particles show a magnetic behavior comparable to that observed in the liquid samples. Note that the existence of the AFM FeO phase along with the Fe_3O_4 surface anisotropy can explain the fact that saturation is not reached at 5 K. To examine the existence of the EB energy at the FeO/Fe_3O_4 interface, the immobile samples were cooled from RT to 5 K in 5 T and then the $M-H$ hysteresis loops were recorded. The measured field cooled (FC) $M-H$ curves and their corresponding ZFC ones are plotted in Fig. 5.26(b)-(d). The EB coupling is characterized by a shift in the hysteresis loop, caused by the ferromagnetic coupling of the magnetite spins to the uncompensated interfacial spins of FeO. The 13 nm NPs reveal similar symmetric and not shifted FC and ZFC magnetization curves, implying that no EB coupling exist in this case. Conclusively, there is no FeO phase in these particles as already deduced from the Mössbauer results. The ZFC and FC magnetizations recorded at different temperatures are presented in Fig. 1 in the Appendix A.

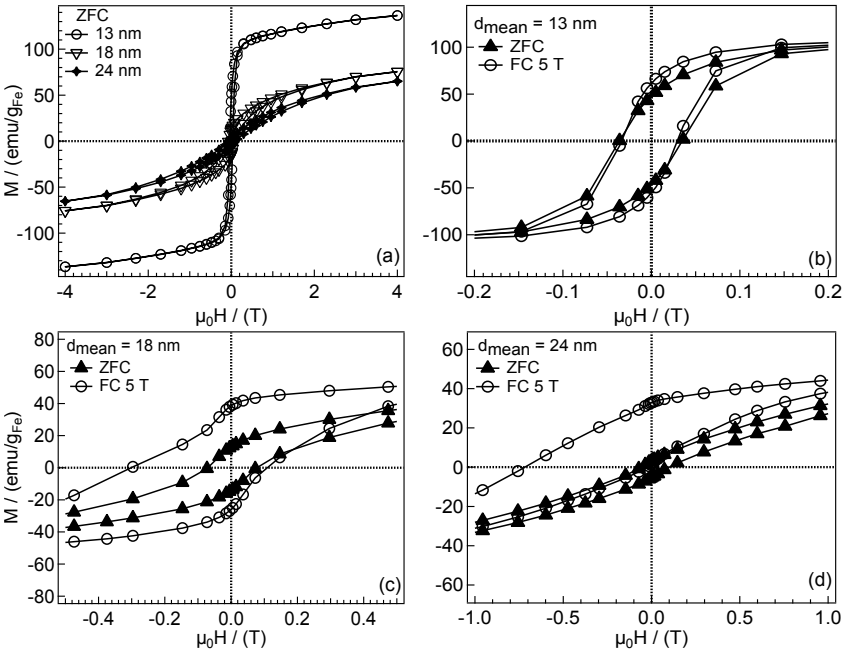

Figure 5.26: (a) ZFC $M-H$ magnetizations of all three samples and (b-d) comparison of the ZFC and FC $M-H$ magnetizations measured at 5 K in 5 T [124]. Reproduced by permission of The Royal Society of Chemistry.

The magnetization of the FeO/Fe_3O_4 NPs differs significantly from magnetite. Some interesting features can be identified at first glance by looking at Fig. 5.26(c) and (d). The first one is the presence of a large EB energy in the FC curves compared to the corresponding ZFC ones for both 18 and 24 nm NPs. At RT, the spin configuration in FeO is paramagnetic and by cooling the particles below the T_N of FeO, the spins orient antiferromagnetically. However, a part of the interfacial spins remains uncompensated which pin the magnetite spins towards the cooling field. The temperature evolution of exchange H_E and coercive H_C fields, given by Eqs. 1.5 and 1.13, for all three samples are plotted in Fig. 5.27(a)-(c). The H^+ and H^- are taken from the hysteresis loops shown in Fig. 5.26. By looking at Fig. 5.27(a), it can be seen that the 13 nm purely magnetite particles show virtually no exchange field, whereas the H_E in the FeO/Fe_3O_4 NPs remains noticeable up to ≈ 200 K, T_N of FeO, and vanishes completely at higher temperatures [124].

The 24 nm NPs reveal a significantly larger H_E compared to the 18 nm ones. This phenomenon is attributed to a stronger pinning of the Fe_3O_4 to FeO spins in the former particles due to their larger FeO volume fraction. The coercivity in the FC case (Fig. 5.27(b)) shows a dropping trend with temperature likewise to what seen for the H_E. The 18 and 24 nm NPs depict a large H_C compared to a

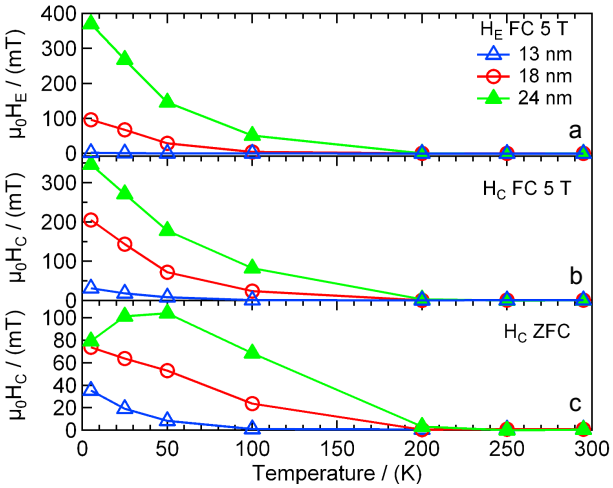

Figure 5.27: (a) Temperature dependence of exchange H_E and coercivity H_C fields in (b) FC and (c) ZFC magnetizations for all three samples. The solid lines are guides to the eye [124]. Reproduced by permission of The Royal Society of Chemistry.

small one observed for the 13 nm ones. This observation can be linked to a large unidirectional anisotropy induced by the uncompensated spins at the AFM/FIM interface, coinciding with the hysteresis loops vertical shift [133]. As the volume fraction of the intermediate phase and FeO grows, the number of uncompensated spins increases and this effect becomes stronger. Interestingly, the H_C increases by nearly a factor of four in the FC case ($\mu_0 H_C = 346$ mT) compared to the ZFC ($\mu_0 H_C = 79$ mT) at 5 K for the 24 nm NPs. The difference between the H_C in the FC and ZFC becomes less pronounced in the 18 nm NPs where the fractions of FeO and the intermediate FeO/Fe_3O_4 phase are smaller.

Another remarkable feature of the FC magnetization curve of the FeO/Fe_3O_4 NPs is its distorted symmetry. The magnetization antiparallel to the cooling field (i.e. magnetization reversal) shows a totally different shape compared to the magnetization parallel to the cooling field. This is easily recognizable for the 24 nm NPs in Fig. 5.26(d). This difference is attributed to the different dominating magnetization mechanisms which arise depending upon the direction of the applied field [136]. In the magnetization reversal process in which the field is exerted antiparallel to the cooling field, the Fe_3O_4 pinned spins should not only overcome their own anisotropy energy barrier, but also the EB anisotropy of FeO to reorient. Therefore at a certain field (e.g. ≈ 60 mT for the 18 nm NPs), the magnetostatic energy becomes so large that the magnetization via the nucleation and propagation of domain walls is energetically favorable to the coherent spin rotation. This phenomenon explains a break in the symmetry of the FC magnetization reversal of these NPs (see Figs. 5.26(c) and (d)). The FC and ZFC magnetization branches show a similar shape which is a compelling evidence of the domination of coherent spin rotation mechanism. Notably,

the field whereby the magnetization reversal starts to behave asymmetrically switches to lower field values as the particle size, literally the FeO size, enlarges. This asymmetric magnetization diminishes at a temperature between 50 and 100 K (see Fig. 2 and 3 in the Appendix A) where the thermal energy becomes comparable with the anisotropy energy [124].

An anomalous vertical shift towards higher M values is noticeable in the FeO/Fe_3O_4 NPs. This shift is an indication of the presence of the EB coupling at the AFM/FIM FeO/Fe_3O_4 interface and also the uncompensated interfacial spins [133]. A noticeable shift is observed in the 24 nm NPs which becomes less prominent by decreasing the particle size. By taking the Mössbauer findings into consideration, it is deduced that the enlargement of the vertical shift coincides with increasing the fraction of FeO and the interfacial FeO/Fe_3O_4 phase as the particle enlarges.

Magnetization measurements as a function of temperature under both ZFC and FC conditions were conducted in a field of 1 mT and the results are plotted in Fig. 5.28. The magnetic moment of the 13 nm NPs shows a hump shaped rise between 5 K and 120 K, followed by an abrupt increase which eventually peaks at the blocking temperature of $T_B^{sp} = 260$ K. In the low temperature regime, a kink existing at ≈ 110 K is presumably attributed to the Verwey transition of magnetite. This observation indicates the crystal perfection of these small NPs as perceived from the HRTEM studies too. The relatively high blocking temperature estimated for these particles, matching well with the Mössbauer findings, can be related to the dipolar interactions between the particles due to their proximity in the powder state and their bulk like magnetization. The FeO/Fe_3O_4 NPs behave differently. For the 18 nm NPs, the magnetic moment grows steadily up to 150 K where it starts to soar and finally peaks at the blocking temperature $T_B^{sp} = 210$ K. A slight shoulder at ≈ 110 K may be linked to the Verwey transition, yet appearing in these particles since the magnetite shell is comparatively thick and crystallized (refer to Figs. 5.19(a) and (d)). Conversely, for the 24 nm NPs, the magnetic moment remains nearly zero and then launches to rise at 180 K, matching with the T_N of FeO. This phenomenon is associated with the transition from AFM to paramagnetic spin configuration in FeO at T_N. Ultimately, the magnetic moment reaches a peak at the blocking temperature $T_B^{sp} = 260$ K. It seems that the effective anisotropy energy in the FeO/Fe_3O_4 NPs (i.e. proportional to the blocking temperature) is a summation of the anisotropy of Fe_3O_4 and the exchange anisotropy of FeO and the intermediate phase. Therefore, a lower blocking temperature estimated for the 18 nm NPs than the 24 nm ones can be related to their smaller fraction of FeO and the intermediate phase [124].

5.4 Characterization of biphasic particles after oxidation

As mentioned earlier, FeO is the most thermodynamically unstable phase of iron oxide and thereby prone to oxidation. Understanding the oxidation process in the FeO/Fe_3O_4 NPs and its effect on the particle phase composition and magnetic properties led us to store the as-synthesized 24 nm NPs, discussed

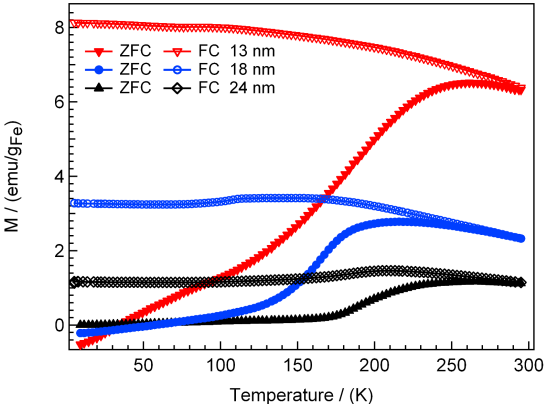

Figure 5.28: ZFC and FC temperature dependent magnetizations performed on the immobile particles in a magnetic field of 1 mT [124]. Reproduced by permission of The Royal Society of Chemistry.

in the previous section, at the ambient conditions for a couple of months and then characterize the changes in their composition and magnetization using Mössbauer spectroscopy and FC and ZFC magnetization measurements.

5.4.1 Mössbauer spectroscopy

In section 5.3.4, we have shown the as-synthesized 24 nm FeO/Fe_3O_4 NPs are composed of 18% and 20% of FeO and the intermediate phase, respectively. In this part, we present the MS measurements performed on the 24 nm sample after 67 days of aging. Note that to approximate the trend of the oxidation assisted phase transformation in these biphasic particles, it is adequate to perform the Mössbauer measurement at RT. The recorded spectrum is displayed in Fig. 5.29(b). The spectrum was fitted using the methodology applied for the fresh samples (cf. section 5.3.4). The hyperfine field values are given in Table 5.3. For comparison, the MS spectrum of the as-synthesized sample is shown in Fig. 5.29(a). At first glance, it can be seen that two spectra are different. A clear feature appearing in the spectrum of the aged sample is the presence of the magnetic six lines at RT. In the freshly synthesized sample, the splitting already collapses at this temperature range. From the fits, we have found out the spectral fraction of FeO shrinks to 14% after this period of storing. Clearly, the aged particles have a blocking temperature T_B^{sp} higher than RT. The rise in the blocking temperature T_B^{sp} is due to the presence of a larger volume fraction of Fe_3O_4 in the aged sample.

5.4.2 Field and zero field cooled magnetization studies

To elucidate how the spontaneous oxidation and transformation of FeO to Fe_3O_4 affect the magnetic properties of the biphasic NPs, the 24 nm particles were characterized magnetically likewise to the as-synthesized ones after being stored

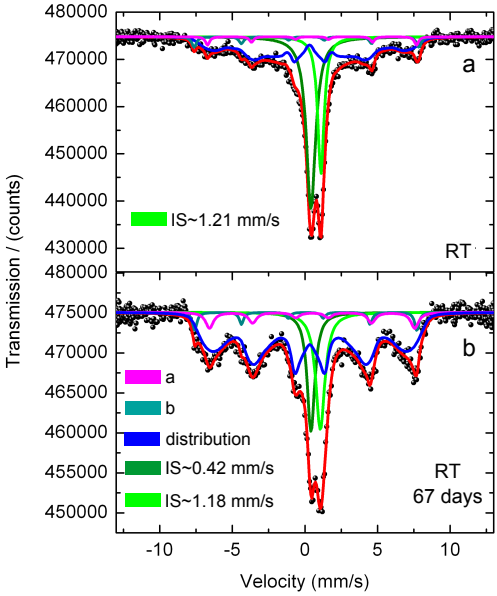

Figure 5.29: Room temperature Mössbauer spectra of (a) as-synthesized 24 nm FeO/Fe_3O_4 NPs and (b) aged at ambient conditions for 67 days. The solid red lines are least-squares fits of the experimental data to a superposition of different spectral components.

on shelf for 120 days. Fig. 5.30(a) depicts the ZFC and FC $M-H$ hysteresis loops measured on the immobile aged sample at 5 K in a cooling magnetic field of 5 T. The results obtained for the as-synthesized 24 nm (Fig. 5.30(b)) are shown here again for comparison. Interestingly, the ZFC loops show a similar trend prior and after aging whereas the FC ones change considerably. Qualitatively, it can unambiguously be seen that the FC hysteresis loops of the aged sample shift towards positive field and negative M values, implying its smaller exchange bias (EB) energy. This is an indication of a shrunk volume of FeO and FeO/Fe_3O_4 intermediate phase in the stored sample compared to its fresh state.

The change in EB energy can quantitatively be identified by comparing the temperature dependence evolution of exchange H_E and coercive H_C fields prior and after aging. The H_E and H_C were calculated using Eqs. 1.5 and 1.13, respectively, and the results for both fresh and aged particles are plotted in Fig. 5.31(a)-(c). Notably, after aging and oxidation of FeO to Fe_3O_4 both exchange and coercive fields decrease. For instance, by looking at Fig. 5.31(a), it is calculated that the H_E at 5 K drops from 370 mT to 193 mT after storing for the designated time. In coincidence with the Mössbauer findings, the magnetization results suggest the occurrence of a gradual growth of Fe_3O_4 from the surface towards the inner FeO core simply by storing.

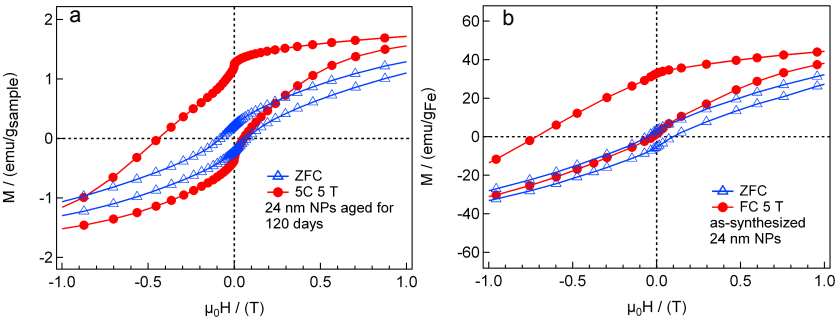

Figure 5.30: ZFC and FC $M-H$ hysteresis loops of (a) 24 nm nanoparticles aged for 120 days at ambient conditions and (b) as-synthesized 24 nm nanoparticles taken at 5 K. The FC measurements were performed in a cooling magnetic field of 5 T.

Another remarkable feature is that the decay rate of both H_E and H_C becomes retarded in the aged sample where the volume fraction of Fe_3O_4 grows. The temperature dependence magnetic behavior of these FeO/Fe_3O_4 NPs is determined by a competition between the exchange anisotropy of FeO and the magnetocrystalline anisotropy of Fe_3O_4. It appears that the anisotropy energy and thermal stability of Fe_3O_4 grow as its thickness enlarges in the aged particles. This can explain the shallower decay observed in the aged particles. At temperatures above 200 K, these nanoparticles reveal a factor of two higher ZFC coercive field compared to the as-synthesized ones as can be seen in Fig. 5.31(c). It can be concluded that the FeO/Fe_3O_4 NPs tend to switch from superparamagnetic to ferro(i)magnetic by further aging and the formation of a thicker Fe_3O_4 shell.

Fig. 5.32 shows the temperature dependent FC and ZFC magnetization results of the as-prepared 24 nm NPs and the sample stored for 120 days on shelf. Interestingly, the shoulder attributed to the Verwey transition in magnetite at $\approx$ 110-120 K in the ZFC branch becomes visible in the aged sample. This observation is a compelling evidence of the conversion of FeO to Fe_3O_4 via aging. Remarkably, in the stored sample, the major rise in the magnetic moment occurs at the Néel temperature T_N of FeO. Notably, the superparamagnetic blocking temperature T_B^{sp} of the aged sample is above the measurement window and apparently higher than the one estimated for the as-formed one ($T_B^{sp} = 260$ K). This finding coincides with the Mössbauer results. It appears that the particle blocking temperature depends strongly on the volume fractions of Fe_3O_4 to FeO.

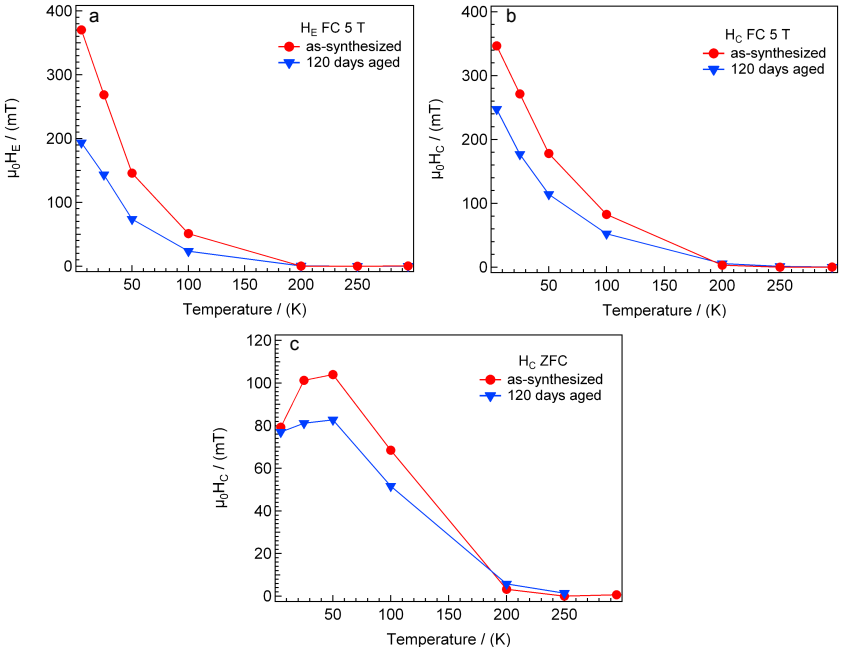

Figure 5.31: (a) Temperature dependence of exchange H_E and coercive H_C fields in (b) FC and (c) ZFC magnetizations for as-synthesized and 120 days aged 24 nm nanoparticles. The solid lines are guides to the eye.

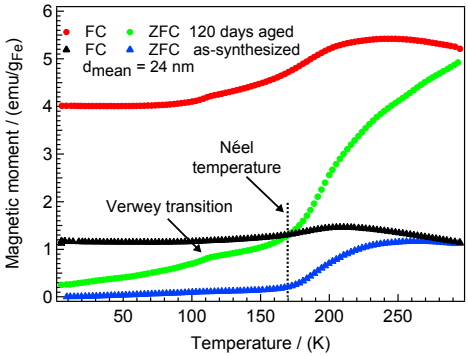

Figure 5.32: ZFC and FC temperature dependent magnetizations carried out on as-synthesized and 120 days aged 24 nm nanoparticles.

5.5 Characterization of PEGylated nanoparticles

5.5.1 synthesis of PEG derivative compounds

To conjugate PEG moieties to the particles, nitrodopamine with high binding affinity to the interfacial iron atoms was chosen as an anchoring group [74]. The synthesis procedure of both nitrodopamine and the conjugated HO-PEG-nitrodopamine are described in sections 4.6.1 and 4.6.2. The success of the nitrodopamine synthesis reaction of as well as its conjugation to HO-PEG compounds were proven by ^{1}H NMR and IR spectroscopy.

NMR and IR spectroscopy

Fig. 5.33 presents the NMR spectra obtained for nitrodopamine and HO-PEG-nitrodopamine. In the nitrodopamine spectrum, the peaks corresponding to the aromatic ring protons can be seen at 7.63 (d) and 6.90 ppm (c). The peaks appearing at 3.32 (a) and 3.23 ppm (b) can be assigned to the methylene groups. The results match well with the previous findings by Malisova et al. [119]. The NMR spectrum of HO-PEG-nitrodopamine is more complex. The peaks related to the nitrodopamine ring protons (g and f) can be identified at 7.60 and 6.93 ppm. The peak at 3.90 ppm (c) can be attributed to the protons of the methylene groups (O-CH_2-(C=O)NH-) [119]. The PEG chain methylene groups (a and b) overlap with those corresponding to nitrodopamine and yet can be observed at 4.06 to 3.24 ppm. On the whole, the occurrence of an amide bond between nitrodopamine and PEG moieties can be concluded [137].

Fig. 5.34 depicts the IR spectrum of HO-PEG-nitrodopamine. A band appearing at 1530 cm^{-1} can be attributed to NH deformation vibration in secondary amides [138]. Another absorption band seen at 1665 cm^{-1} can be related to the C=O stretching vibration of secondary amides. Besides, the absorption band at 1720 cm^{-1} may be an indication of a slight remaining trace of unreacted NHS-PEG. Additionally, the absorption bands appearing at 1050-1200 cm^{-1} are ascribed to C-O-C stretching vibration of PEG chains [79, 137, 138].

5.5.2 Surface properties of oleic acid capped particles

Particle stability

To probe the stability of oleic acid coated particles and gain an impression about their shelf life time, the PCCS measurements were carried out on two batches of hydrophobic OA coated particle suspensions with a mean core diameter of 12 and 24 nm after being stored at 4°C for 365 and 155 days, respectively. The particle concentration of the stored samples is $\approx$ 1 mg/mL. The samples with two completely different magnetic core diameters were chosen to examine the impact of the dipole-dipole interactions on particle agglomeration.

Fig. 5.35 shows the temporal change in the particle hydrodynamic size. It is obvious that even a year of aging has a marginal effect on the dispersion state of the 12 nm. For the 24 nm NPs, the hydrodynamic size increases slightly after

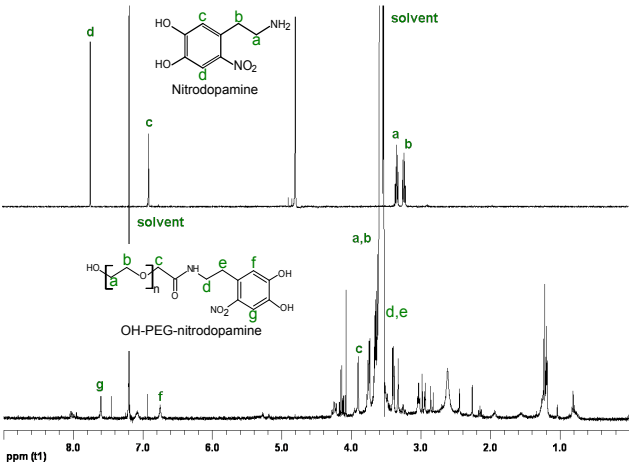

Figure 5.33: ^{1}H NMR spectra of nitrodopamine (400 MHz, D_2O, δ) and HO-PEG-nitrodopamine (400 MHz, $CDCl_3$, δ). The spectra were calibrated with respect to the solvent signal [137]. Reproduced by permission of The Royal Society of Chemistry.

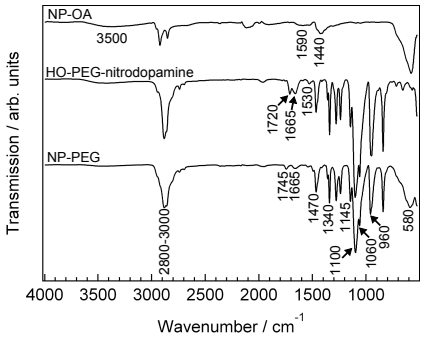

Figure 5.34: IR spectra of NP-OA, HO-PEG-nitrodopamine and NP-PEG [137]. Reproduced by permission of The Royal Society of Chemistry.

155 days. This change is in the range of the measurement error and cannot be attributed to coupling of two individual nanoparticles and the eventual formation of dimers.

Capping density of oleic acid molecules

Before performing the ligand exchange reaction, it is important to have an estimate of the number of bound OA molecules to particles and its dependence on particle core size. TGA experiments (refer to section 3.1.3) were carried out on dried NP-OA particles with a mean core size of 12 and 22 nm and the results

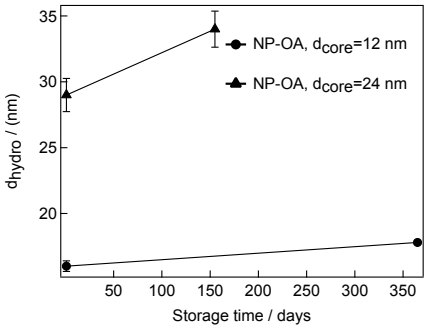

Figure 5.35: Change in the particle hydrodynamic size after storing at 4°C for 365 and 155 days as measured with PCCS. The sample particle concentration is ≈ 1 mg/mL.

are depicted in Fig. 5.36(a). Additionally, a differential scanning calorimetry (DSC) experiment was performed on a 12 nm NP-OA to elucidate the desorption pathways of OA molecules. The DSC graph is shown in Fig. 5.36(b).

Three distinct endothermic peaks can be observed in the DSC graph. The first peak appearing at ≈ 100°C can be ascribed to the desorption of absorbed and structural water as well as absorbed impurities. However, the peak intensity is rather low, indicating the presence of very low amount of water and impurities in the SPIONs. This can also be confirmed by seeing nearly no weight loss until 100°C in the TGA plots. The second peaks being observed around ≈ 235°C may be attributed to the dissociation of those OA molecules with a weaker binding strength, presumably bound via bidentate or unidentate coordination modes. Evidently, the removal of this type of OA molecules triggers a small weight loss step (so-called 1^{st} weight loss, cf. Table 5.5), pointing out that only a few percent of OA molecules are bound weakly. The last peak seen at ≈ 390°C can be linked to the dissociation of OA molecules plausibly bound via bridging coordination mode to the particles which apparently demand higher thermal energy to be released. The main dissociation temperatures and their corresponding weight losses extracted from TGA and DSC graphs are summarized in Table 5.5. The number of OA molecules covered a single nanoparticle was estimated using Eq. 3.1. Eventually, the head area of a single OA molecule a was estimated and listed in Table 5.5. Remarkably, the values estimated for 12 and 22 nm particles agree well. This indicates that the formation of a single OA layer on particles is independent of their core size.

5.5.3 Ligand exchange scheme

To pull the hydrophobic NP-OA nanoparticles into water, PEG moieties were grafted to the particles via a mild reaction at RT (cf. section 4.6.3). The process is illustrated schematically in Fig. 5.37. The success and applicability of the phase transfer reaction have been examined for a broad range of particle sizes. In this study, one of our goals is to design functional NPs for homogeneous magnetic bioassays. To conduct a successful magnetic bioassay via the manipulation of

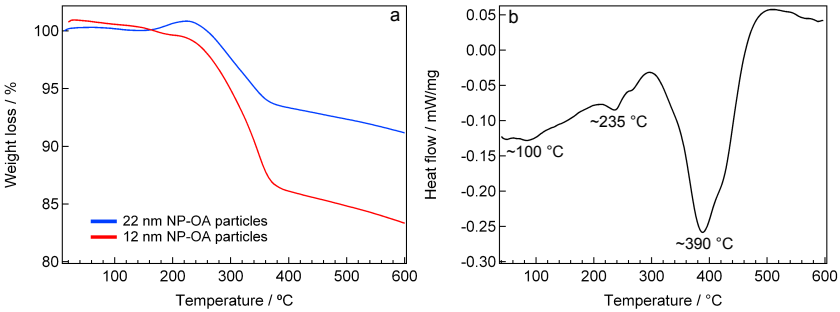

Figure 5.36: (a) TGA plots of 12 and 22 nm NP-OA particles carried out under a flow of nitrogen and oxygen, (b) typical DSC test performed on 12 nm NP-OA.

Table 5.5: TGA and DSC results of 12 and 22 nm NP-OA.

Core size	TGA					DSC
	1st weight loss (%)	2nd weight loss (%)	Total weight loss[a] (%)	No. OA molecules[b]	Head area of OA (Å^2)	Dissociation peak (°C)
12	1.29	15.8	17.09	2059	4.68	≈ 235-260
22	0.3	9.6	9.9	6764	4.7	≈ 390

[a]Measured between 25 and 600°C

[b]Estimated by employing Eq. 3.1 and it is the number of OA molecules per single particle.

the particles using the RMF setup, the particles relaxing via the Brownian mechanism ($d_c > \approx 22$ nm) are required (cf. Fig. 1.11). This topic is addressed in section 5.6.1. Therefore, we have further investigated the properties of 24 nm NPs.

Capping density of PEG moieties

The amounts of the capping molecules prior and after the ligand exchange were assessed by TGA. The weight losses of NP-OA and NP-PEG particles as a function of temperature are plotted in Fig. 5.38. The total weight of OA molecules pyrolysed between 25°C and 600°C is ≈ 26% and happens in two distinct steps. The first weight loss occurs between 180°C and 270°C which is followed by the second step terminating at 390°C. The amount of the OA molecules per gram of particles was calculated to be ≈ 1.2 mmol [137]. It appears that OA molecules are pyrolysed in two temperature regimes as previously discussed in section 5.5.2.

After the PEGylation, the total weight loss percentage increases substantially. The ligand exchange reaction was performed at two PEG:NPs mass ratios to study the impact of available PEG molecules on their packing density. The total weight loss of PEG groups on the NP-PEG particles stabilized with 28 (△) and

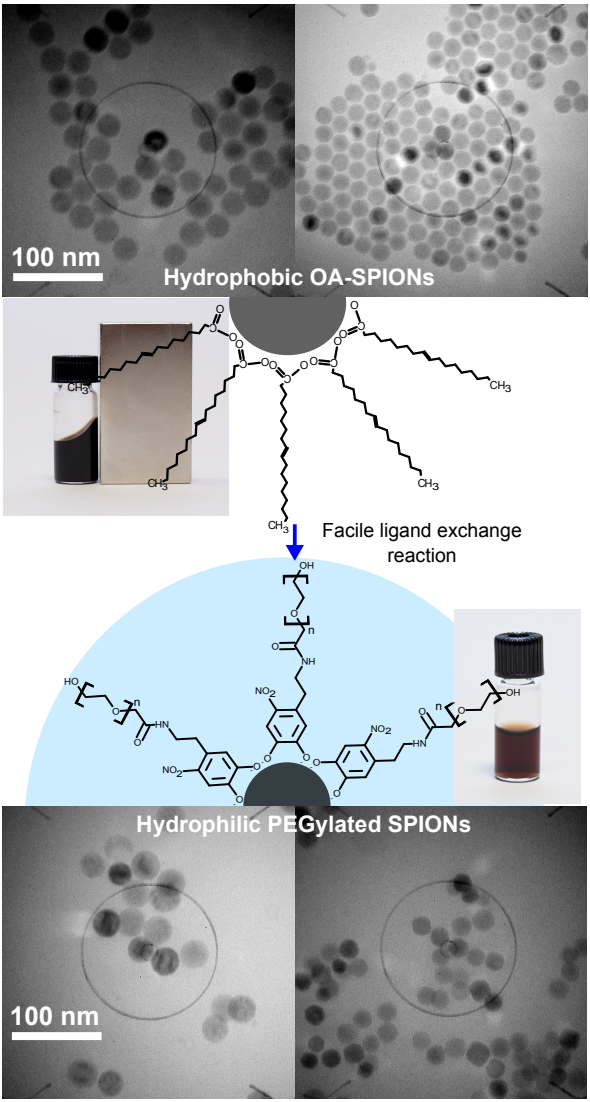

Figure 5.37: Schematic depiction of the phase transfer strategy via exchanging OA molecules with hydrophilic HO-PEG-nitrodopamine groups. Typical TEM micrographs of 24 and 18 nm prior and after PEGylation are shown.

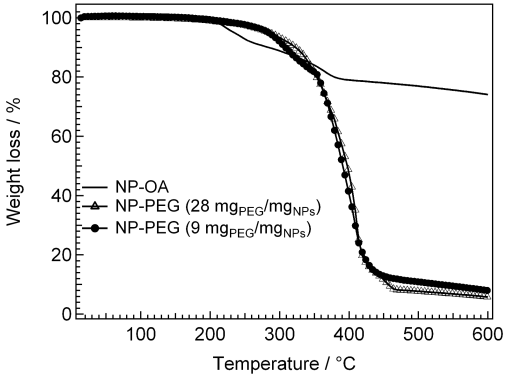

Figure 5.38: TGA results obtained for NP-OA (-) and NP-PEG stabilized with 28 (△) and 9 (•) mg_{PEG}/mg_{NPs}. The particle core size is 24 nm [137]. Reproduced by permission of The Royal Society of Chemistry.

9 (•) mg_{PEG}/mg_{NPs} are 92% to 66% and 88% to 62%, respectively. The bigger and smaller values were obtained respectively by assuming that either all OA molecules have been removed completely or have been remained fully on the particle after the PEGylation. Since the temperature ranges in which OA and PEG molecules are pyrolysed are unresolved, only a weight loss range can be given.

Interestingly, the weight percentage of the capped PEG groups is virtually independent of the PEG:NPs mass ratio chosen for the exchange reaction. This indicates that solely a single PEG layer encapsulates the particles regardless of the amount of PEG groups added to the reaction. The weight loss percentages measured between 25°C and 600°C, for the scenario that all OA molecules remained bound to the particles, were converted into the number of PEG per particle surface area provided that the particles are spherical with density of 5.18 g cm^{-3}. The number of PEG per square nanometer of the particle surface was estimated to be 1-1.5 PEG nm^{-2} for both mass ratios [137]. This finding is in a good agreement with the packing density previously approximated for PEG derivative dispersants [74, 79].

Particle hydrodynamic size distribution and stability

The hydrodynamic size number distribution of NP-OA and NP-PEG was measured by PCCS as plotted in Fig. 5.39(a). The NP-OA particles reveal a narrow size distribution with a mean size of 30±3.5 nm. No trace of clustering was detected. Knowing that the mean core size is 24 nm and the length of an OA molecule is 2-2.5 nm [78], it can be assumed that the particles are covered with a mono layer of OA molecules. After the PEGylation and suspending in water, the particle hydrodynamic size grew to 60±8 nm. This observation coincides well with respectively ≈ 30 nm and ≈ 40 nm enlargement in hydrodynamic size after conjugating PEG moieties with a molecular weight of 5 and 3 kDa reported previously [74, 78, 79]. The stability of the NP-PEG suspensions in

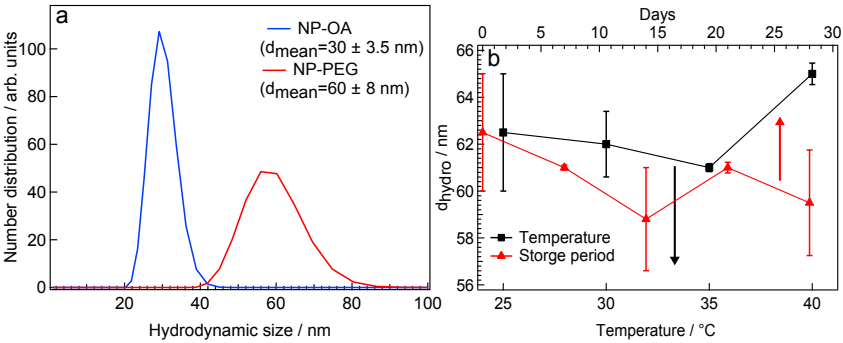

Figure 5.39: (a) Number weighted hydrodynamic sizes of NP-OA and NP-PEG particles and (b) temporal and temperature dependent change in hydrodynamic size of NP-PEG particles [137]. Reproduced by permission of The Royal Society of Chemistry.

water against temperature and storage time was monitored by PCCS and the results are plotted in Fig. 5.39(b). The measurement conditions are described in section 3.4.1. As can be seen, no remarkable change in the hydrodynamic size was observed after a month of storage. Besides, the particles show an exceptional stability against temperature up to 40°C [137].

Static and dynamic magnetic properties

The impact of the PEGylation on the particle static and dynamic magnetic properties was investigated using a MPMS-XL (Quantum Design) magnetometer and an ACS setup [113]. The recorded $M-H$ curves are plotted in Fig. 5.40(a). The saturation magnetizations M_s values are 240 and 234 kA m^{-1} for NP-OA and NP-PEG samples, respectively. The findings indicate that the PEGylation has a negligible influence on the particle static magnetization. The particle response to dynamic magnetic fields changes remarkably after the PEGylation. ACS measurements were performed on particle suspensions at a magnetic field amplitude of 95 μT from 1 Hz to 0.6 MHz. The recorded real and imaginary parts are displayed in Fig. 5.40(b). Note that in ACS both Néel and Brownian relaxation mechanisms contribute and the quickest one dominates. The Brownian peaks of NP-OA and NP-PEG particles are at 20 kHz and 5 kHz, respectively. The observed shift towards lower frequencies after the PEGylation agrees with 30 nm enlargement in the particle hydrodynamic diameter measured by PCCS. The Néel-relaxation-dominated particles produce a constant real part signal for frequencies smaller than their characteristic relaxation frequencies and thus the drop seen in the real part is solely related to the Brownian-relaxation-dominated particles. Accordingly, we can estimate the Néel particles' fraction k introduced by Yoshida et al.[139] by calculating the percentage that the real part signal drops within the measurement frequency range. The fraction of the Néel particles was found to be k=6.6% for both NP-OA and NP-PEG samples [137].

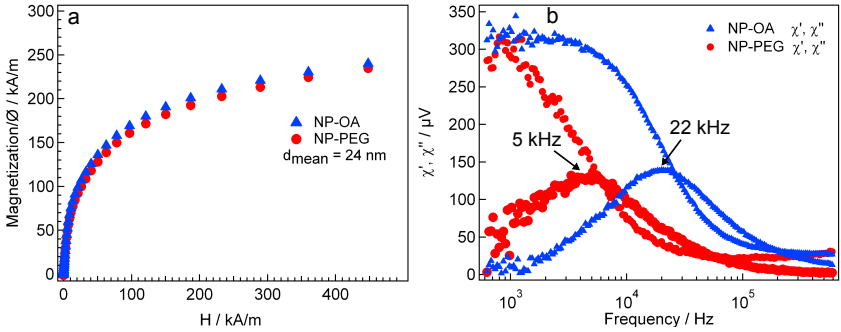

Figure 5.40: (a) $M - H$ magnetization curves and (b) real and imaginary part of the frequency dependent ac susceptibility of NP-OA and NP-PEG particle suspensions taken at RT. The iron concentration of ACS samples was set to 10 mM Fe [137]. Reproduced by permission of The Royal Society of Chemistry.

5.5.4 Cytotoxicity assessment

Macrophages are one of the first cell lines encountering invading microorganisms. They are also important mediators of inflammation. In this study, bone marrow-derived macrophages were treated with the NP-PEG suspensions with three iron doses, 0.3 (labeled by 1:1000 (NP-PEG:DMEM)), 3 and 30 μg_{Fe} mL^{-1} to study their impact on the cytokine release of macrophages. The chemicals and experimental procedures used in the assays are provided in sections 3.6 and 4.8. The levels of IL-6 and IL-10 as inflammatory and anti-inflammatory markers were determined by enzyme-linked immunosorbent assay (ELISA) and the results are plotted in Fig. 5.41(a) and (b). For comparison, the cytokine induced in cells treated with LPS, a strong inflammatory component of Gram-negative bacteria, is plotted too. No release of inflammatory or anti-inflammatory cytokines was observed even at the highest tested particle concentration which exceeds a typical iron concentration used in nanoparticle-based MRI experiments (i.e. 1-20 mg kg^{-1} [71]) [137].

Next, we evaluated the particle cytotoxic effect on *in vitro* cultured bone marrow-derived macrophages. The cultured macrophages were treated with the NP-PEG suspensions with the iron doses mentioned earlier. Generally, the release of the cytoplasmic lactate dehydrogenase (LDH) enzyme into the culture medium is an indication of plasma membrane disruption. Hence the levels of cell cytotoxicity were determined by the release of LDH into the culture supernatants as plotted in Fig. 5.41(c). The particles reveal a moderate cytotoxic effect on macrophages after 24 h of incubation [137].

5.5.5 Particle uptake by macrophages

To examine the particle uptake by macrophages, we have performed a series of TEM experiments on in-situ ultrathin sections of the treated macrophages. The sample preparation and operation conditions are given in section 3.6.3. Fig. 5.42(a) shows a single cell treated with the NP suspensions at an iron

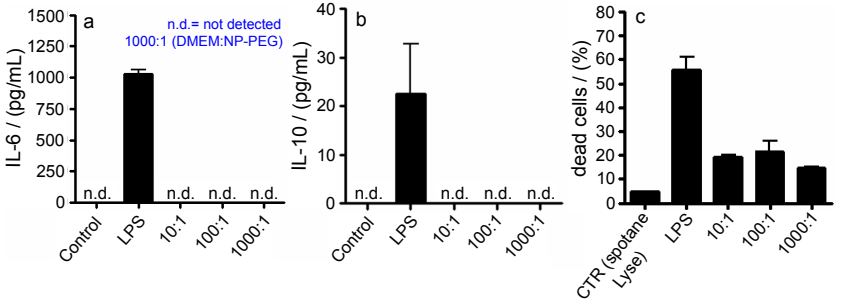

Figure 5.41: Amounts of the IL-6 and IL-10 cytokines released by macrophages after being incubated with NP-PEG suspensions for 24 h determined by ELISA [137]. Reproduced by permission of The Royal Society of Chemistry.

concentration of 30 μg_{Fe} mL^{-1}. The intracellular presence of the NPs taken up by the cell is clearly observed. Apparently, both single particles (indicated by arrows) and micro-sized clusters (captured in circles) were engulfed by the cell via typical phagocytoses and accommodated in primary lysosomes. The area captured in a square is magnified and displayed in Fig. 5.42(b). A survey view of the cell treated with the particles at an iron concentration of 0.3 μg_{Fe} mL^{-1} is depicted in Fig. 5.42(c). It can be seen that the particle uptake reduces considerably as the particle concentration decreases. Interestingly, at this concentration, the engulfed particles are primarily individual NPs (black arrows) as can obviously be seen in Fig. 5.42(d). However, a few nanoscale particle clusters have also been taken up at this dose as can be seen in Fig. 5.42(c). Note that the amount of the particles internalized in the cytoplasm is adjusted to the individual cellular level and differs significantly from cell to cell [137].

To gain a deeper understanding of the dominating endocytosis mechanisms, the particle distribution in a single cell was investigated further. An enlarged image is displayed in Fig. 5.43. Generally speaking, we have found that the particles are endocytosed via both phagocytosis and pinocytosis. The bigger particle aggregates existing outside the cell are phagocytosed through a two step process. Firstly, the aggregates are enclosed by macrophage surface veils outside the cell annotated with "os" in the figure. Secondly, they are internalized into the cell lumen and cellular matrix matter (white arrows). The situation after cytoplasmic uptake (denoted by "is") can also be characterized by the presence of an amorphous medium dense matter. Notably, the cells treat the smaller particles in a different way. Individual to triplex NPs which are in contact with the cell surface are endocytosed by pinocytosis annotated with "pc" in the figure. They can be recognized within the cytoplasm as small envesiculated entities. Interestingly, the amount of single and/or oligomeric NPs taken up by pinocytosis is virtually independent of the particle dose [137].

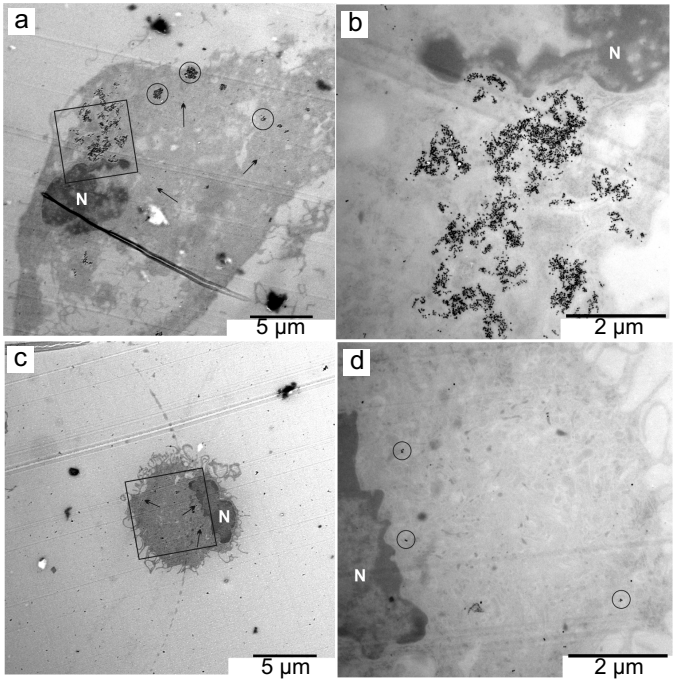

Figure 5.42: TEM micrographs of in-situ ultrathin sections of the macrophages treated with NP-PEG suspensions in DMEM. Typical views of a single treated macrophage at iron concentrations of (a),(b) 30 μg_{Fe} mL^{-1} and (c)(d) 0.3 μg_{Fe} mL^{-1}. N = nucleus and ER = endoplasmic reticulum [137]. Reproduced by permission of The Royal Society of Chemistry.

To confirm that the up taken objects are actually iron oxide NPs, the wide range parallel EELS (WR-PEELS) and ESI Fe-elemental experiments were carried out on the cells. Fig. 5.44(a) shows the recorded Fe-elemental map colored in red. For further investigation, a WR-PEELS spectrum was taken from the selected area (dashed circle) as displayed in Fig. 5.44(b). The presence of O K and Fe $L_{2,3}$ edges suggests that the engulfed objects have iron oxide composition.

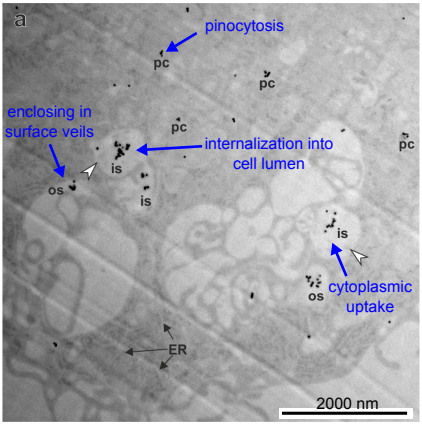

Figure 5.43: Magnified view of a treated macrophage annotated with different endocytosis mechanisms as thoroughly discussed in the text [137]. Reproduced by permission of The Royal Society of Chemistry.

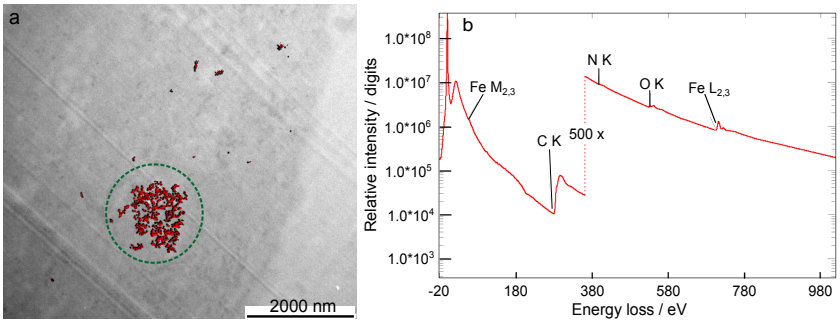

Figure 5.44: (a) ESI Fe-elemental map shown in red, superposed on the ultra-structural grey image of the motif, and (b) WR-PEELS spectrum taken from NP-PEG particles engulfed by macrophages [137]. Reproduced by permission of The Royal Society of Chemistry.

5.6 Homogeneous magnetic bioassays

One of the aims of this thesis is to evaluate the capability of the monodisperse PEGylated iron oxide nanoparticles as biomarkers for homogeneous magnetic bioassays. Having successfully optimized the particle synthesis process and having prepared a highly stable colloidal aqueous suspensions of iron oxide nanoparticles via PEGylation, now we are able to functionalize the particles with proteins or antibodies. For this purpose, we have decided to label the particles with Herceptin antibodies to offer a magnetic marker for detecting tumor specific HER2 biomarkers. In this thesis, the size dependent magnetic response of particles to a rotating magnetic field (RMF) was exploited to assess the binding

of PEG molecules and Herceptin antibodies to particles. The particle response was measured with the fluxgate-based RMF setup (cf. section 3.5.5). The phase lag produced by particles is analyzed to model the change in their hydrodynamic size and eventually approximate the number of bound antibodies. This magnetic detection scheme is simple and quick since no washing steps are needed.

In the next sections, first, we discuss the size dependent particle response to RMF and then the binding mechanisms of the PEGylated NPs to Herceptin will be addressed. Finally, we present and discuss the results of the RMF experiments performed on hydrophobic OA coated (NP-OA), PEGylated (NP-PEG) and ultimately Herceptin functionalized (NP-Herceptin) nanoparticles. The preliminary results of binding Herceptin functionalized nanoparticles to tumor specific HER2 biomarkers will be presented.

5.6.1 Size dependent particle response to RMF

To chose the optimal particles for homogeneous magnetic bioassays in RMF, the particles with different core and hydrodynamic diameters were analyzed with the fluxgate-based RMF setup. Here we discuss the measured phase lag spectra of 13 (i.e. sample R7 discussed in section 5.2) and 24 nm particles as displayed in Fig. 5.45. The 13 nm NPs show a slight increase of the phase lag up to 5 kHz. This behavior indicates that these small particles, with a very small Néel relaxation time constant (i.e. in the order of microsecond), can easily follow the applied rotating magnetic field and thus produce almost no phase lag. Notably, in 24 nm particles, the phase lag increases with frequency. This implies that by increasing the frequency the particle magnetic moment lags behind the magnetic field vector as schematically illustrated in Fig. 5.46. In summary, it can be deduced that the 24 nm NPs, containing a reduced fraction of Néel-relaxation-dominated particles as deduced from ACS results (cf. section 5.5.3), are potent tracers for homogeneous magnetic bioassays in RMF whereas the 13 nm ones, consisting of small particles primarily relaxing via the Néel mechanism, are not.

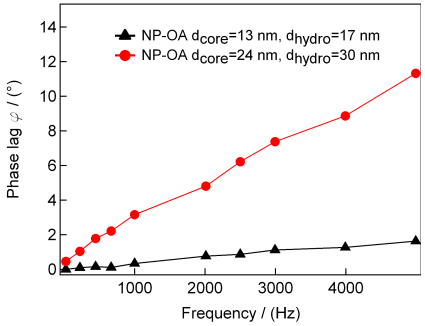

Figure 5.45: Measured phase lag spectra of NP-OA nanoparticles with different core and hydrodynamic sizes versus frequency in 1 mT rotating magnetic field. The solid lines are guides to the eye.

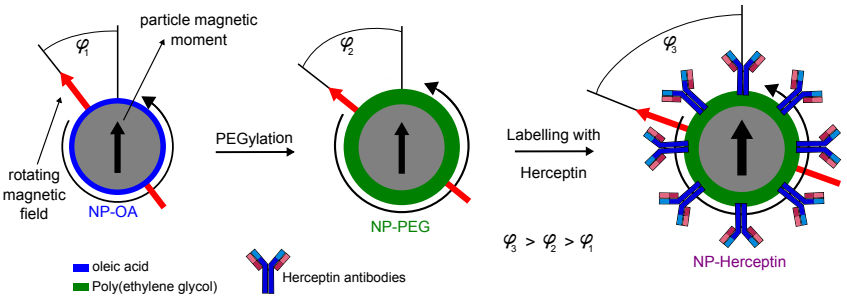

Figure 5.46: Diagrammatic illustration of the increased particle phase lag after transferring into water by PEGylation and eventually by being conjugated to Herceptin antibodies.

5.6.2 Binding Herceptin to nanoparticles

The success and reliability of homogeneous magnetic bioassays depend strongly on the structural and magnetic properties of the used biomarkers. In the last section, we showed that the PEGylated NPs with a magnetic core size of 24 nm have a great potential for magnetic bioassays. To examine their functionality, we have firstly linked Herceptin antibodies to the particles via bio-conjugation chemistry as illustrated in Fig. 5.47. The PEGylated nanoparticles have hydroxyl terminal groups. To make the particles ready for reacting with amine containing Herceptin antibodies, the hydroxyl groups should be activated with amine reactive moieties. N, N'-Disuccinimidyl carbonate, a small homobifunctional NHS ester cross-linking reagent, reacts with the terminal hydroxyl groups of PEG chains in anhydrous solvents and convert them into succinimidyl carbonate groups. In its structure, two NHS ester groups are linked with a carbonyl group as drawn in the figure. This bio-conjugation scheme was adapted for the PEGylated particles from the original recipe proposed by Hermanson [120]. After having the amine activating groups on the particles, the next step is the addition of amine containing antibodies to particle suspensions in Phosphate Buffered Saline (PBS) (coupling buffer, pH=7.4). The particles and antibodies are bound together via amide bonds as can be seen in the chemical structure of NP-Herceptin.

5.6.3 Monitoring of particle surface modification

Fig. 5.48(a) reveals the measured phase lag spectra of NP-OA, NP-PEG and NP-Herceptin nanoparticle suspensions for 1 mT rotating magnetic field versus frequency. It is seen that by further surface modification of the particles and increasing their hydrodynamic size initially via PEGylation and then through labeling with Herceptin, the particle phase lag increases systematically. The stepwise change in the particle phase lag is visualized in Fig. 5.46. This observation corresponds with the rise in the particle hydrodynamic size as monitored by PCCS after functionalization with Herceptin. The results are plotted in Fig. 5.48(b). To simulate the measured phase lag spectra, the empirical

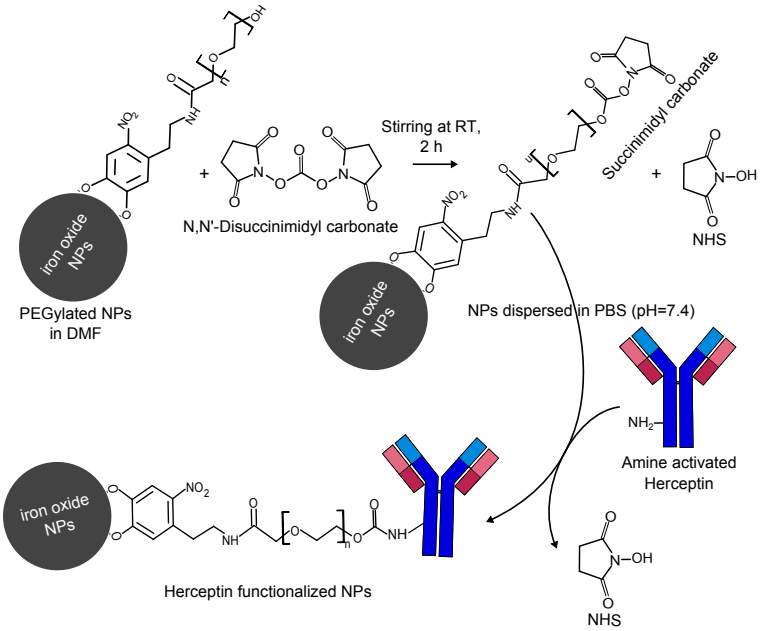

Figure 5.47: Schematic illustration of labeling of PEGylated nanoparticles with Herceptin antibodies using N, N'-Disuccinimidyl carbonate as a homobifunctional NHS ester cross-linker [137]. Reproduced by permission of The Royal Society of Chemistry.

model describing the magnetization dynamics of magnetic nanoparticles in a rotating magnetic field proposed by Yoshida et al. [139] was employed. The particle hydrodynamic diameter d_h and standard deviation can be determined from the fit. The parameters used for the simulations are summarized in Table 5.6.

The fits result in hydrodynamic diameters of 34±4.6 nm, 47.5±12.3 nm and 69±24.5 nm for NP-OA, NP-PEG and NP-Herceptin nanoparticles, respectively. Interestingly, by comparing the hydrodynamic sizes obtained by PCCS and determined from the fit to RMF data, a good agreement can solely be found for NP-OA particles. It seems that by each additional binding step the results tend to diverge more and more. Ultimately, for NP-Herceptin nanoparticles, the results are rather not correlated. In the same way, the measured and simulated phase lag spectra of NP-Herceptin nanoparticles show some deviations. Notably, at the low frequency regime, a noticeable discrepancy between the measured and simulated results is observed. This deviation is presumably due to the presence of a fraction of particles with a hydrodynamic size of 138 nm (clustered particles), measured by PCCS and shown in Fig. 5.48(b), formed during the functionalization process. Since the contribution of clustered particles is not taken into account in the physical model applied for the fit, the

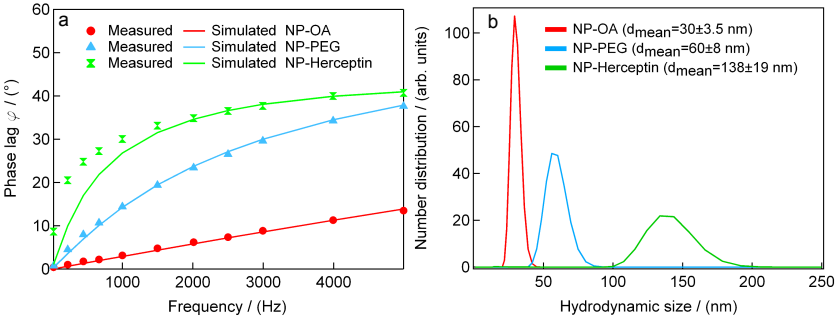

Figure 5.48: (a) Measured (markers) and simulated (solid lines) phase lag spectra of NP-OA, NP-PEG and NP-Herceptin suspensions in 1 mT rotating magnetic field and (b) number weighted particle hydrodynamic size distribution measured by PCCS for all three suspensions. The sample iron concentration was 7, 9.5 and 0.25 mM Fe, respectively [137]. Reproduced by permission of The Royal Society of Chemistry.

Table 5.6: The parameters used for the simulation of the particle phase lag [137]. Reproduced by permission of The Royal Society of Chemistry.

Sample	m (aA m^2)^a	η (mPa s)	Temp. (K)	k^b (×100, %)	d_{hydro}^{RMF}	d_{hydro}^{PCCS}
NP-OA	1.41±0.35	0.56	297	0.067	34±4.6	30±3.5
NP-PEG	1.29±0.31	0.98	294	0.066	47.5±12.3	60±8
NP-Herceptin	1.29±0.31	0.93	296	0.09	69±24.5	138±19

^{a}Estimated from the particle M_s values obtained from Fig. 5.40(a)

^{b}Fraction of Néel relaxation dominated NPs estimated from ACS measurements discussed in section 5.5.3

presence of clusters in the sample can cause the observed deviations. Note that these clusters solely contribute at low frequencies to the signal due to their relatively slow dynamic response. It should be noted that PCCS measurements on suspensions consisting of single and clustered particles are strongly affected by the Rayleigh stray light depending on the sixth power of the hydrodynamic diameter. Accordingly, the existing clusters in NP-Herceptin sample dominate the PCCS measurement. Conversely, in the higher frequency range, since merely the singly isolated NP-Herceptin nanoparticles take part in the measurement, a perfect match between the measured and simulated results is observed [137].

5.6.4 Detection of tumor specific HER2 biomarkers

In the last section of the thesis, we present and discuss the preliminary results of binding Herceptin functionalized nanoparticles to tumor specific HER2 biomarkers. The binding experiments were monitored by the RMF setup via tracing the change in the particle phase lag after adding the HER2 biomarkers to particles (denoted by NP-Herceptin-HER2). Fig. 5.49(a) shows the measured

phase lag spectra of NP-Herceptin and NP-Herceptin-HER2 particles in 1 and 5 mT rotating magnetic fields. By comparing the spectra recorded in 1 mT, it is seen that by further growth of the particle hydrodynamic size after binding to HER2, the phase lag changes drastically. Interestingly, the phase lag rises up to $\approx 20^{\circ}$ and remains unchanged up to 5 kHz being well below the measured phase lag of the NP-Herceptin sample although the hydrodynamic size is expected to be higher. One plausible explanation is that by binding HER2 biomarkers and further growth of hydrodynamic size, the Brownian relaxation time constant (annotated with #4 in Fig. 5.49(b)) becomes higher than the corresponding Néel relaxation time constant (annotated with #1 in Fig. 5.49(b)). As a result, the particles relax via the latter mechanism. To shed a light on this matter, we have measured the sample R4 phase lag (cf. Table 5.1) in mobile (suspended in chloroform) and immobile (solidified with gypsum) states. The measured phase lag spectra are displayed in Fig. 5.50.

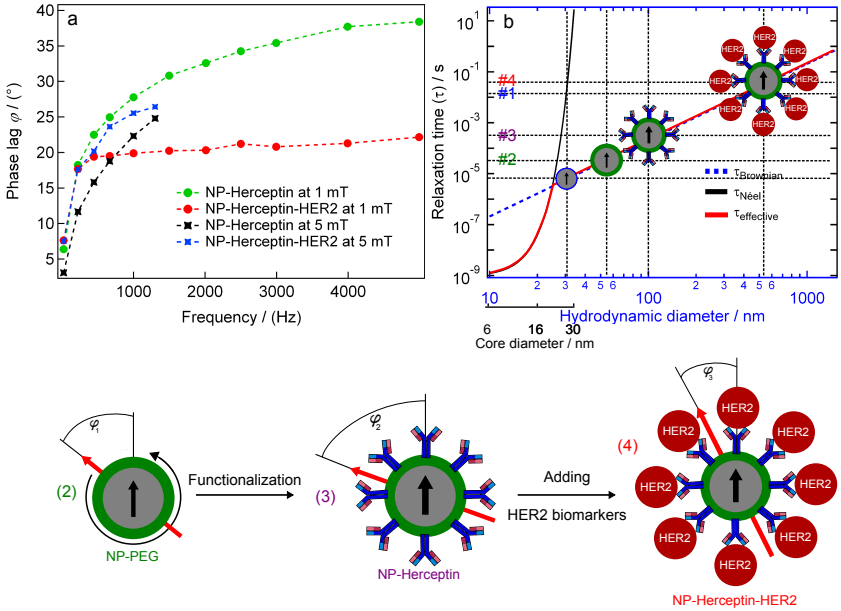

Figure 5.49: (a) Recorded phase lag spectra for NP-Herceptin and NP-Herceptin-HER2 as a function of frequency in 1 and 5 mT and (b) Brownian, Néel and effective relaxation time versus core and hydrodynamic diameters for small field amplitudes. The binding of HER2 biomarkers to NP-Herceptin is schematically depicted in the graph.

By looking at Fig. 5.50, it can be seen that by suppressing the Brownian rotation via immobilizing and activating the Néel mechanism, the increasing trend of the phase lag spectrum changes. Interestingly, the HER2 conjugated particles and the immobile ones reveal a nearly identical RMF response. What

is interesting to note is that by performing the measurements in 5 mT, the particle RMF response changes. Apparently, in 5 mT rotating magnetic field, the particle Brownian relaxation time constant does not overtake the corresponding Néel one and thus the particles yet relax via the Brownian mechanism and show a growing phase lag (blue markers in Fig. 5.49(a)). It has to be mentioned that no adequate physical model for Néel relaxation in large rotating fields exists and thus this topic needs further investigation. The difference observed between the particle relaxational behavior in different field values is an indication of the field dependent particle relaxation time constant.

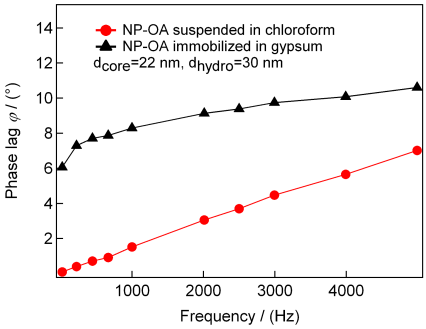

Figure 5.50: Recorded phase lag spectra of NP-OA suspensions in chloroform and immobilized with gypsum in 1 mT rotating magnetic field. The solid lines are guides to the eye.

Conclusion and outlook

In the first part of the thesis, the synthesis of single-core superparamagnetic iron oxide nanoparticles via high temperature decomposition of the self-synthesized iron-oleate was investigated systematically. The influence of iron-oleate concentration, reaction temperature and time and heating rate was optimized with the help of design of experiment methodology. Having analyzed the hydrodynamic diameters obtained from photon cross-correlation spectroscopy, an empirical model showing the dependencies of the hydrodynamic diameter on iron-oleate concentration, reaction temperature and time was found. This systematic approach enabled us to vary the particle core and hydrodynamic sizes from 12 to 24 nm and 17 to 36 nm, respectively, and eventually establish a reproducible protocol for the fabrication of highly monodisperse iron oxide nanoparticles. By combining the magnetorelaxometry, transmission electron microscopy and thermogravimetric analysis results, we concluded that the formation of highly monodisperse nanoparticles with a mean core size of ≈ 13 nm was linked to burst nucleation and quickly terminating growth mechanisms, occurring at the heating rate of 3°C/min. The particle mean core diameter can grow up to 24 nm by retarding the decomposition process with reducing the heating rate to 1°C/min. In this circumstance, gradual and multi-step nucleation and slow growth mechanisms lead to the particle size broadening and modality. To fabricate monodisperse 24 nm nanoparticles, the reaction mixture should be heated up to 357°C at a heating rate of 3°C/min and an iron-oleate concentration of 2 mmol and then age for an hour.

The particle magnetic, structural and compositional properties were correlated to their core size for different sizes varying from 13 to 24 nm by employing high resolution transmission electron microscopy, Mössbauer spectroscopy as well as field and temperature dependent magnetization measurements. We have found that the freshly formed crystallites are primarily made of FeO due to the reductive nature of the decomposition reaction. In the 13 nm nanoparticles, FeO underwent a complete oxidation in the course of aging since the diffusion length is short. Thus, these particles are perfectly ordered single crystals of Fe_3O_4 as deduced from high resolution microscopy and Mössbauer spectroscopy investigations. For these particles, the magnetorelaxometry, transmission electron microscopy and field dependent static magnetization measurements agreed well. As the particle size grows to 18 and 24 nm by increasing the growth time and temperature, the oxidation process becomes retarded and the already formed Fe_3O_4 phase on the outermost layers hampers the further epitaxial growth of Fe_3O_4 towards the center. This situation results in the formation of biphasic FeO/Fe_3O_4 nanoparticles. The oxidation process triggered the formation of disordered and poorly crystalline magnetite domains being oriented in different directions in the shell and also induced lattice defects, atomic displacement and eventually strain in the biphasic particles. The degree of atomic disordering and the amount of lattice defects rose in outer layers

as the particle grew. The FeO/Fe_3O_4 nanoparticles showed a deteriorated magnetization compared to the well ordered 13 nm magnetite particles due to the presence of a large fraction of paramagnetic FeO and the FeO/Fe_3O_4 intermediate phase as well as those disordered poorly crystalline domains, compensating each others magnetizations. A large exchange bias energy was observed in the FeO/Fe_3O_4 particles which increased remarkably as the volume fraction of FeO enlarged. It was found that the relative volume fractions of FeO and the intermediate phase not only determine the exchange and coercive fields, but also the particle blocking temperature.

In the last part of the thesis, we have demonstrated that the exchange of oleic acid capping molecules with nitrodopamine-poly(ethylene glycol) (PEG) compounds is a robust strategy to transfer the hydrophobic particles into water and even biologically relevant medium such as Phosphate Buffered Saline. The particle size monodispersity and magnetic properties remained intact via PEGylation. The PEGylated nanoparticles showed an exceptional water stability over eleven months of being monitored, and also revealed no tendency to aggregate even at 40°C. The PEGylate particles cytotoxic effect was assessed on *in vitro* cultured bone marrow-derived macrophages via 24 h incubation. No release of inflammatory or anti-inflammatory cytokine in the treated macrophages and a moderate cytotoxic effect was observed even at an iron concentration of 30 μg_{Fe} mL^{-1}. The particle cellular uptake by macrophages reduced significantly as the iron concentration decreased. It was found that larger clusters are phagocytosed via a two step process whereas individual to triplex particles are endocytosed by pinocytosis.

The capability of particles with different core sizes for homogeneous magnetic bioassays was evaluated by the fluxgate-based rotating magnetic field measurement system. The particle phase lag was measured magnetically and analyzed to estimate a change in the hydrodynamic properties after surface modification. The results indicated that the particles with a core diameter of 12-14 nm, primarily relaxing via the Néel mechanism, are not suitable for homogeneous magnetic bioassays. The ability to synthesize large mono-modal nanoparticles by using the optimized protocol enabled us to reach a significantly shrunk fraction of the Néel-relaxation-dominated particles in the 24 nm nanoparticles, indicating their potential as a marker for the magnetic detection schemes based on the Brownian relaxation mechanism. These particles were labeled with Herceptin antibodies for the eventual detection of tumor specific HER2 biomarkers. We have observed a systematic increase in the particle phase lag after PEGylation and functionalization with Herceptin. This increasing trend indicates the presence of a PEG layer on the particles and also their successful linkage to Herceptin.

In summary, we have shown that the 24 nm monodisperse PEGylated nanoparticles with a hydrodynamic size of 60 nm are a potent tracer for detecting biomolecules by monitoring their response to RMF. Besides, they are a capable tracer for targeting small biomolecules due to their small size, making them preferable to the commercially available multi-core nanoparticles. The preliminary binding assay between Herceptin labeled nanoparticles and HER2 biomarkers showed the presence of Herceptin antibodies on the particles.

One of the most promising outlooks for this thesis is to find a procedure to improve the magnetic properties of the large particles by shrinking the volume fraction of FeO and increasing the particle crystal ordering. One option is to oxidize the initially formed FeO crystals in-situ with the help of organic oxidizers. Another option would be ex-situ oxidation after having the particles dried. However, since for biomedical applications the particles should be soluble in aqueous fluids, the oxidation of dried particles is a very delicate process and should be done with a great care to avoid particle coalescence and solid fusion. Another interesting topic is to gain a deeper understanding of binding and coordination mechanisms of PEG molecules to particles. Moreover, it is of great importance, particularly for *in vivo* applications, to understand the dissociation kinetics of PEG molecules in biologically relevant media. The functionalization process can further be optimized to improve its yield, avoid particle clustering and eventually establish a more sensitive detection scheme.

Appendix A

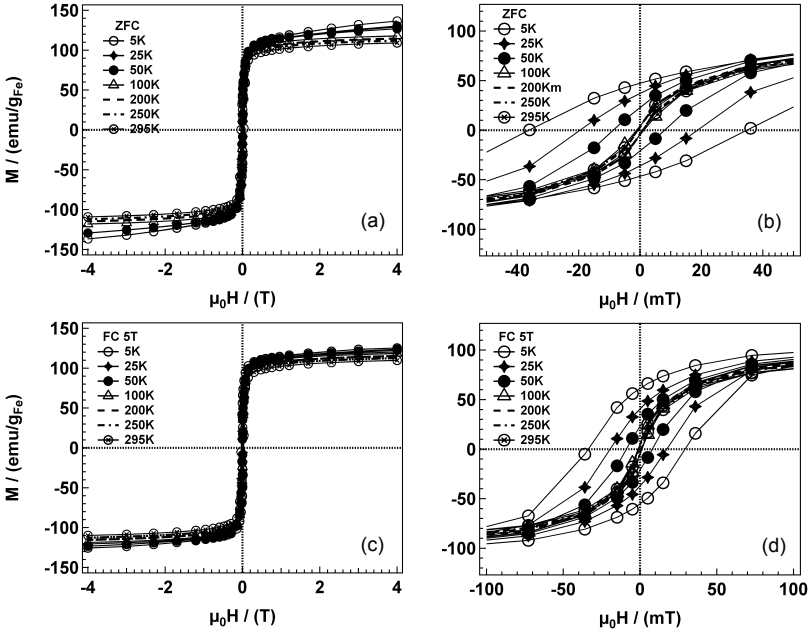

Figure 1: a), (b) ZFC and (c), (d) FC magnetizations of 13 nm Fe_3O_4 NPs versus magnetic field in the cooling field of 5 T taken at different temperatures.

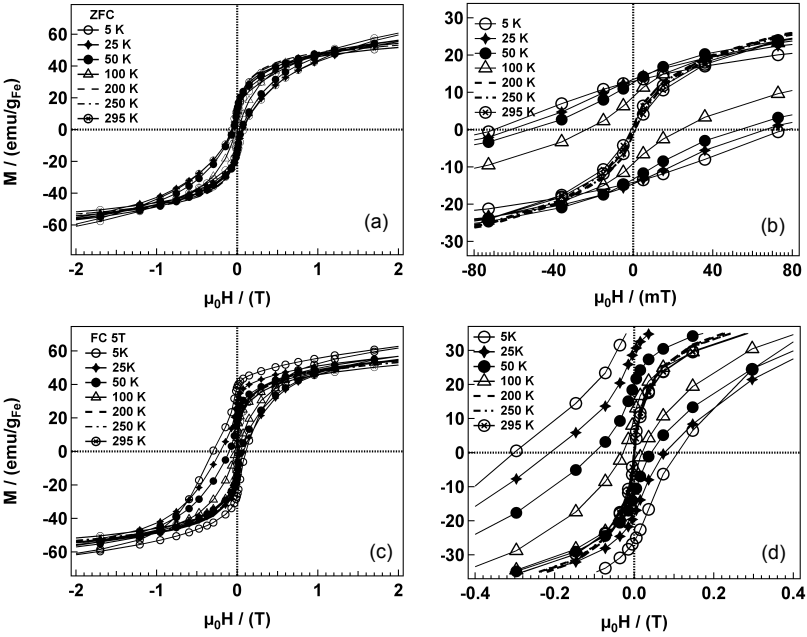

Figure 2: (a), (b) ZFC and (c), (d) FC magnetizations of 18 nm FeO/Fe_3O_4 NPs versus magnetic field in the cooling field of 5 T taken at different temperatures..

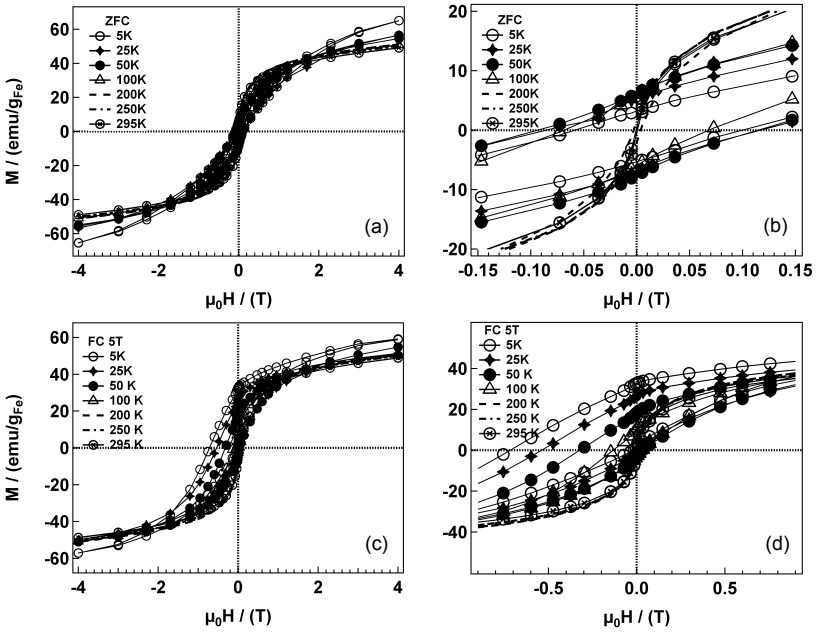

Figure 3: (a), (b) ZFC and (c), (d) FC magnetizations of 24 nm FeO/Fe_3O_4 NPs versus magnetic field in the cooling field of 5 T taken at different temperatures.

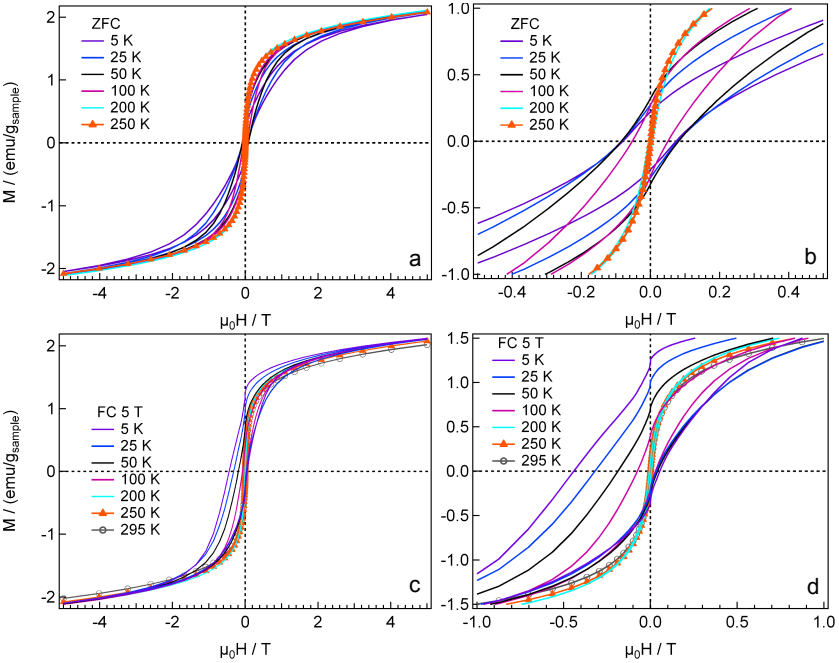

Figure 4: (a), (b) ZFC and (c), (d) FC magnetizations of 24 nm FeO/Fe_3O_4 NPs stored for 120 days at ambient conditions versus magnetic field in the cooling field of 5 T taken at different temperatures.

Publications and presentations

Publications

1. Lak, A., Kraken, M., Ludwig, F., Kornowski, A., Eberbeck, D., Sievers, S., Litterst, F. J., Weller, H., Schilling, M. Size dependent structural and magnetic properties of FeO-Fe_3O_4 nanoparticles. Nanoscale 5: 12286-12295 (2013).
2. Lak, A., Dieckhoff, J., Ludwig, F., Scholtyssek, J. M., Goldmann, O., Lünsdorf, H., Eberbeck, D., Kornowski, A., Kraken, M., Litterst, F. J., Fiege, K., Mischnick, P., Schilling, M. Highly stable monodisperse PEGylated iron oxide nanoparticles aqueous suspensions: a nontoxic tracer for homogeneous magnetic bioassays. Nanoscale 5: 11447-11455 (2013).
3. Lak, A., Ludwig, F., Scholtyssek, J. M., Dieckhoff, J., Fiege, K., Schilling, M. Size distribution and magnetization optimization of single-core iron oxide nanoparticles by exploiting design of experiment methodology. IEEE Transactions on Magnetics 49: 201-209 (2013).
4. Yan, H., Lemmens, P., Wulferding, D., Shi, J., Becker, K. D., Lak, A., Schilling, M. Tailoring defect structure and optical absorption of porous anodic aluminum oxide membranes. Materials Chemistry and Physics 135: 206-211 (2012).
5. Lak, A., Wawrzik, T., Ludwig, F., Schilling, M. Synthesis of single-core iron oxide nanoparticles as a tracer for magnetic particle imaging. Springer Proceedings in Physics, Magnetic Particle Imaging 140: 93-97 (2012).
6. Yoshida, T., Enpuku, Keiji., Ludwig, F., Dieckhoff, J., Wawrzik, T., Lak, A., Schilling, M. Characterization of Resovist® nanoparticles for magnetic particle imaging. Springer Proceedings in Physics, Magnetic Particle Imaging 140: 3-7 (2012).
7. Yan, H.-D., Lemmens, P., Ahrens, J., Bröring, M., Burger, S., Daum, W., Lilienkamp, G., Korte, S., Lak, A., Schilling, M. High-density array of Au nanowires coupled by plasmon modes. Acta Physica Sinica 61: art. no. 237105 (2012).
8. Lak, A., Ludwig, F., Grabs, I.-M., Garnweitner, G., Schilling, M. Influence of synthesis parameters on magnetization and size of iron oxide nanoparticles. American Institute of Physics Conference Proceedings 311: 224-230 (2010).

Presentations

1. Lak, A., Ludwig, F., Scholtyssek, J. M., Wawrzik, T., Schilling, M.: Ultra-stable and high quality PEGylated Fe_3O_4 nanoparticle aqueous

suspensions: tracer for magnetic particle imaging. (Oral) European Materials Research Society, Strasbourg (2013).

2. Lak, A., Ludwig, F., Scholtyssek, J. M., Dieckhoff, J., Schilling, M.: Large single-core iron oxide nanoparticles: a tracer for magnetorelaxometry immunoassays. (Oral) 9$^{\text{th}}$ International Conference on the Scientific and Clinical Applications of Magnetic Carriers, Minneapolis (2012).

3. Lak, A., Ludwig, F., Schilling, M.: Synthesis of single-core iron oxide nanoparticles as a tracer for magnetic particle imaging. (Oral) 2$^{\text{nd}}$ International Workshop on Magnetic Particle Imaging, Lübeck (2012).

4. Lak, A., Ludwig, F., Scholtyssek, J. M., Dieckhoff, J., Schilling, M.: Size distribution and magnetization optimization of single-core iron oxide nanoparticles by design of experiment methodology. (Poster) 12$^{\text{th}}$ German Ferrofluid Workshop, Benediktbeuern (2012).

5. Lak, A., Wawrzik, T., Remmer, H., Ludwig, F., Schilling, M.: In-situ study of iron oxide nanoparticle growth kinetics by means of magnetic particle spectroscopy. (Poster) 11$^{\text{th}}$ German Ferrofluid Workshop, Benediktbeuern (2011).

6. Lak, A., Ludwig, F., Schilling, M.: Ex situ monitoring of superparamagnetic iron oxide nanoparticles growth by fluxgate magnetorelaxometry. (Poster) 10$^{\text{th}}$ German Ferrofluid Workshop, Benediktbeuern (2010).

7. Lak, A., Ludwig, F., Schilling, M.: Influence of synthesis parameters on magnetization and size of iron oxide nanocrystals. (Poster) 8$^{\text{th}}$ International Conference on the Scientific and Clinical Applications of Magnetic Carriers, Rostock (2010).

Bibliography

[1] S. Laurent, D. Forge, M. Port, A. Roch, C. Robic, L. V. Elst, and R. N. Muller. Magnetic iron oxide nanoparticles: synthesis, stabilization, vectorization, physicochemical characterizations, and biological applications. *Chem. Rev.*, **108**: 2064–2110, (2008).

[2] A. H. Lu, E. L. Salabas, and F. Schüth. Magnetic nanoparticles: synthesis, protection, functionalization, and application. *Angew. Chem. Int. Ed.*, **46**: 1222–1244, (2007).

[3] S. Blundell. *Magnetism in condensed matter*. Oxford university press, 2001.

[4] R. E. Rosensweig. *Ferrohydrodynamics*. Dover publications, 1997.

[5] V. K. Varadan, L. Chen, and J. Xie. *Nanomedicine design and applications of magnetic nanomaterials, nanosensors and nanosystems*. Wiley, 2008.

[6] X. Batlle and A. Labarta. Finite-size effects in fine particles: magnetic and transport properties. *J. Phys. D: Appl. Phys.*, **35**: R15–R42, (2002).

[7] D. L. Leslie-Pelecky and R. D. Rieke. Magnetic properties of nanostructured materials. *Chem. Mater.*, **86**: 1770–1783, (1996).

[8] K. M. Krishnan. Biomedical nanomagnetics: A spin through possibilities in imaging, diagnostics, and therapy. *IEEE Trans. Magn.*, **46**: 2523–2558, (2010).

[9] Y. L. Raĭkher and M. I. Shliomis. *The effective field method in the orientational kinetics of magnetic fluids and liquid crystals*. Advances in Chemical Physics Series, Wiley, 1994.

[10] B. A. Larsen, M. A. Haag, N. J. Serkova, K. R. Shroyer, and C. R. Stoldt. Controlled aggregation of superparamagnetic iron oxide nanoparticles for the development of molecular magnetic resonance imaging probes. *Nanotechnology*, **19**: 265102, (2008).

[11] Y-M. Huh, Y-W. Jun, H-T. Song, S. Kim, J-S. Choi, J-H. Lee, S. Yoon, K-S. Kim, J-S. Shin, J-S. Suh, and J. Cheon. In vivo magnetic resonance detection of cancer by using multifunctional magnetic nanocrystals. *J. Am. Chem. Soc.*, **127**: 12387–12391, (2005).

[12] F. Hu, L. Wei, Z. Zhou, Y. Ran, Z. Li, and M. Gao. Preparation of biocompatible magnetite nanocrystals for in vivo magnetic resonance detection of cancer. *Adv. Mater.*, **1819**: 2553–2556, (2006).

[13] Q. A. Pankhurst, J. Connolly, S. K. Jones, and I. Dobson. Applications of magnetic nanoparticles in biomedicine. *J. Phys. D: Appl. Phys.*, **36**: R167–R181, (2003).

[14] E. Heim, F. Ludwig, and M. Schilling. Binding assays with streptavidin-functionalized superparamagnetic nanoparticles and biotinylated analytes using fluxgatemagnetorelaxometry. *J. Magn. Magn. Mater.*, **321**: 1628–1631, (2009).

[15] S. H. Chung, A. Hoffmann, S. D. Bader, C. Liu, B. Kay, L. Makowski, and L. Chen. Biological sensors based on brownian relaxation of magnetic nanoparticles. *Appl. Phys. Lett.*, **85**: 2971, (2004).

[16] A. P. Astalan, F. Ahrentrop, C. Johansson, K. Larsson, and A. Krozer. Biomolecular reactions studied using changes in brownian rotation dynamics of magnetic particles. *Biosens. Bioelectron.*, **19**: 945–951, (2004).

[17] C-Y. Hong, C. C. Wu, Y. C. Chiu, S. Y. Yang, H. E. Horng, and H. C. Yang. Magnetic susceptibility reduction method for magnetically labeled immunoassay. *Appl. Phys. Lett.*, **88**: 212512, (2006).

[18] M. H. F. Meyer, M. Hartmann, H.-J. Krause, G. Blankenstein, B. Mueller-Chorus, J. Oster, P. Miethe, and M. Keusgen. CRP determination based on a novel magnetic biosensor. *Biosens. Bioelectron.*, **22**: 973–979, (2007).

[19] L. Tu, Y. Ling, Y. Li, and J-P. Wang. Real-time measurement of brownian relaxation of magnetic nanoparticles by a mixing-frequency method. *Appl. Phys. Lett.*, **98**: 213702, (2011).

[20] J. Dieckhoff, M. Schilling, and F. Ludwig. Fluxgate based detection of magnetic nanoparticle dynamics in a rotating magnetic field. *Appl. Phys. Lett.*, **99**: 112501, (2011).

[21] B. Gleich and J. Weizenecker. Tomographic imaging using the nonlinear response of magnetic particles. *Nature*, **435**: 1214–1217, (2005).

[22] M. K. Yu, J. Park, and S. Jon. Magnetic nanoparticles and their applications in image-guided drug delivery. *Drug Deliv. and Transl. Res.*, **2**: 3–21, (2012).

[23] C. Xu and S. Sun. New forms of superparamagnetic nanoparticles for biomedical applications. *Adv. Drug Delivery Rev.*, **65**: 732–743, (2013).

[24] M. P. Morales, C. J. Serna, F. Bodker, and S. Morup. Spin canting due to structural disorder in maghemite. *J. Phys.: Condens. Mat.*, **9**: 5461–5467, (1997).

[25] R. Massart. Preparation of aqueous magnetic liquids in alkaline and acidic media. *IEEE Trans. Magn.*, **17**: 1247–1248, (1981).

[26] J. Lee, T. Isobe, and M. Senna. Magnetic properties of ultrafine magnetite particles and their slurries prepared via in-situ precipitation. *Colloids Surf., A*, **109**: 121–127, (1996).

[27] A. K. Guptaa and M. Gupta. Synthesis and surface engineering of iron oxide nanoparticles for biomedical applications. *Biomaterials*, **26**: 3995–4021, (2005).

[28] X. Wang, J. Zhuang, Q. Peng, and Y. Li. A general strategy for nanocrystal synthesis. *Nature Letters*, **437**: 121–124, (2005).

[29] P. Tartaj, M. P. Morales, S. Veintemillas-Verdaguer, T. Gonzalez-Carreno, and C. J. Serna. The preparation of magnetic nanoparticles for applications in biomedicine. *J. Phys. D: Appl. Phys.*, **36**: R182–R197, (2003).

[30] J. Tanori, N. Duxin, C. Petit, I. Lisiecki, I. Lisiecki, and M.P. Pileni. Synthesis of nanosize metallic and alloyed particles in ordered phases. *Colloid Polym. Sci.*, **273**: 886–892, (1995).

[31] N. Feltin and M. P. Pileni. New technique for synthesizing iron ferrite magnetic nanosized particles. *Langmuir*, **13**: 3927–3933, (1997).

[32] E. E. Carpenter. Iron nanoparticles as potential magnetic carriers. *J. Magn. Magn. Mater.*, **225**: 17–20, (2001).

[33] G. Schmidt. *Nanoparticles: From Theory to Application.* Wiley, 2004.

[34] C. B. Murray, D. J. Noms, and M. G. Bawendi. Synthesis and characterization of nearly monodisperse CdE (E = S, Se, Te) semiconductor nanocrystallites. *J. Am. Chem. Soc.*, **115**: 8706–8715, (1993).

[35] J. Park, J. Joo, S. G. Kwon, Y. Jang, and T. Hyeon. Synthesis of monodisperse spherical nanocrystals. *Angew. Chem. Int. Ed.*, **46**: 4630–4660, (2007).

[36] X. Peng, J. Wickham, and A. P. Alivisatos. Kinetics of II – VI and III – V colloidal semiconductor nanocrystal growth: "focusing" of size distribution. *J. Am. Chem. Soc.*, **120**: 5343–5344, (1998).

[37] J. Rockenberger, E. C. Scher, and A. P. Alivisatos. A new nonhydrolytic single-precursor approach to surfactant-capped nanocrystals of transition metal oxides. *J. Am. Chem. Soc.*, **121**: 11595–11596, (1999).

[38] C. B. Murray, C. R. Kagan, and M. G. Bawendi. Synthesis and characterization of monodisperse nanocrystals and closed-packed nanocrystal assemblies. *Annu. Rev. mater. Sci.*, **30**: 545–610, (2000).

[39] X. teng and H. Yang. Effects of surfactants and synthetic conditions on the sizes and self-assembly of monodisperse iron oxide nanoparticles. *J. Mater. Chem.*, **14**: 774–779, (2004).

[40] S. J. Park, S. Kim, S. Lee, Z. G. Khim, K. Char, and T. Hyeon. Synthesis and magnetic studies of uniform iron nanorods and nanospheres. *J. Am. Chem. Soc.*, **122**: 8581–8582, (2000).

[41] T. Hyeon, S. S. Lee, J. park, Y. Chung, and H. B. Na. Synthesis of highly crystalline and monodisperse maghemite nanocrystallites without a size-selection process. *J. Am. Chem. Soc.*, **123**: 12798–12801, (2001).

[42] C. M. Donegá, P. Liljeroth, and D. Vanmaekelbergh. Physicochemical evaluation of the hot-injection method, a synthesis route for monodisperse nanocrystals. *Small*, **1**: 1152–1162, (2005).

[43] S. O'Brien, L. Brus, and C. B. Murray. Synthesis of monodisperse nanoparticles of barium titanate: Toward a generalized strategy of oxide nanoparticle synthesis. *J. Am. Chem. Soc.*, **123**: 12085–12086, (2001).

[44] J. Park, K. An, Y. Hwang, J. G. Park, H. J. Noh, J. Y. Kim, J. H. Park, N. M. Hwang, and T. Hyeon. Ultra-large-scale syntheses of monodisperse nanocrystals. *Nat. Mater.*, **3**: 891–895, (2004).

[45] S. G. Kwon, Y. Piao, J. Park, S. Angappane, Y. Jo, N. M. Hwang, J. G. Park, and T. Hyeon. Kinetics of monodisperse iron oxide nanocrystal formation by heating up process. *J. Am. Chem. Soc.*, **129**: 12571–12584, (2007).

[46] J. Park, E. Lee, N. M. Hwang M. Kang, S. C. Kim, Y. Hwang, J. G. Park, H. J. Noh, J. Y. Kim, J. H. Park, and T. Hyeon. One-nanometer-scale size-controlled synthesis of monodisperse magnetic iron oxide nanoparticles. *Angew. Chem. Int. Ed.*, **44**: 2872–2877, (2005).

[47] W. W. Yu, J. C. Falkner, C. T. Yavuz, and V. L. Colvin. Synthesis of monodisperse iron oxide nanocrystals by thermal decomposition of iron carboxylate salts. *Chem. Commun.*, 2306–2307, (2004).

[48] S. Sun and H. Zeng. Size-controlled synthesis of magnetite nanoparticles. *J. Am. Chem. Soc.*, **124**: 8204–8205, (2002).

[49] V. K. Lamer and R. H. Dinegar. Theory, production and mechanism of formation of monodispersed hydrosols. *J. Am. Chem. Soc.*, **72**: 4847–4854, (1950).

[50] V. Privman, D. V. Goia, J. Park, and E. Matijevic. Mechanism of formation of monodispersed colloids by aggregation of nanosize precursors. *J. Colloid Interface Sci.*, **213**: 36–45, (1999).

[51] V. Gorshkov and V. Privman. Models of synthesis of uniform colloids and nanocrystals. *Physica E*, **43**: 1–12, (2010).

[52] H. Reiss. The growth of uniform colloidal dispersions. *J. Am. Chem. Soc.*, **19**: 482–487, (1951).

[53] T. Sugimoto. *Monodispersed particles*. Elsevier, 2001.

[54] V. F. Puntes, K. M. Krishnan, and A. P. Alivisatos. Colloidal nanocrystal shape and size control: the case of cobalt. *Science*, **291**: 2115–2117, (2001).

[55] S. Sun and C. B. Murray. Synthesis of monodisperse cobalt nanocrystals and their assembly into magnetic superlattices. *J. Appl. Phys.*, **85**: 4325–4330, (1999).

[56] E. V. Shevchenko, D. V. Talapin, A. L. Rogach, A. Kornowski, M. Haase, and H. Weller. Colloidal synthesis and self-assembly of $CoPt_3$ nanocrystals. *J. Am. Chem. Soc.*, **124**: 11480–11485, (2002).

[57] K. Woo, J. Hong, S. Choi, H-W. Lee, J-P. Ahn, C. S. Kim, and S. W. Lee. Easy synthesis and magnetic properties of iron oxide nanoparticles. *Chem. Mater.*, **16**: 2814–2818, (2004).

[58] R. M. Ferguson, K. R. Minard, A. P. Khandhar, and K. M. Krishnan. Optimizing magnetite nanoparticles for mass sensitivity in magnetic particle imaging. *Med. Phys.*, **38**: 1619–1626, (2011).

[59] R. M. Ferguson, A. P. Khandhar, and K. M. Krishnan. Tracer design for magnetic particle imaging. *J. Appl. Phys.*, **111**: 07B318, (2012).

[60] A. Senyei, K. Widder, and G. Czerlinski. Magnetic guidance of drug-carrying microspheres. *J. Appl. Phys.*, **49**: 3578–3583, (1978).

[61] K. J. Widder and A. E. Senyel G. D. Scarpelli. Magnetic microspheres: a model system of site specific drug delivery *in vivo*. *P. Soc. Exp. Biol. Med.*, **158**: 141–146, (1978).

[62] W. Wu, Q. He, and C. Jiang. Magnetic iron oxide nanoparticles: synthesis and surface functionalization strategies. *Nanoscale Res. Lett.*, **3**: 397–415, (2008).

[63] O. Veiseh, J. W. Gunn, and M. Zhang. Design and fabrication of magnetic nanoparticles for targeted drug delivery and imaging. *Adv. Drug Deliver. Rev.*, **62**: 284–304, (2010).

[64] C.-A. J. Lin, R. A. Sperling, J. K. Li, T.-Y. Yang, P.-Y. Li, M. Zanella, W. H. Chang, and W. J. Parak. Design of an amphiphilic polymer for nanoparticle coating and functionalization. *Small*, **4**: 334–341, (2008).

[65] W. W. Yu, E. Chang, C. M. Sayes, R. Drezek, and V. L. Colvin. Aqueous dispersion of monodisperse magnetic iron oxide nanocrystals through phase transfer. *Nanotechnology*, **17**: 4483–4487, (2006).

[66] R. D Corato, A. Quarta, P. Piacenza, A. Ragusa, A. Figuerola, R. Buonsanti, R. Cingolani, L. Manna, and T. Pellegrino. Water solubilization of hydrophobic nanocrystals by means of poly(maleic anhydride-*alt*-1-octadecene). *J. Mater. Chem.*, **18**: 1991–1996, (2008).

[67] E. V. Shtykova, X. Huang, X. Gao, J. C. Dyke, A. L. Schmucker, B. Dragnea, N. Remmes, D. V. Baxter, B. Stein, P. V. Konarev, D. I. Svergun, and L. M. Bronstein. Hydrophilic monodisperse magnetic nanoparticles protected by an amphiphilic alternating copolymer. *J. Phys. Chem. C*, **112**: 16809–16817, (2008).

[68] T. Zhang, J. Ge, Y. Hu, and Y. Yin. A general approach for transferring hydrophobic nanocrystals into water. *Nano Lett.*, **7**: 3203–3207, (2007).

[69] H. Wu, H. Zhu, J. Zhuang, S. Yang, C. Liu, and Y. C. Cao. Water-soluble nanocrystals through dual-interaction ligands. *Angew. Chem. Int. Ed.*, **120**: 3790–3794, (2008).

[70] N. Kohler, G. E. Fryxell, and M. Zhang. A biofunctional poly(ethylene glycol) silane immobilized on metallic oxide-based nanoparticles for conjugation with cell targeting agents. *J. Am. Chem. Soc.*, **126**: 7206–7211, (2004).

[71] H. Lee, E. Lee, D. K. Kim, N. K. Jang, Y. Y. Jeong, and S.angyong Jon. Antibiofouling polymer-coated superparamagnetic iron oxide nanoparticles as potential magnetic resonance contrast agents for in vivo cancer imaging. *J. Am. Chem. Soc.*, **128**: 7383–7389, (2006).

[72] C. Xu, K. Xu, H. Gu, R. Zheng, H. Liu, X. Zhang, Z. Guo, and B. Xu. Dopamine as a robust anchor to immobilize molecules on the iron oxide shell of magnetic nanoparticles. *J. Am. Chem. Soc.*, **126**: 9938–9939, (2004).

[73] U. Tromsdorf, O. T. Bruns, S. C. Salmen, U. Beisiegel, and H. Weller. A highly effective, nontoxic T_1 MR contrast agent based on ultrasmall PEGylated iron oxide nanoparticles. *Nano Lett.*, **9**: 4434–4440, (2009).

[74] E. Amstad, T. Gillich, I. Bilecka, M. Textor, and E. Reimhult. Ultrastable iron oxide nanoparticle colloidal suspensions using dispersants with catechol-derived anchor groups. *Nano Lett.*, **9**: 4042–4048, (2009).

[75] H. B. Na, G. Palui, J. T. Rosenberg, X. Ji, S. C. Grant, and H. Mattoussi. Multidentate catechol-based polyethylene glycol oligomers provide enhanced stability and biocompatibility to iron oxide nanoparticles. *ACS Nano*, **6**: 389–399, (2012).

[76] Y. Zhang, N. Kohler, and M. Q. Zhang. Surface modification of superparamagnetic magnetite nanoparticles and their intracellular uptake. *Biomaterials*, **23**: 1553–1561, (2002).

[77] J. Xie, C. Xu, Z. Xu, Y. Hou, K. L. Young, S. X. Wang, N. Pourmand, and S. Sun. Linking hydrophilic macromolecules to monodisperse magnetite (Fe_3O_4) nanoparticles via trichloro-s-triazine. *Chem. Mater.*, **18**: 5401–5403, (2006).

[78] J. Xie, C. Xu, N. Kohler, Y. Hou, and S. Sun. Controlled PEGylation of monodisperse nanoparticles for reduced non-specific uptake by macrophage cells. *Adv. Mater.*, **19**: 3163–3166, (2007).

[79] D. Liu, W. Wu, J. Ling, S. Wen, N. Gu, and X. Zhang. Effective PEGylation of iron oxide nanoparticles for high performance in vivo cancer imaging. *Adv. Funct. Mater.*, **21**: 1498–1504, (2011).

[80] E. Amstad, S. Zurcher, A. Mashaghi, J. Y. Wong, M. Textor, and E. Reimhult. Surface functionalization of single superparamagnetic iron oxide nanoparticles for targeted magnetic resonance imaging. *Small*, **5**: 1334–1342, (2009).

[81] L. Illum, A. E. Church, M. D. Butterworth, A. Arien, J. Whetstone, and S. S. Davis. Development of systems for targeting the regional lymph nodes for diagnostic imaging: In vivo behaviour of colloidal PEG-coated magnetite nanospheres in the rat following interstitial administration. *Pharm. Res.*, **18**: 640–645, (2001).

[82] C. Barrera, A. P. Herrera, and C. Rinaldi. Colloidal dispersions of monodisperse magnetite nanoparticles modified with poly(ethylene glycol). *J. Colloid Interface Sci.*, **329**: 107–113, (2009).

[83] M. Lattuada and T. A. Hatton. Functionalization of monodisperse magnetic nanoparticles. *Langmuir*, **23**: 2158–2168, (2007).

[84] Y. Xu, Y. Qin, S. Palchoudhury, and Y. Bao. Water-soluble iron oxide nanoparticles with high stability and selective surface functionality. *Langmuir*, **27**: 8990–8997, (2011).

[85] Y. Lu, Y. Yin, B. T. Mayers, and Y. Xia. Modifying the surface properties of superparamagnetic iron oxide nanoparticles through a sol-gel approach. *Nano Lett.*, **2**: 183–186, (2002).

[86] J. Lee, Y. Lee, J. K. Youn, H. B. Na, T. Yu, H. Kim, S.-M. Lee, Y.-M Koo, J. H. Kwak, H. G. Park, H. N. Chang, M. Hwang, J-G. Park, J. Kim, and T. Hyeon. Simple synthesis of functionalized superparamagnetic magnetite/silica core/shell nanoparticles and their application as magnetically separable high-performance biocatalysts. *Small*, **4**: 143–152, (2008).

[87] M. Zhang, B. L Cushing, and C. J O'connor. Synthesis and characterization of monodisperse ultra-thin silica-coated magnetic nanoparticles. *Nanotechnology*, **19**: 085601, (2008).

[88] D. Niu, Y. Li, Z. Ma, H. Diao, J. Gu, H. Chen, W. Zhao, M. Ruan, Y. Zhang, and J. Shi. Preparation of uniform, water-soluble, and multifunctional nanocomposites with tunable sizes. *Adv. Funct. Mater.*, **20**: 773–780, (2010).

[89] D. Shao, K. Xu, X. Song, J. Hu, W. Yang, and C. Wang. Effective adsorption and separation of lysozyme with PAA-modified Fe_3O_4@silica core/shell microspheres. *J. Colloid Interface Sci.*, **336**: 526–532, (2009).

[90] W. Stöber, A. Fink, and E. Bohn. Controlled growth of monodisperse silica spheres in the micron size range. *J. Colloid Interface Sci.*, **26**: 62–69, (1968).

[91] D. Ma, J. Guan, F. Normandin, S. Dénommée, G. Enright, T. Veres, and B. Simard. Multifunctional nano-architecture for biomedical applications. *Chem. Mater.*, **18**: 1920–1927, (2006).

[92] Y.-H Deng, C.-C Wang, J.-H Hu, W.-L Yang, and S.-K Fu. Investigation of formation of silica-coated magnetite nanoparticles via sol-gel approach. *Colloids Surf., A*, **262**: 87–93, (2005).

[93] Kazuo Nakamoto. *Infrared and Raman spectra of inorganic and coordination compounds.* Wiley, 1986.

[94] R. F. Egerton. *Physical principles of electron microscopy: An introdcution to TEM, SEM and AEM.* Springer, 2005.

[95] R. Kötitz, L. Trahms, H. Koch, and W. Weitschies. Ferrofluid relaxation for biomagnetic imaging. In: C. Baumgartner, L. Deecke, and S. J. Williamson. *Biomagnetism: Fundamental research and clinical applications.* Elsevier Science, 1995.

[96] H. L. Grossman, W. R. Myers, V. L. Vreeland, R. Bruehl, M. D. Alper, C. B. Bertozzi, and J. Clarke. Detection of bacteria in suspension by using a superconducting quantum interference device. *Proc. Natl. Acad. Sci. USA*, **101**: 129–134, (2004).

[97] I. A. Volkov, M. L. Chkharkin, O. V. Snigirev, A. V. Volkov, M. A. Moskvina, S. A. Gudoshnikov, and A. K. Kerimov. HTS SQUID microscopy for measuing the magnetization relaxation of magnetic nanoparticles. *IEEE Trans. Appl. Supercond.*, **15**: 3874–3878, (2005).

[98] F. Ludwig, S. Mäuselein, E. Heim, and M. Schilling. Magnetorelaxometry of magnetic nanoparticles in magnetically unschielded environment utilizing a differential fluxgate arrangement. *Rev. Sci. Instrum.*, **76**: 106102, (2005).

[99] E. A. Heim. *Fluxgate-Magnetrelaxometrie magnetischer Nanopartikel in der Bioanalytik.* PhD thesis, Technische Universität Braunschweig, 2009.

[100] F. Ludwig, E. Heim, S. Mäuselein, D. Eberbeck, and M. Schilling. Magnetorelaxometry of magnetic nanoparticles with fluxgate magnetometers for the analysis of biological targets. *J. Magn. Magn. Mater.*, **293**: 690–695, (2005).

[101] R. W. Chantrell, S. R. Hoon, and B. K. Tanner. Time-dependent magnetization in fine-particle ferromagnetic systems. *J. Magn. Magn. Mater.*, **38**: 133–141, (1983).

[102] F. Ludwig, E. Heim, D. Menzel, and M. Schilling. Investigation of superparamagnetic Fe_3O_4 nanoparticles by fluxgate magnetorelaxometry for use in magnetic relaxation immunoassays. *J. Appl. Phys.*, **99**: 08P106, (2006).

[103] S. Amelinckx, D. van Dyck, J. van Landuyt, and G. van Tendeloo. *Electron microscopy: Principles and fundamentals.* Wiley, 1997.

[104] R. J. D. Tilley. *Crystals and crystal structures.* Wiley, 2006.

[105] R. F. Egerton. Electron energy-loss spectroscopy in the TEM. *Rep. Prog. Phys.*, **72**: 016502, (2009).

[106] Z. L. Wang. *Characterization of Nanophase Materials.* Wiley, 2000.

[107] R. F. Egerton. *Electron energy loss spectroscopy in the electron microscope.* Springer, 2011.

[108] R. Finsy. Particle sizing by quasi-elastic light scattering. *Adv. Colloid Interface Sci.*, **52**: 79–143, (1994).

[109] R. L. Mössbauer. *Les Prix Noble en 1961.* Noble Foundation, 1962.

[110] F. Walz. The verwey transition a topical review. *J. Phys.: Condens. Mat.*, **14**: R285–R340, (2002).

[111] D. W. Kavich, J. H. Dickerson, S. V. Mahajan, S. S. Hasan, and J. H. Park. Exchange bias of singly inverted FeO/Fe_3O_4 core-shell nanocrystals. *Phys. Rev. B*, **78**: 174414, (2008).

[112] J. Connolly and T. G. St Pierre. Proposed biosensors based on time-dependent properties of magnetic fluids. *J. Magn. Magn. Mater.*, **225**: 156–160, (2001).

[113] F. Ludwig, A. Guillaume, M. Schilling, N. Frickel, and A. M. Schmidt. Determination of core and hydrodynamic size distibutions of $CoFe_2O_4$ nanoparticle suspensions using ac susceptibility measurements. *J. Appl. Phys.*, **108**: 033918, (2010).

[114] S. H. Chung, A. Hoffmann, K. Guslienko, S. D. Bader, C. Liu, B. Kay, L. Makowski, and L. Chen. Biological sensing with magnetic nanoparticles using brownian relaxation. *J. Appl. Phys.*, **97**: 10R101, (2005).

[115] H. Friebolin. *Basic one- and two-dimensional NMR spectroscopy.* Wiley, 2005.

[116] M. Roming, H. Lünsdorf, K. E. J. Dittmar, and C. Feldmann. $ZrO(HPO_4)_{1-x}(FMN)_x$: Quick and easy synthesis of a nanoscale luminescent biomarker. *Angew. Chem. Int. Ed.*, **48**: 1–7, (2009).

[117] T. T. Tidwell. Wilhelm schlenk: The man behind the flask. *Angew. Chem. Int. Ed.*, **40**: 331–337, (2001).

[118] A. Lak, F. Ludwig, J. M. Scholtyssek, J. Dieckhoff, K. Fiege, and M. Schilling. Size distribution and magnetization optimization of single-core iron oxide nanoparticles by exploiting design of experiment methodology. *IEEE Trans. Magn.*, **49**: 201–209, (2013).

[119] B. Malisova, S. Tosatti, M. Textor, K. Gademann, and S. Zurcher. Poly(ethylene glycol) adlayers immobilized to metal oxide substrates through catechol derivatives: Influence of assembly conditions on formation and stability. *Langmuir*, **26**: 4018–4026, (2010).

[120] G. T. Hermanson. *Bioconjugate techniques.* Academic press, 2008.

[121] F. Ludwig. Characterization of magnetic core-shell nanoparticles suspensions using ac susceptibility for frequencies up to 1 MHz. *AIP Conf. Proc.*, **1311**: 249–254, (2010).

[122] S. Palchoudhury, W. An, Y. Xu, Y. Qin, Z. Zhang, N. Chopra, R. A. Holler, C. H. Truner, and Y. Bao. Synthesis and growth mechanism of iron oxide nanowhiskers. *Nano Lett.*, **11**: 1141–1146, (2011).

[123] J. Xie, C. Xu, Z. Xu, Y. Hou, K. L. Young, S. X. Wang, N. Pourmand, and S. Sun. The concept of delayed nucleation in nanocrystal growth demonstrated for the case of iron oxide nanodisks. *J. Am. Chem. Soc.*, **128**: 1675–1682, (2006).

[124] A. Lak, M. Kraken, F. Ludwig, A. Kornowski, D. Eberbeck, S. Sievers, F. J. Litterst, H. Weller, and M. Schilling. Size dependent structural and magnetic properties of FeO/Fe_3O_4 nanoparticles. *Nanoscale*, **5**: 12286–12295, (2013).

[125] M. Levy, A. Quarta, A. Espinosa, A. Figuerola, C. Wilhelm, M. Garíca-Hernández, A. Genovese, A. Falqui, D. Alloyeau, R. Buonsanti, P. D. Cozzoli, M. A. García, F. Gazeau, and T. Pellegrino. Correlating magneto-structural properties to hyperthermia performance of highly monodisperse iron oxide nanoparticles prepared by a seeded-growth route. *Chem. Mater.*, **23**: 4170–4180, (2011).

[126] J. Rodriguez-Carvajal. *FullProf Suite*. LLB Saclay & LCSIM, Rennes, France, 2003.

[127] B. Luigjes, S. M. C. Woudenberg, R. de Groot, J. D. Meeldijk, H. M. Torres Galvis, K. P. de Jong, A. P. Philipse, and B. H. Erné. Diverging geometric and magnetic size distributions of iron oxide nanocrystals. *J. Phys. Chem. C*, **115**: 14598–14605, (2011).

[128] C. Colliex, T. Manoubi, and C. Ortiz. Electron-energy-loss-spectroscopy near-edge fine structures in the iron-oxygen system. *Phys. Rev. B*, **44**: 11402–11411, (1991).

[129] D. H. Pearson, B. Fultz, and C. C. Ahn. Measurements of 3d state occupancy in transition metals using electron energy loss spectrometry. *Appl. Phys. Lett.*, **53**: 1405–1407, (1988).

[130] J. Jasinski, K. E. Pinkerton, I.M. Kennedy, and V. J. Leppert. Spatially resolved energy electron loss spectroscopy studies of iron oxide nanoparticles. *Microsc. Microanal.*, **12**: 424–431, (2006).

[131] C. A. McCammon and D. C. Price. Mössbauer spectra of Fe_xO (x>0.95). *Phys. Chem. Miner.*, **11**: 250–254, (1985).

[132] I. Dézsi, Cs. Fetzer, Á. Gombkötő, I. Szűcs, J. Gubicza, and T. Ungár. Phase transition in nanomagnetite. *J. Appl. Phys.*, **103**: 104312–2, (2008).

[133] X. Sun, N. F. Huls, A. Sigdel, and S. Sun. Tuning exchange bias in core/shell FeO/Fe_3O_4 nanoparticles. *Nano Lett.*, **12**: 246–251, (2012).

[134] D. V. Berkov, P. Görnert, N. Buske, C. Gansau, J. Mueller, M. Giersig, W. Neumann, and D. Su. New method for the determination of the particle magnetic moment distribution in a ferrofluid. *J. Phys. D: Appl. Phys.*, **33**: 331–337, (2000).

[135] T. Yoshida, K. Enpuku, F. Ludwig, J. Dieckhoff, T. Wawrzik, A. Lak, and M. Schilling. Characterization of resovist nanoparticles for magnetic particle imaging. In: T. M. Buzug and J. Borgert. *Magnetic particle imaging: A novel SPIO nanoparticle imaging technique*. Springer, 2012.

[136] M. R. Fitzsimmons, P. Yashar, C. Leighton, I. K. Schuller, J. Nogués, C. F. Majkrzak, and J. A. Dura. Asymmetric magnetization reversal in exchange-biased hysteresis loops. *Phys. Rev. Lett.*, **84**: 3986–3989, (2000).

[137] A. Lak, J. Dieckhoff, F. Ludwig, J. M. Scholtyssek, O. Goldmann, H. Lünsdorf, D. Eberbeck, A. Kornowski, M. Kraken, F. J. Litterst, K. Fiege, P. Mischnick, and M. Schilling. Highly stable monodisperse PEGylated iron oxide nanoparticle aqueous suspensions: a nontoxic tracer for homogeneous magnetic bioassays. *Nanoscale*, **5**: 11447–11455, (2013).

[138] S. M. Kang, I. S. Choi, K.-B. Lee, and Y. Kim. Bioconjugation of poly(poly(ethylene glycol) methacrylate)-coated iron oxide magnetic nanoparticles for magnetic capture of target proteins. *Macromol. Res.*, **17**: 259–264, (2009).

[139] T. Yoshida, K. Enpuku, J. Dieckhoff, M. Schilling, and F. Ludwig. Magnetic fluid dynamics in a rotating magnetic field. *J. Appl. Phys.*, **111**: 053901, (2012).

List of Figures

List of Tables

Acknowledgements

I would like to thank all the people who contributed to this work and supported me during the last few years.

First, many thanks to Prof. Dr. Meinhard Schilling for giving me the opportunity of working in his group, Braunschweig International Graduate School of Metrology PhD scholarship grant and supervising my PhD thesis work. I would like to thank him for his kind support, helpful advice and scientific input.

I would like to thank Dr. Frank Ludwig for introducing me to different magnetic measurements and his valuable scientific discussions regarding nanomagnetism. I also would like to thank him for proofreading of my manuscript.

I would like to thank Prof. Dr. Horst Weller, Dr. Andreas Kornowski and Ms. Almut Barck from Hamburg University for HRTEM, EELS and XRD measurements.

I would like to thank Prof. Dr. Fred Jochen Litterst and Mathias Kraken for Mössbauer measurement, analysis and for always being keen for discussions. Another thank you goes to Prof. Dr. Fred Jochen Litterst who accepted being examiner of my PhD thesis work.

I would like to thank Prof. Dr. Petra Mischnick and Dr. Kathrin Fiege for NMR measurement and analysis and also for letting me to use the facilities at the Institute of Food Chemistry.

I would like to thank Dr. Oliver Goldmann and Dr. Heinrich Lünsdorf from Helmholtz Center for Infection Research, Braunschweig, for cytotoxicity assessment and TEM ultrastructural analysis.

I would like to thank Dr. Dietmar Eberbeck and Dr. Sibylle Sievers from Physikalisch-Technische Bundesanstalt, Berlin and Braunschweig, for SQUID magnetization measurements.

I would like to thank Prof. Dr. Peter Lemmens for being co-examiner of my PhD thesis work.

A big thank you goes to Dr. Jan. M. Scholtyssek for performing many TEM measurements.

A thank you goes to Dr. Dezhen Li and Sandra Engelhardt for helping me to start my PhD scholarship.

I would like to thank Gabriele Weise for taking care of all the administrative affairs and Kerstin Franke, Bjorn Kühn and Ralf Behme for technical support. A thank you goes to Georg Dornig and Tanja Coenen for graphic design. I would like to thank Mr. Schmidt, Mr. Müller and Mr. Pförtner from the workshop.

A special thank you goes to Thilo Wawrzik and Jan Dieckhoff for being such great colleagues and friends: Thilo and Jan, always open to scientific discussions and happy to help me with work unrelated issues. Jan, I very much enjoyed working with you, our philosophical discussions and also spending time "out of the lab" with you. I thank Thilo and Jan for MPS and RMF measurements and analyses.

A thank you goes to all former and current colleagues in EMG for their support and the very friendly atmosphere.

A warm thank you goes to my parents for their continuous support.

Finally, my biggest thanks go to my wonderful wife Matin for her great love, unconditional support and patience.